

CLUSTER SUPERLATTICE MEMBRANES

INAUGURAL DISSERTATION

zur

Erlangung des Doktorgrades
der Mathematisch-Naturwissenschaftlichen Fakultät
der Universität zu Köln

vorgelegt von

M. Sc. Tobias Hartl

aus

Frechen

Köln Juni 2023

Erster Gutachter: Prof. Dr. Thomas Michely

Zweiter Gutachter: Prof. Dr. Ruslan Temirov

Tag der mündlichen Prüfung: 05.09.2023

Abstract

The rapid development of two-dimensional (2D) materials has revolutionized various fields of science and technology, offering immense potential for diverse applications. Novel techniques have emerged which bestow scientists with the capability to tailor the properties of 2D materials specifically for their intended applications. One of the many fields in which 2D materials are employed is catalysis. Requirements for modern catalysts are a high efficiency and stability. Both are governed by their atomic make up, structure and support, all of which can be rationally designed to optimize their performance. One incredibly promising system capable of supporting nano catalysts are so called cluster superlattices. These structures, made up of a templating support and long range ordered nano clusters, are self organizing and highly versatile, allowing a near endless combination of metals and supports. Their application so far has been hampered by their instability, as the long range order of the cluster degrades at temperatures of a few hundred centigrade or atmospheric pressures.

In this work, a newly synthesized 2D material - the so called cluster superlattice membrane (CSLM) - which aims to solve these instability problems is presented. The remarkable properties and versatility in possible application is not limited to catalysis but encompasses the fields of optoelectronics, and magnetism as well. The material is synthesized through a bottom-up approach, combining precise control over atomic arrangements and advanced transfer techniques.

In the first manuscript the general idea and fabrication method of the CSLM is introduced. Scanning tunneling microscopy (STM), low energy electron diffraction (LEED) and X-ray photoelectron spectroscopy (XPS) are employed to study the carbon embedding process. Restructuring in the a-C layer at elevated temperatures is observed, which in turn lowers the binding of the Gr to the substrate, which is revealed to be a requirement for the successful delamination from the Ir(111) substrate. A conventional hydrogen bubbling transfer method is then used to remove the CSLM from the substrate and form the final free standing 2D material. Transmission electron microscopy (TEM) reveals the presence of a perfectly ordered cluster superlattice inside the a-C matrix while TEM diffraction measurements and Raman spectroscopy provide evidence for the graphene layer still being present.

The second manuscript extends the idea of the CSLM from the graphene templating layer to hexagonal Boron Nitride (h-BN). The embedding process with carbon on this structurally similar but atomically different compound is studied via STM and XPS. The combination of h-BN template and Pt clusters not only shows the versatility of the system, but allows to disentangle effects of the carbon deposition onto the clusters from the interactions of the clusters with the templating layer and the Ir substrate in the XP spectra. The C attaches to the clusters first, and only after fully covering them forms the stabilizing network, while rehybridizing the h-BN layer. High temperature annealing shows the C domes to be stable, but analysis of the Pt signal shows intercalation of the cluster material below the h-BN layer.

In the third manuscript the moiré of h-BN on Ir(111) is used to grow a Si cluster superlattice, extending group of templatable elements even further. The calibration of deposited Si on Ir(111) is done via a $(\sqrt{19} \times \sqrt{19})$ Si/Ir(111) superstructure. h-BN is a large band gap insulator and as such the perfect substrate to study the size dependent electronic structure of the Si clusters via scanning tunneling spectroscopy (STS). Experiments show that with decreasing cluster size the band gap of the Si is increased. Finally the thermal stability of the Si CSL is investigated.

Chapter 6 details the development of a transfer strategy which is required to handle the CSLMs, as they are asymmetrical and top and bottom of the membrane differ strongly. The requirements for large scale delamination of the membranes are discussed and influences of size and thickness on the process are tested via optical microscopy. Finally a working transfer method is given which enables side sensitive transfers of large scale CSLMs.

Building on the work of all prior chapters, Chapter 7 a CSLM based on FePt clusters is transferred graphene side up to a new Ir(111) substrate and the protective properties of the graphene are tested via exposure to oxygen radicals. X-ray adsorption near edge spectroscopy (XANES) shows that the clusters don't oxidise as long as Gr is present. The ability of O to adsorb on Gr is then used to etch away the Gr in a controlled fashion, to expose the clusters to the atmosphere again, at which point the CSLM is ready to be used in experiments in nano catalysis.

The scientific appendix provides additional information on h-BN based cluster superlattice membranes. TEM has been used to confirm the clusters to be protected in the a-C layer after the removal from the substrate. Diffraction shows the presence of h-BN. An annealing series determines the stability and sintering mechanism of the CSL in the membranes up to 1050 K. High temperature imaging at 1350 K provides direct evidence of particle migration and coalescence happening inside the membranes.

German Abstract

(Deutsche Kurzzusammenfassung)

Die rasante Entwicklung zweidimensionaler (2D) Materialien hat verschiedene Bereiche der Wissenschaft und Technologie revolutioniert und ein enormes Potenzial für vielfältige Anwendungen eröffnet. Neue Techniken sind entstanden, die Wissenschaftlern die Fähigkeit verleihen, die Eigenschaften von 2D-Materialien gezielt auf ihre beabsichtigten Anwendungen zuzuschneiden. Einer der vielen Bereiche, in denen 2D-Materialien eingesetzt werden, ist die Katalyse. Die Anforderungen an moderne Katalysatoren sind hohe Effizienz und Stabilität. Beide Eigenschaften werden durch ihre atomare Zusammensetzung, geometrische Struktur und Trägermaterialien bestimmt, die alle gezielt gestaltet werden können, um ihre Leistung zu optimieren. Ein äußerst vielversprechendes System für Nano-Katalysatoren sind sogenannte Cluster-Übergitter. Diese Strukturen bestehen aus einem strukturgebenden Templat und Nano-Clustern mit einer langreichweitigen Ordnung und sind selbst organisierend und äußerst vielseitig. Sie ermöglichen eine nahezu endlose Kombination von Metallen und Templatmaterialien. Ihre Anwendung wurde bisher jedoch durch ihre Instabilität behindert, da die langreichweitige Ordnung der Cluster bei Temperaturen von einigen hundert Grad Celsius oder hohem Druck zerstört wird.

In dieser Arbeit wird ein neu synthetisiertes 2D-Material vorgestellt - die sogenannte Cluster-Übergitter-Membran (**Cluster SuperLattice Membrane** - CSLM), die darauf abzielt, diese Instabilitätsprobleme zu lösen. Die bemerkenswerten Eigenschaften und die Vielseitigkeit der möglichen Anwendungen beschränken sich nicht nur auf die Katalyse, sondern umfassen auch die Bereiche Optoelektronik und Magnetismus. Das Material wird durch einen Bottom-up-Ansatz synthetisiert, der präzise Kontrolle über atomare Anordnungen und fortschrittliche Transferverfahren kombiniert.

Im ersten Manuskript wird die allgemeine Idee und Herstellungsmethode der CSLM vorgestellt. Raster-Tunnelmikroskopie (STM), Niederenergie-Elektronenbeugung (LEED) und Röntgenphotoelektronenspektroskopie (XPS) werden eingesetzt, um den Prozess der Kohlenstoffeinbettung zu untersuchen. Eine Umstrukturierung in der amorphen Kohlenstoff (a-C) Schicht bei erhöhten Temperaturen wird beobachtet, was wiederum die Bindung von Graphen (Gr) an das Substrat

verringert. Dies ist eine Voraussetzung für eine erfolgreiche Ablösung von dem Ir(111)-Substrat. Anschließend wird eine konventionelle Wasserstoffblasen-Transfermethode verwendet, um die Membran vom Substrat zu entfernen und das endgültige freistehende 2D-Material zu bilden. Die Transmissionselektronenmikroskopie (TEM) zeigt das Vorhandensein eines perfekt geordneten Cluster-Übergitters innerhalb der a-C-Matrix, während TEM-Beugungsmessungen und Raman-Spektroskopie Hinweise darauf liefern, dass die Graphenschicht weiterhin vorhanden ist. Das zweite Manuskript erweitert die Idee der CSLM von der Graphen-Templatschicht auf hexagonales Bornitrid (h-BN). Der Einbettungsprozess mit Kohlenstoff auf dieser strukturell ähnlichen, aber atomar unterschiedlichen Verbindung wird mittels STM und XPS untersucht. Die Kombination aus h-BN-Templat und Pt-Clustern zeigt nicht nur die Vielseitigkeit des Systems, sondern ermöglicht es auch, die Effekte der Kohlenstoffeinbettung auf die Cluster von den Wechselwirkungen der Cluster mit der Templatschicht und dem Ir-Substrat in den XP-Spektren zu entflechten. Das Kohlenstoff heftet sich zuerst an die Cluster und bildet erst nach vollständiger Bedeckung ein stabilisierendes Netzwerk, wobei die h-BN-Schicht um hybridisiert wird. Ein Hochtemperatur Ausheilen zeigt, dass die Kohlenstoffkuppeln stabil sind, aber die Analyse des Pt-Signals zeigt, dass eine Interkalation des Cluster-Materials durch die h-BN-Schicht erfolgt. Im dritten Manuskript wird das Moiré-Muster von h-BN auf Ir(111) genutzt, um ein Si-Cluster-Übergitter zu erzeugen und die Gruppe der Übergitter formenden Elemente zu erweitern. Die Kalibrierung des auf Ir(111) abgeschiedenen Si erfolgt über eine ($\sqrt{19} \times \sqrt{19}$) Si/Ir(111)-Überstruktur. H-BN ist ein Isolator mit großer Bandlücke und somit das perfekte Substrat, um die größenabhängige elektronische Struktur der Si-Cluster mittels Raster-Tunnel-Spektroskopie (STS) zu untersuchen. Experimente zeigen, dass mit abnehmender Clustergröße die Bandlücke des Si wächst. Schließlich wird die thermische Stabilität der Si-Cluster-Übergitter untersucht. Kapitel 6 erläutert die Entwicklung einer Transferstrategie, die für die CSLMs erforderlich ist, da sich im Gegensatz zu herkömmlichen 2D Materialien die Ober- und Unterseite der Membran stark unterscheiden. Die Anforderungen an die großflächige Ablösung der Membranen werden diskutiert und der Einfluss von Größe und Dicke auf den Prozess wird mittels optischer Mikroskopie getestet. Schließlich wird eine funktionierende Transfermethode vorgestellt, die eine großflächige, seitensensitive Übertragung von Cluster-Übergittermembranen ermöglicht. Aufbauend auf den Arbeiten aller vorherigen Kapitel wird in Kapitel 7 eine CSLM auf der Basis von FePt-Clustern mit der exponierten Graphenseite auf ein neues Ir(111)-Substrat übertragen. Die schützenden Eigenschaften des Graphens werden durch die Exposition der FePt Cluster gegenüber Sauerstoffradikalen getestet. Röntgen-Absorptionskanten-Spektroskopie (XANES) zeigt, dass die Cluster nicht oxidieren, solange Graphen vorhanden ist. Die Fähigkeit von Sauerstoff, sich auf Graphen abzuscheiden, wird dazu genutzt, um das Graphen kontrolliert zu ätzen.

und die Cluster wieder der Atmosphäre auszusetzen. An diesem Punkt ist die CSLM bereit, in Experimenten zur Nano-Katalyse eingesetzt zu werden.

Der wissenschaftliche Anhang enthält zusätzliche Informationen zu h-BN basierten Cluster-Übergittermembranen. TEM wurde verwendet, um zu bestätigen, dass die Cluster nach der Entfernung vom Substrat in der a-C-Schicht geschützt sind. Elektronenbeugung zeigt das Vorhandensein von h-BN. Eine Serie von Ausheilversuchen bestätigt die Stabilität und den Sintermechanismus der Cluster-Übergitter in den Membranen bis zu 1050 K. TEM Messungen bei 1350 K liefern direkte Hinweise auf Sintern durch Partikelwanderung und Koaleszenz.

Frequently used Symbols and Abbreviations

a-C	-	amorphous carbon
ALD	-	atomic layer deposition
CSL	-	cluster superlattice
CSLM	-	cluster superlattice membrane
CVD	-	chemical vapor deposition
DFT	-	density functional theory
Gr	-	graphene
h-BN	-	hexagonal boron nitride
LEED	-	low energy electron diffraction
LH	-	Langmuir-Hinshelwood mechanism
PC	-	polycarbonate
PPC	-	polypropylencarbonate
PDMS	-	polydimethylsiloxane
PMC	-	particle migration and coalescence
PMMA	-	polymethylmethacrylate
STM	-	scanning tunneling microscopy
STS	-	scanning tunneling spectroscopy
SERS	-	surface enhanced raman spectroscopy
UHV	-	ultra high vacuum
TEM	-	transmission electron microscopy
XANES	-	X-ray absorption near edge spectroscopy
XPS	-	X-ray photoelectron spectroscopy
XRD	-	X-ray diffraction

Table of contents

Abstract	iii
German Abstract (<i>Deutsche Kurzzusammenfassung</i>)	v
1 Introduction	1
2 Background	5
2.1 Clusters in Catalysis	5
2.2 Templated Clusters	12
2.3 The Concept of Cluster Superlattice Membranes	16
3 Manuscript 1: Cluster Superlattice Membranes	21
4 Manuscript 2: Carbon Embedding of Pt Cluster Superlattices Templated by Hexagonal Boron Nitride on Ir(111)	37
5 Manuscript 3: Silicon Cluster Arrays on the Monolayer of Hexagonal Boron Nitride on Ir(111)	53
6 Transfer Methods for Cluster Superlattice Membranes	61
6.1 Introduction	61
6.2 Experimental Methods	62
6.3 Modified Bubbling Transfer Method	62
6.4 Effects of CSLM Preparation	64
6.5 Simple Carbon Side up Transfer	67
6.6 Turn-over Transfer	68
6.7 Conclusion and Outlook	72
7 Functionalization of Fe–Pt Cluster Superlattice Membranes via O Radical Etching	73
7.1 Introduction	73
7.2 Experimental Methods	74
7.3 Results and Discussion	74
7.4 Conclusion	78

8	Discussion and Perspectives	79
8.1	Cluster Superlattice Membranes	79
8.2	Carbon Embedding of Pt Cluster Superlattices Templated by Hexagonal Boron Nitride on Ir(111)	80
8.3	Silicon Cluster Arrays on the Monolayer of Hexagonal Boron Nitride on Ir(111)	82
8.4	Transfer Methods for Cluster Superlattice Membranes	83
8.5	Functionalization of Fe–Pt Cluster Superlattice Membranes via O Radical Etching	85
8.6	The Future of CSLMs	86
9	Scientific Appendix: h-BN Based Cluster Superlattice Membranes	89
10	List of Publications (<i>Liste der Teilpublikationen</i>)	95
	Bibliography	97
	Lebenslauf (<i>Curriculum Vitae</i>)	123

1 Introduction

The origins of catalysis can be traced back to the earliest human practices of utilizing fermentation to produce alcohol. Even before a systematic understanding of catalytic processes emerged, humans frequently employed catalysts without realizing it. Early usages of the word catalysis refer to a "magical catalyst" that would help alchemists convert base metals into gold. It was not until 1835 when Jöns Jacob Berzelius recognized the recurring phenomenon of accelerated chemical reactions, that the term "catalysis" as we understand it was coined [1]. In his words:

"The catalytic power of substances seems to depend upon their ability to awaken the dormant affinities of other substances by their mere presence and not by their own affinity."[2]

He based his ideas on experiments by his contemporaries like Sir Humphry Davy, who suggested in 1817, that the presence of Platinum could lead to combustible gases mixed with oxygen to explode below their usual ignition temperature [3]. Further experiments with Platinum quickly proved its potential, e.g. by Edmund Davy who showed in 1820 that one can oxidise alcohol to acetic acid on the surface of Pt [4].

Today the global market for catalysts is estimated at USD 37.3 billion and is expected to hit USD 61.8 billion in 2030 [5]. The industrial significance of noble metal catalysts is undeniable, as they play a crucial role in various processes, such the production of medicine or cracking of petroleum hydrocarbons [6, 7]. Another notable example is their indispensable role in combustion processes aimed at reducing pollutant emissions [8]. Consequently, it becomes imperative to enhance the cost-effectiveness and efficiency of these applied noble metals. Typically, noble metals are utilized in the form of clusters, which are small particles comprising a few to a few thousand atoms. Clusters occupy an intermediate state between single atoms and bulk materials [9]. Given that catalysis occurs on the surface of particles, smaller clusters make more efficient use of the available atoms compared to larger bulk particles. However, the advantages of clusters extend beyond their surface-to-volume ratio. In this fascinating state of matter even a slight alteration by a single atom can significantly impact its properties, such as its magnetic

moment or reactivity [10, 11].

The study of clusters and their properties necessitates either highly localized probing techniques or obtaining a collective signal from a large ensemble of clusters. However, the dependence on the number of atoms within the cluster makes precise control of cluster size crucial. Otherwise, the information obtained becomes convoluted by variations in atomicity. One method to address this challenge is to select clusters based on their size and investigate them in a free beam [12–14]. However, this approach severely limits the available techniques for measuring the physicochemical properties of clusters.

A more effective approach involves supporting metal clusters on a surface, enabling the application of a wide variety of surface science techniques. One very precise method is the soft landing of size-selected clusters, which results in sparsely distributed and non-ordered clusters on the surface [15–17]. These clusters can then be studied using scanning probe techniques.

Another approach lies in the use of periodic templates, which can, by themselves, lead to the growth of ordered cluster arrays. The size distribution of the clusters templated for example by moiré reconstructions is narrow enough to study size dependent effects via averaging techniques like X-ray diffraction, X-ray photoelectron spectroscopy, or infra red spectroscopy [18–22]. Because all the clusters are of similar size and see the same environment it is possible to infer information about processes on single clusters from the averaged signal [23]. One of the main disadvantages of these systems however is their tendency to sinter under catalytic conditions (e.g. high temperatures and pressures).

In this work we will use carbon embedding to stabilize cluster superlattices against sintering. In the endeavour to apply the embedded clusters as model catalyst, a novel free-standing 2D material, the cluster superlattice membrane (CSLM) is developed. This material houses the cluster array on their template inside an amorphous carbon layer.

The growth steps of the fabrication, which are performed in ultra high vacuum (UHV) conditions are observed using scanning tunnelling microscopy (STM) and low energy electron diffraction (LEED). STM enables one to study the stability of the CSLs, find the adsorption areas of clusters and pin point the attachment areas of the carbon. LEED confirms the long range order over large areas of the sample. In addition, we employ XPS to further investigate this material. XPS provides not only information about the chemistry of the membrane, but enables us to see below the amorphous carbon coverage to study intercalation effects, which are hidden from LEED and STM. Optical microscopy is used to study the delamination process of the CSLM from its growth substrate. The free standing 2D material is stable in ambient conditions and as such enables further ex situ studies. Surface sensitive XRD and TEM provide additional information about the order and stability of these systems.

This thesis is structured as follows: In Chapter 2 the general concept of catalysis and the role of clusters in the field are introduced. The issue of catalyst deactivation and strategies to mitigate it are laid out. An overview about templated cluster systems and their applications are provided. Finally the concept of the cluster superlattice membranes is described as a means to combat shortcomings of other templated cluster systems and lay out a new avenue to fabricate a stable model catalyst.

In the following experimental chapters the main findings of this thesis are presented: Chapter 3 describes the base fabrication methods and results forming the CSLM. Chapters 4&5 both are work done on the templating layer of h-BN/Ir(111). First, the carbon embedding process of Pt clusters and the thermal stability of the system is studied, then the template is used to grow Si nano clusters. Chapter 6 serves as a manual how to handle the transfer of CSLMs to arbitrary substrates, a pre requirement to the work described in Chapter 7, which demonstrates the etching of the membranes via radical O.

Finally Chapter 8 provides a conclusion and a discussion of the experimental results. Future work to be done on the CSLMs is outlined. The Appendix 9 contains new findings about h-BN based CSLMs and their stability as a freestanding 2D material.

2 Background

2.1 Clusters in Catalysis

The term catalysis describes the process of enhancing the rate of a chemical reaction by introduction of a catalyst, which remains unchanged by the reaction [24]. As the reaction proceeds, the catalyst forms intermediate compounds that ultimately lead to the production of the final product. The catalyst continues to be available to assist in the reaction of additional intermediate compounds, facilitating the reaction’s progression. Today, more than 85% of chemical products are made using catalysts [25].

Catalysts can be classified into two categories based on their physical state relative to that of the reactants. Heterogeneous catalysis refers to those processes in which the catalyst and the reactants are in different states of matter. For instance, a metal catalyst promoting reactions involving gases [26]. On the other hand, homogeneous catalysis refer to those where the catalyst and the reactants are in the same state of matter, such as acid catalysis [27].

Supported catalysts belong to the heterogeneous category and involve catalytically active metals supported on various types of substrates. Deposition of the metal on the substrate is typically performed via chemical preparation methods which facilitate the industrial scale deposition of small metal particles on substrates (for further information the reader is guided to References [28–30]). While metal thin-films have been studied for their catalytic activity, it is technically difficult, if not impossible, to coat substrates, as they typically are three dimensional structures, limiting the carry over of results [31]. The support, typically porous metal oxides, zeolites or carbon, provides a structural, stabilizing framework for metal particles [32]. Supported metal catalysts are extensively used in industrial settings, e.g. car exhaust treatment, cracking of petroleum hydrocarbons or clean energy technologies [33–36]. These industrial applications also lead to high requirements for the catalysts, pertaining, but not limited, to their activity, stability and cost which drives research in the field [37]. All of those properties are tied, in one way or the other, to the size of the metallic particles.

2 Background

One of the immediately obvious aspects of shrinking catalytic metal particles down to microscopic crystallites is their superior surface to volume ratio, optimizing the available surface, which can facilitate the requested reactions [38, 39]. As the reactivity per unit of active material is increased the cost of a catalyst is reduced. Edges, different facets, and corners of the crystallites lead to a change in the coordination of atoms in the particles. Atoms in these positions can be more or less prone to adsorption or desorption of reactant species. This also positively impacts the reactivity of a catalyst, thus smaller particles are favoured [40, 41]. These small particles are referred to as clusters, entities bridging the space between atoms and the bulk material. The regime in which the aforementioned effects scale in proportion to the size of the cluster is referred to as the scaling regime.

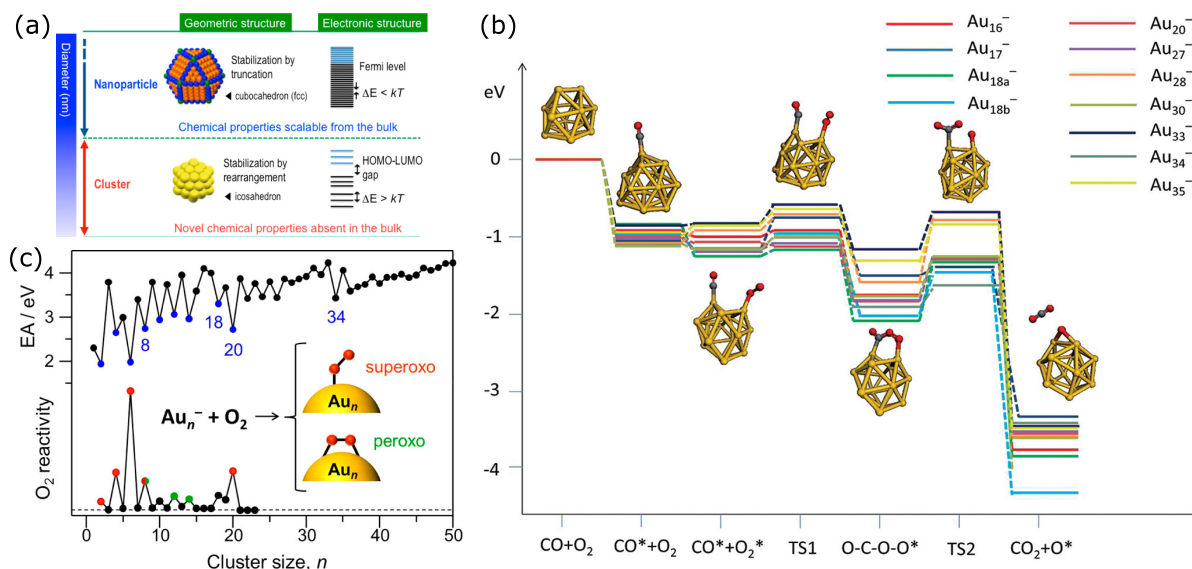


Figure 2.1: (a) Sketch detailing the change in geometric and electronic structure between a crystalline nanoparticle and a cluster. (b) Reaction pathways of $\text{CO} + \text{O}_2 \rightarrow \text{CO}_2 + \text{O}$ associated with various neutral gold clusters in the size range of Au_{16} to Au_{35} . Here, * denotes the adsorbed species on a gold cluster. (c) Correlation between the electronic structure (electron affinity measured by UV photoelectron spectroscopy) of Au clusters and O_2 reactivity predicted by ab initio calculations. (a),(c) Adapted from Ref.[42]. Copyright 2011 American Chemical Society. (b) Adapted from Ref.[43]. Copyright 2014 American Chemical Society.

By further reducing the size to the nanometer and sub-nanometer scale, clusters enter the non-scaling regime, where the effects of quantum mechanics set in, which can transform catalytically inactive bulk metals such as gold into active nanoparticles [44, 45]. This is happening because, as the number of atoms in a particle decreases, the former energy band of the metal starts to split up into discrete energy "molecular" orbitals and finally, in the limit of single atoms, into

atomic orbitals (see Figure 2.1 (a)) [46]. The split into molecular orbitals leads to the appearance of a highest(lowest) (un)occupied molecular orbital (HOMO/LUMO) [43]. The adsorption energies of CO on Au clusters supported on TiO_2 have been studied via infrared reflection absorption spectroscopy, which shows an increase right after crossing into the non-metallic nano cluster regime [47]. This also influences reaction pathways of species like CO and O_2 , depicted in Figure 2.1 (b), that depend strongly on the gap between these molecular orbitals and the geometric structure, which change strongly with the atom number of the clusters [42, 48, 48]. Ultra violet (UV) photoemission spectroscopy measurements of the electron affinity (akin to the work function of bulk materials) of Au clusters with fewer than 30 atoms have shown great variations with the atomicity [49]. These variations are also represented in the predicted reactivity towards O_2 adsorption, as shown in Figure 2.1 (c) [50].

Another interesting effect on catalytic performance of Au nanoparticles stems from the presence of a surface plasmon, a collective excitation of valence electrons. The exact energy of this excitation depends, among other factors, on the size of the particle [51, 52]. In the case of nanometre sized Au particles the absorption band lies in the visible spectrum and thus enables gold to transfer charges when exposed to light, making it a viable photocatalyst [53, 54]. Other metals such as Au and Cu in nanoparticle form exhibit similar photocatalytic properties [55, 56].

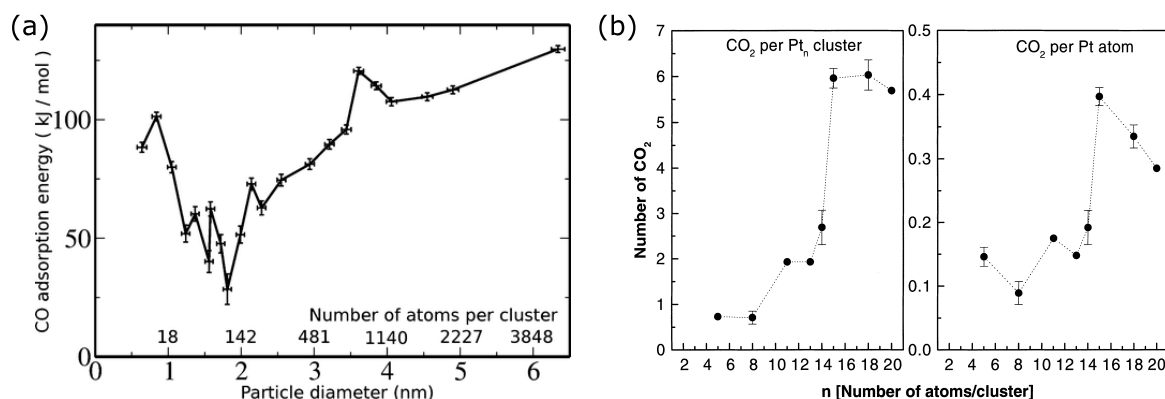


Figure 2.2: (a) Evolution of CO adsorption energy with Pd clusters size. The nonmonotonous variations of the adsorption energy observed in the smallest size regime (i.e., diameter below 1.5 nm or below 100 atoms per cluster) are attributed to the molecular nature of clusters on that scale. Adapted from Ref.[57]. Copyright 2013 American Chemical Society. (b) Left side: total number of catalytically produced CO_2 molecules as a function of cluster size. Right side: total number of produced CO_2 molecules per atom as a function of cluster size. Adapted from Ref.[58]. Copyright 1999 American Chemical Society.

The influence of the particle size on the catalytic performance has also been studied extensively in Pt group metals [59–64]. It can be seen, for example, in the adsorption energies of CO on

Pd particles, depicted in Figure 2.2 (a), which varies strongly for particles below a diameter of 4 nm and asymptotically approaches its bulk value for larger particles, clearly demonstrating the scaling and non scaling regime of clusters [57]. This dependence can also be observed in Figure 2.2 (b) in the oxidation of CO to CO₂ on Pt clusters, with Pt₁₅ clusters having been shown to be most reactive, again illustrating the importance of controlling the atomicity of clusters [58].

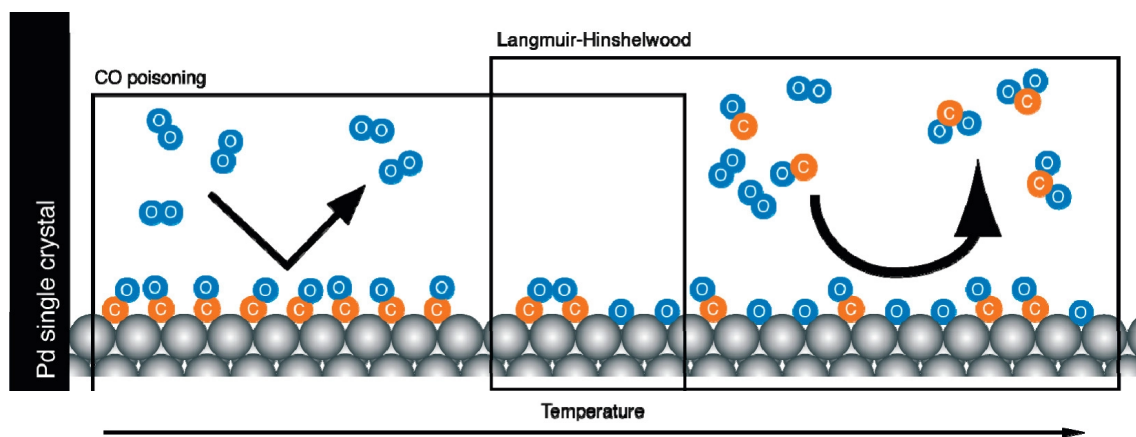


Figure 2.3: Mechanism of CO oxidation on Pd(111) single crystal. At lower temperatures the performance of the CO oxidation is limited by CO poisoning. At higher temperatures CO lifetime on the catalyst is limited, and CO oxidation occurs via the Langmuir-Hinshelwood mechanism. In the transition zone, both regimes overlap leading to a lower reactivity. Adapted from Ref.[65]. Copyright 2010 American Chemical Society.

To provide an example of the mechanism of a catalysed reaction, the oxidation of CO on a single crystal surface of Pt group metals, depicted in Figure 2.3, will be discussed briefly. The chemical reaction is given by:



and follows the so called Langmuir–Hinshelwood (LH) mechanism, in which both constituents adsorb on neighbouring sites of the catalyst and undergo a reaction [66]. O₂ adsorbs dissociatively on the Pt surface and can react with adsorbed CO [67]. The formed CO₂ desorbs from the surface, opening it up to further reactions [68]. For the LH mechanism to take place it is necessary that no one adsorbate species is blocking access to the adsorption sites. This makes the space requirement for the adsorption processes an important factor. CO requires a single free site to adsorb, while the dissociative adsorption of the O₂ leads to the single O atoms to be spaced by two lattice constants. Thus CO can form dense adlayers, poisoning the Pt surface

and preventing the reaction [69]. This is especially problematic at low temperatures, as not only the space requirement of CO on Pt is lower than that of O₂, but also the O₂ activation is decreased, further inhibiting the reaction [65]. Once formed a CO adlayer usually requires removal via high temperature annealing to reform the catalyst [70].

Moving away from catalysis on flat single crystal surfaces to more complicated surfaces requires the inclusion of steps, kinks and other structural defects that lead to under-coordinated atoms, which in turn influence the process [71–73]. Extending the description even further to supported nano clusters not only requires including the geometry and electronic states of the clusters, but their interaction with the support as well (metal-support interaction). On the one hand, strong metal support interaction (SMSI), which occurs in Pt group metals after chemical reduction in high temperatures on reducing substrates like TiO₂, has shown to greatly diminish catalytic activity [74]. On the other hand, supports can actively promote the reactivity of clusters either via spill-over effects or by actively supplying oxygen in the so called Mars-Van Krevelen mechanism [75, 76]. All these complicated, interwoven effects appearing even on simplified systems show that a true, complete understanding of applied catalysts is still far out and demonstrate the need for model catalyst systems in which factors like cluster size, spacing, atomic make up and support can be precisely controlled.

Degradation of Catalysts

Catalysts pose fundamental challenges which, in order to improve their performance in applications, have to be overcome. A catalyst needs to be specific and efficient. A perfectly specific catalyst only facilitates the desired reaction and no unwanted by-products are formed. The efficiency of a catalyst governs how fast a reaction takes place and how much of the actual catalytically active material is needed, as well as how resistant to degradation the catalyst itself is. All catalysts suffer from degradation in some form and while some of the deactivation mechanisms are reversible most of them aren't, making it imperative to design the catalyst in such a way that degradation is limited as much as possible.

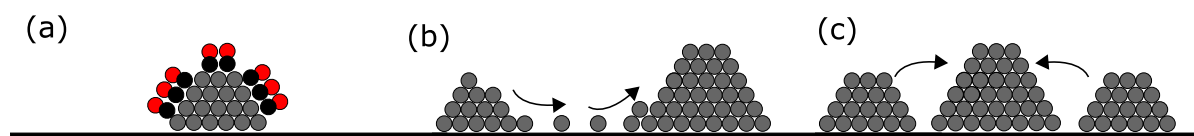


Figure 2.4: Mechanisms of catalyst deactivation. (a) Poisoning (for example via CO), (b) Ostwald ripening, (c) particle migration and coalescence (PMC)

Degradation of catalysts happens in a number of ways, for example through chemical deactivation (poisoning), mechanical deactivation (deformation/abrasion or fouling) or thermal/-chemical deactivation via sintering. Poisoning, which has been discussed above, happens when species strongly adsorb in the catalytically active sites of the catalyst, blocking access to these sites and thus deactivating the catalyst (see Figure 2.4). Mechanical deactivation can be either caused by abrasion of the catalytically active metals or the support, or by fouling which is a process in which the pores of the support get blocked leading to reactants being unable to reach the catalyst itself. Sintering, meaning the coalescence of particles without crossing into the liquid phase, can be caused by chemical processes, but can always be thermally activated. The coalesced particles will either be less active due to the number of active sites decreasing or completely deactivated if their reactivity was dependent on their small size.

Minimizing the impact of all degradation mechanisms at once is a complicated task requiring the interplay of support, active metal, the purity of the reactants, their flow rate, the pressure and the temperature at play. Because the announced goal of this work is to specifically limit thermally induced sintering, the next part will focus on the mechanisms of sintering and present routes to stabilize catalysts against them.

Sintering can be categorized into two main processes: Ostwald ripening and particle migration and coalescence (PMC) - also called Smoluchowski ripening [77]. Ostwald ripening, shown in Figure 2.4 (b), describes a process in which atoms or molecules detach from one particle and agglomerate at others. The generalized Gibbs-Thomson equation states that the vapour pressure of smaller particles is higher than that of larger ones, due to their higher curvature. Statistically this leads to more atoms detaching from smaller particles and agglomerating at larger ones and thus to growth of larger particles and the consumption of smaller ones, explaining nature's tendency to favour larger over smaller particles.

PMC (Figure 2.4 (c)), on the other hand, describes sintering via migration of whole particles. If the binding to the substrate is low and the particles sufficiently mobile, they will move and once they get in close proximity of another particle, the energy gained by decreasing their total surface area will lead to a merger of the two particles.

As sintering is generally irreversible, it is an important goal to understand which process is dominant in any given system and how to rationally design a catalyst in a way that suppresses this deactivation [77]. However, the exact contribution of each mechanism of catalyst sintering is experimentally challenging to probe because the timescales of deactivation vary greatly from an initial rapid sintering in seconds [78, 79] to long term effects which stabilize after many hours [80]. Specialized experimental set-ups, such as transmission electron microscopes capable of operating at high T and pressures in the milli-bar regime are required to monitor the evo-

lution of particles in-situ as sintering only sets in under these conditions, further complicating the endeavour [81]. Another, experimentally less demanding, strategy involves the analysis of the particles after sintering. By measuring the particle-size distribution it can be possible to differentiate PMC, which is predicted to result in a log-normal size distribution with a tail towards the large particle sizes [82], from Ostwald ripening, where a tail towards smaller particle sizes and a sharp cut-off at higher sizes is expected [83]. Monitoring the average particle size over time and inferring information from the rate of change was another suggested way to nail down the sintering mechanism [83]. As the measured slope, however, is again dependent on the observed time-scale it is not entirely clear that it has mechanistic significance [77].

There are a number of strategies to stabilize catalyst nanoparticles that tackle one or both mechanisms: PMC and Ostwald ripening can both be influenced by the choice of catalyst support. If the catalyst particles are well anchored to the substrate, such as Pd clusters on Rh(111), sintering via PMC is heavily suppressed, whereas Ostwald ripening processes can be limited on substrates which limit the atomic diffusion [17]. Pt atoms dispersed on Al_2O_3 , for instance, will aggregate into clusters during CO oxidation because the CO adsorption on the Pt lowers its adhesion to the substrate, increasing its mobility [84]. A switch to CeO_2 greatly enhances the Pt stability due to the stronger bonding interaction with the Pt atoms [85–87].

Enclosing strategies that limit the mobility of particles can also be employed to suppress sintering. Overcoating of particles via atomic layer deposition (ALD) can be used in different ways to protect the catalyst [88]. An average overcoating of just 0.1 nm Al_2O_3 is sufficient to stabilize Pd nanoparticles during methane decomposition at 260 °C [89]. In this study the alumina coating was found to preferentially bind to corners and steps of the Pd particles, leaving the active Pd(111) surfaces exposed and stabilized. Overcoating, in general, needs to preserve access to the nanoparticles and methods have been developed to either grow porous overcoatings or fabricate pores after the growth, e.g. by thermal treatments [90]

Further important factors for the stability of supported metal nanocatalysts are metal loading and size distribution of the nanoparticles [80, 91]. Ostwald ripening specifically can be targeted by fabrication of catalyst particles which are very homogeneous, as it is driven by the difference in particle size. In the extreme case of size selected metal nano clusters this can lead to greatly improved stability as demonstrated by Wettergren et al. [16].

Bimetallic nanoparticles such as Pt–Rh or dual metal catalysts like Fe–Ni composites have shown to possess higher activity than their pure counterparts as well as improved stability [92, 93].

Combining these approaches, by choice of a suitable substrate, a narrow cluster size distribution and overcoating one can expect to greatly enhance a catalysts stability in harsh conditions.

2.2 Templated Clusters

Templated cluster arrays are a type of nanostructured material consisting of clusters patterned via a template that guides the placement and organization of the clusters. As such, nano cluster arrays possess great potential for use in catalysis [21, 39, 94, 95], but also in different of applications ranging from electronics [96] to sensing [97]. The properties of the clusters themselves such as size, shape, and composition as well as the geometry of the arrays are tunable, bestowing the systems with a lot of flexibility.

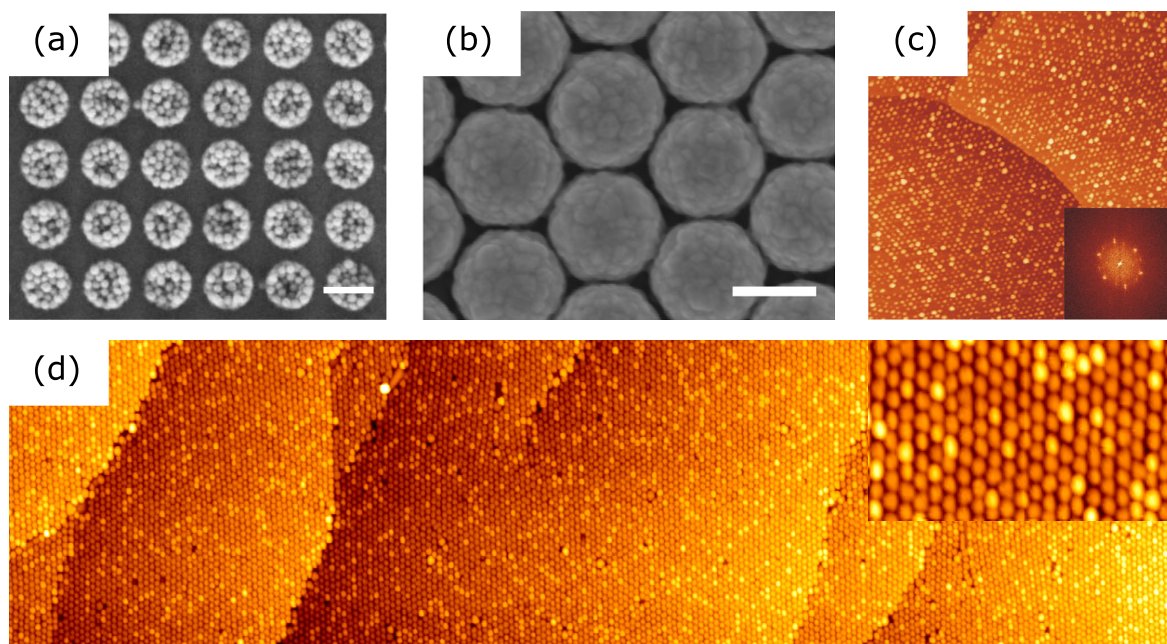


Figure 2.5: (a) Au nanoparticle cluster array, fabricated via e-beam lithography, with constant binding site diameter 200 nm and cluster edge-to-edge separation 50 nm. Scale bar is 200 nm. Adapted from Ref.[97]. Copyright 2009 American Chemical Society. (b) SEM images of 60 nm thick Ag deposited over SiO_2 nanosphere template, nanosphere diameter: 300 nm. The scalebar is 200 nm. Adapted from Ref.[98]. Copyright 2017 Elsevier B.V. (c) Ordered array of Au-Pd nanoparticles on a nanostructured thin alumina film on $\text{Ni}_3\text{Al}(111)$. STM image after deposition of 0.02 ML Pd and post-deposition of 0.04 ML Au at 300 K. Image size is 200 nm \times 200 nm. The insets show the corresponding Fourier transformation. Two domain structures of threefold symmetry with an angular difference in orientation of about 24° can be distinguished. Au atoms are captured exclusively by the Pd nanoclusters. As a consequence, ordered arrays of bimetallic Au-Pd nanoclusters are formed. Adapted from Ref.[99]. Copyright 2006 IOP Publishing, Ltd. (d) Ir cluster superlattice grown at 300K on Gr/Ir(111). Average cluster size is 70 atoms. Image size is 0.5 μm \times 0.13 μm . Inset is 500 \AA \times 300 \AA . Adapted from Ref.[100] under CC BY-NC-SA 3.0. Copyright 2009 IOP Publishing, Ltd.

Cluster arrays, like the one depicted in Figure 2.5 (a), come in a variety of different geometries, with a particle size and spacing in the 10 nm to 100 μm range. They can be fabricated via

direct electron beam writing on a positive resist and subsequent chemical vapour deposition (CVD) or ALD of the desired metal species [95]. After removal of the resist the patterned clusters remain on the substrate. By exploitation of sintering mechanisms it is even possible to fabricate nanoclusters with a size of 2 nm, albeit at the cost of large inter particle distances [101]. As prepared Au, Ag and bimetallic Au–Ag cluster arrays have been shown to strongly influence the surface enhanced Raman scattering (SERS) of different species and thus lend themselves to chemical and biological sensing [97, 102–104]. Ag nanocluster arrays on alumina prepared by e-beam lithography have been studied as a model catalyst in ethylene epoxidation [105].

A second fabrication method for periodic nano cluster arrays is based the substrate itself acting as template. This can be achieved by patterning the substrate before the deposition of the cluster material. One such template is porous anodic alumina which is prepared by a series of anodizations and removal of Al_2O_3 to form nanochannels in which the clusters can be deposited afterwards [106]. As prepared Ag clusters have been studied for their photoconductivity and as SERS sensors [107, 108]. Templating the surface with silica nanospheres allows a large scale patterning of Ag nanoparticles as depicted in Figure 2.5(b) [98].

A very elegant method for the stabilization of ordered cluster arrays emerges from the use of substrates that naturally form a template. These templates can cover large areas ($>1\text{ mm}^2$) which don't require an active patterning, opening the door for an easily scalable approach [109, 110]. One basis for such systems are ultra-thin oxide films on metals [111]. An FeO(111) layer on top of the Pt(111) surface has been shown to drive self organization of Au atoms due to its polar surface [112]. An alumina thin film on $\text{Ni}_3\text{Al}(111)$ can template metal nanoclusters such as Pd, Au–Pd, Cu and V with a regular spacing of 4.1 nm [99, 113, 114] (see Figure 2.5 (c)). Not all metals however are templatable, Ag and Mn clusters have been found to coalesce at higher coverages [114]. Au and Fe clusters templated by alumina have been studied for their catalytic and magnetic properties respectively [57, 115]. An overview of alumina templated cluster arrays can be found in Ref.[116].

Moiré reconstructions of 2D materials with their growth substrates, such as Gr/Ir(111) or h-BN/Rh(111) are also able to efficiently template cluster superlattices. Early experiments using the moiré of Gr/Ir(111) to grow Ir clusters (depicted in Figure 2.5(d)) have opened the field to a multitude of different templating systems [117]. Today W, Ir, Pt, Ru, Re, Rh, Sm, Ni, Co, Fe and Au clusters have been grown on graphene or h-BN on Ir(111), Pt(111), Ru(0001) and Rh(0001)[100, 118–125]. The best organization of clusters has been found in Ir on the moiré of Gr or h-BN on Ir(111) [116, 126]. Ir cluster superlattices stabilized on Gr/Ir(111) are highly stable and will start degrading only above 550 K. Some materials such as Co and Au, which do

not form well defined cluster superlattices at room temperature, can either be seeded by one of the better organized metals or deposited at lowered temperatures (200 K) to improve their order [100, 127].

Because of their controllable cluster size and regular spacing templated CSLs have already been studied as model catalyst systems. Martinez-Galera et al. have shown in a combined STM and XPS study, that Ir clusters templated by h-BN can be treated by O₂ exposure to remove carbon species and are capable of CO oxidation without sintering under reaction conditions [128]. The group of Christian Papp has extensively studied clusters on Gr or h-BN on Rh(111). Due to the great long range order of these systems it is possible to apply XPS as a probe to understand processes happening in a single moiré unit cell of the system. This way they have studied the adsorption and decomposition of ethene on Pt/h-BN/Rh(111) and were able to elucidate the roles of edges and facets of the Pt clusters, as well as establish a new reaction pathway, not present on the Pt(111) surface [129]. Similarly, they were able to study the CO adsorption on Gr/Rh(111) templated Pt and Pd particles [21, 125]. However, due to their limited stability, these systems are prone to sinter under harsher conditions and are thus only applicable in carefully designed experiments.

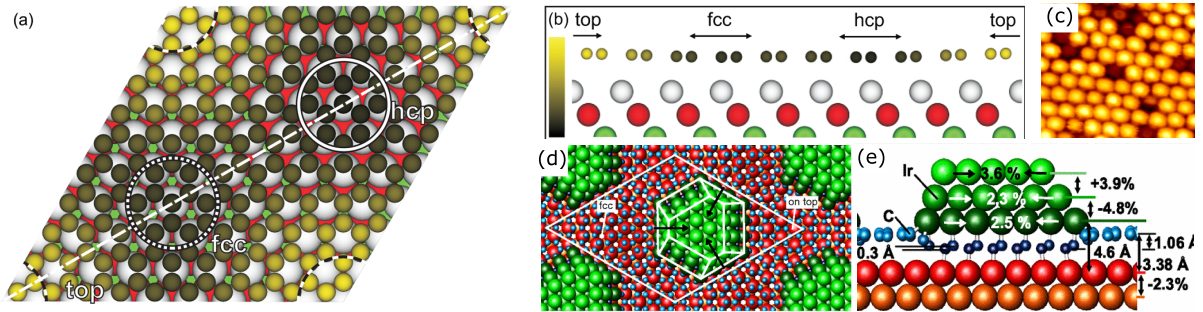


Figure 2.6: (a) Top view and (b) side view [cut along the dashed line in (a)] of the relaxed structure of graphene/Ir(111) obtained by DFT including vdW interactions. Regions of high-symmetry stacking (fcc, hcp, top) are marked by circles (a) or arrows (b). Adapted from [130]. Copyright 2011 American Physical Society. (c) STM topograph of 0.4 ML Ir clusters on Gr on Ir(111). Size is 22 nm×20 nm. (d) Top view of a structural model of Ir clusters on Gr/Ir(111). The moiré unit cell is indicated by the white line. High symmetry sites are marked, where the center of the carbon rings is located either at an fcc or on-top site with respect to the substrate. The center of the nanoparticles is located at the hcp position of the carbon rings. (e) Cross-sectional side view of the particles together with relaxation values derived from SXRD fits. Not all C atoms are shown for clarity. Adapted from [18]. Copyright 2013 American Physical Society.

As the stabilizing mechanism of clusters on Gr/Ir(111) is especially important in the scope of this work, a more in depth explanation is provided: Graphene forms a moiré reconstruction, displayed in Figure 2.6 (a), with a periodicity of 25.3 Å on the Ir(111) substrate due to the

slight difference in lattice constants ($a_{\text{Ir}} = 2.72 \text{ \AA}$ and $a_{\text{Gr}} = 2.45 \text{ \AA}$) [109]. In these 10.32×10.32 Gr unit cells on 9.32×9.32 Ir unit cells, three high symmetry points, namely the hcp, fcc and top region, can be identified. Due to the change in relative horizontal positions between Ir and C atoms in these regions, different relative heights are exhibited between the layers (see Figure 2.6 (b)) [130]. In the hcp regions, where C atoms sit directly atop the Ir atoms the C $2p_z$ orbital hybridizes with the Ir $d_{3z^2-r^2}$ orbital, locally giving the graphene an sp^3 like character [117]. These rehybridizations of the C atoms directly atop the Ir atoms then disturb the π bonds of the graphene, activating the neighbouring C atoms, which in turn can anchor metal atoms that are deposited on the graphene, forming the seeds for the cluster superlattice. As more and more metal atoms are deposited and attach to the cluster seed more C atoms rehybridize, further anchoring the cluster. A STM topograph of the cluster superlattice together with a structural model are shown in Figure 2.6 (c) and (d). The rehybridizing from sp^2 to sp^3 C bonds can be seen in x-ray photoelectron spectroscopy (XPS) measurements of the C1s core level and is consistent with density functional theory (DFT) calculations, as well as structural relaxation fits to SXRD data (see Figure 2.6 (e)) [18, 131, 132]. This mechanism also offers an explanation for the different thermal stabilities observed in metal clusters. Metals with extended d orbitals, which essentially are the binding component of the cluster material to the graphene, have been found to have the highest thermal stability [100].

h-BN/Ir(111) offers another versatile template for the growth of cluster superlattices [126, 133].

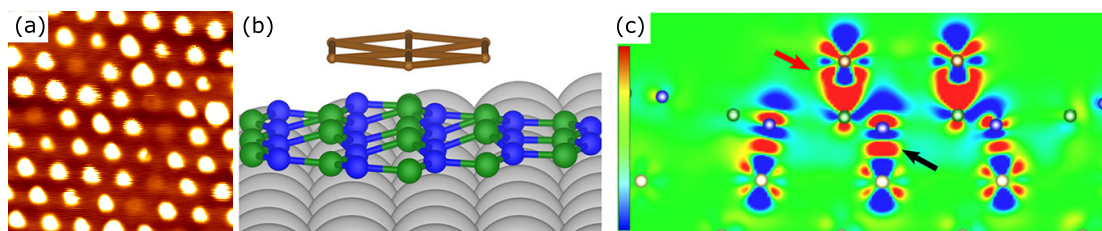


Figure 2.7: (a) STM topograph of 0.02 ML Pt on h-BN on Ir(111). The scale is $18 \text{ nm} \times 18 \text{ nm}$. (b) Relaxed DFT geometries of an Ir heptamer (brown balls connected by sticks) on h-BN on Ir(111). Perspective view, highlighting buckling of h-BN with B atoms approaching the Ir heptamer atoms and N atoms approaching the Ir substrate atoms. (c) Charge density difference between relaxed system and subsystems of Ir cluster, h-BN, and Ir substrate without changing atomic coordinates within each subsystem. Adapted from [126]. Copyright 2018 American Chemical Society.

The mechanism is similar to that of the Gr/Ir(111) system. The h-BN ($a_{\text{h-BN}} = 2.48 \text{ \AA}$) forms a 29.1 \AA periodic moiré reconstruction on the Ir(111) substrate, in which a central $B_{\text{hcp}}N_{\text{top}}$ region can be identified that is able to stabilize clusters (Figure 2.7 (a)) [126, 134]. In this region the h-BN buckles when metal atoms are deposited on top, with the N atoms moving towards the substrate, while the B atoms move towards the cluster atoms (see Figure 2.7 (b)).

Figure 2.7 (c) shows a charge density difference plot, indicating strong sp^3 hybridization of the h-BN below the clusters. This mechanism leads to a large energy gain for the cluster, making the as grown cluster superlattices even more stable than their Gr/Ir(111) counterparts, with Ir cluster superlattices being stabilized up to 700 K [126].

2.3 The Concept of Cluster Superlattice Membranes

Cluster superlattice membranes (CSLMs) are a novel type of heterogeneous 2D material being developed within the scope of this work. They consist of three main components: A templating layer - Gr or h-BN - on which the second component, a cluster superlattice, consisting of clusters evenly spaced nanometres apart, is grown. The third defining component is an embedding layer, which, in this work is an amorphous carbon layer [135]. The goal for this new material is to stabilize the cluster superlattice, enabling it to withstand even higher temperatures and ambient or catalytic conditions without sintering.

The choice of templating material determines the exact cluster lattice spacing, but also offers the opportunity to either grow on a conducting (Gr) or an insulating (h-BN) template. Also, the binding mechanism between templating layer and embedding matrix is dependent on this choice, possibly enabling different fabrication steps.

The cluster superlattice itself can consist of the wide variety of different cluster materials discussed earlier and all possible bi- or multi-metallic nano cluster combinations. The clusters are scalable in size from the single atom limit up to a few hundred atoms, following a narrow Poisson size distribution [117].

For the embedding layer carbon is a natural choice, as C can easily be deposited from the vapour phase in atomic, dimer and trimer form, forms cage-like clusters on Gr, while forming stable bonds with it [136]. It also strongly adsorbs on Pt/Ir, adhering perfectly to the noble metal clusters and forms a conformal embedding without disturbing the long range order of the cluster superlattice [132, 137]. The carbon embedding greatly stabilizes the clusters against sintering via PMC up until 1050 K. However, one can imagine many other embedding materials, each coming with unique advantages and challenges. From oxide supports which actively increase catalytic performance like TiO_2 , Al_2O_3 or CeO_2 , to elemental B to electrically isolate the clusters from one another. The thickness of the embedding layer is another tunable quantity, with extremely thin coverings like 1 nm Al_2O_3 possibly offering both stabilization and catalytic access [89, 90], while thicker layers in the multi nano metre range can further increase mechanical and thermal stability. A heterostructure of different embedding materials could be used to further bestow functionality to the system. For example, a thin carbon coverage followed by a thin film

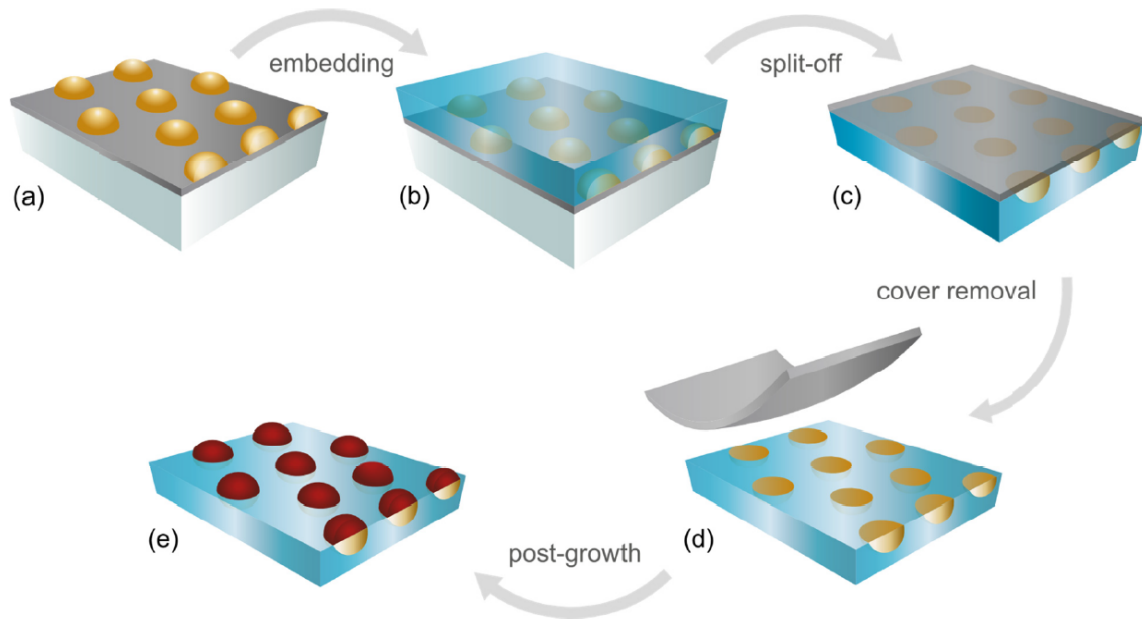


Figure 2.8: Concept sketch detailing the fabrication steps of a cluster superlattice membrane. (a) Growth of a templated cluster superlattice. (b) Embedding of the cluster superlattice. (c) Split-off of the membrane from the growth substrate. (d) removal of the templating layer. (e) Post-growth of the clusters.

of lead could be used to induce superconductivity in the clusters via proximity effect [138, 139].

The fabrication of CSLMs follows from the role of the components and is laid out in Figure 2.8. First, the templating layer is grown on a clean Ir(111) substrate, following an inhouse developed recipe described in Refs. [126, 132]. CVD grown Gr or h-BN can cover large scale areas of the sample, providing the basis for millimetre sized membranes. Cluster superlattices are grown in situ via e-beam evaporation of metals onto the templating layer (Figure 2.8 (a)) [100, 126]. Figure 2.8 (b) shows the membrane after the stabilizing embedding matrix has been grown. The embedding is done via evaporation of material from an e-beam or a Knudsen cell. At this point the clusters are full covered by the a-C layer and protected against sintering via PMC [132]. Application as a model catalyst however, is impossible at this point, because no reactants will be able to reach the catalytic particles. Thus, the next following idea is to turn the membrane around and remove the templating layer. This should, if successful, leave the clusters stabilized by the embedding matrix like eggs in an egg carton. To this end, first the removal from the substrate is necessary (Figure 2.8 (c)). Since the bonds between templating layer and the substrate are enhanced during the previous growth steps it is necessary to weaken them again before a large scale transfer is possible. One strategy for the reduction of binding

of a carbon based membrane is an annealing step to 750 K, which leads to a restructuring of the amorphous C matrix to a more sp^2 like network [135]. A second option is the intercalation of different species into the space between the Gr and the Ir(111). Candidates for this are K, Br, Cs, Eu, or Li [140–143].

The hydrogen bubbling method is the basis for the delamination of the CSLM from the Ir substrate [144]. After the preparation the crystal is removed from the UHV, covered by a polymethylmethacrylate (PMMA) support layer (either drop casted or spin-coated) and subjected to a standard hydrogen bubbling transfer, finally forming the free-standing hybrid 2D material (see Figure 2.8 (c)) [135].

One necessary requirement for the application of CSLMs as a model catalyst is the partial or full removal of the templating layer, allowing reactants to reach the encapsulated clusters. An opened CSLM is depicted in Figure 2.8 (d). Possible ways to remove the templating layer include etching with oxygen or argon plasma. However, it is extremely important to choose an approach which does not also damage the embedding matrix, meaning that either one has to be very careful when using the oxygen approach, or the matrix has to be made from a material which resists the etching agent.

Once opened, post growth of the cluster superlattice (Figure 2.8 (e)) can be performed to either improve the properties, or bestow new functionality in the clusters by depositing different metal species on the opened CSLM.

Future research opportunities for the CSLMs are found foremost in the field of catalysis. The variety of possible cluster materials and sizes, combined with different supports and the predicted high temperature stability lend themselves to experiments in high pressure and temperature regimes, which lead to sintering in other supported systems. The narrow size distribution and long range order of the systems allow the investigations of spill over and reverse-spill over effects, as well as the determination of the cluster shape during reactions. The ability to tune the size of the clusters down to the atomic limit also enables studies into single atom catalysis, an emerging field which makes optimal use of the catalytic metal atoms [145, 146]. As the interaction between the single atoms and their support is even more important in single atom catalysts than in nanoclusters, the choice of embedding material enables to study the interaction effects in otherwise unchanged conditions [147–149]. Ideally, this capability will help bridge the pressure gap in catalysis, which separates the understanding of traditional model systems from industrial catalysts [150].

Closely related to its potential in catalysis, recently, a Pd CSL has been demonstrated to be an efficient hydrogen storage, displaying its capabilities for clean energy storage [20]. A CSLM based on Pd clusters, either seeded by Ir or post grown after the template removal, could pro-

vide enhanced stability for the CSL and prevent it from degrading during multiple absorption and desorption cycles.

Further applications include magnetism and phase formation. Magnetic properties of clusters, such as anisotropy and blocking temperature, depend on their size and shape [151, 152]. Their interactions are governed by their spatial orientation. The spatial distance can be controlled via choice of template and the size of the clusters is tunable through the deposited amount. The a-C matrix stabilizes both, protecting the clusters from sintering or oxidizing. The separation on the order of 1 nm lends itself to investigations into magnetic dipole–dipole interactions [153]. Connected to the opportunities in magnetism, phase formation can be studied in the cluster in the membrane. It requires significant energy for the clusters to escape their encapsulation, as they essentially have to either pass through the a-C, or penetrate the graphene layer. The penetration through the graphene layer has been observed on the substrate, as the chemical potential at the single crystal surface is lower than in the clusters. However, once removed from the growth substrate the driving force for this process would also be eliminated. Phase transitions, for example of Fe–Pt clusters into the magnetically highly anisotropic L1₀ phase, have already been investigated in similar systems. Sellmyer et al. have investigated the phase transformation of randomly deposited Fe–Pt clusters in an a-C matrix and Capiod et al. studied size selected and soft landed clusters, which don’t form a dense superlattice, on the Gr/Ir(111) template [154, 155]. The CSLM combines the advantages of both systems, enabling a high density of clusters with a narrow size distribution housed inside the protective a-C matrix.

3 Manuscript 1: Cluster Superlattice Membranes

This chapter wholly consists of the above-named manuscript and its supplement, published 10th of September 2020 at ACS Nano

The experiments were proposed by T. Hartl, P. Bampoulis and T. Michely. All sample growth and measurements performed at ATHENE were conducted by T. Hartl and S. Dellmann. Hydrogen bubbling experiments were performed in Zagreb, Croatia by T. Hartl and P. Bampoulis under the experimental guidance of D. Čapeta and M. Kralj. Raman spectroscopy measurements were performed by B. Senkovskiy and A. Grüneis. XPS measurements were taken at the Elettra Synchrotron in Trieste, Italy, by T. Hartl, M. Will, P. Bampoulis, P. Lacovig, VB. de la Cruz, S. Lizzit and J. Knudsen. TEM measurements were performed in Vienna, Austria by R. Singh, D. Scheinecker and J. Kotakoski in cooperation with P. Bampoulis. All work was supervised by P. Bampoulis and T. Michely.

The manuscript was written in close cooperation by T. Hartl, P. Bampoulis and T. Michely.

Some of the results shown in this chapter can be found in the Master's thesis of T. Hartl and the Bachelor's thesis of S. Dellmann.

Cluster Superlattice Membranes

Tobias Hartl, Moritz Will, Davor Čapeta, Rajendra Singh, Daniel Scheinecker, Virginia Boix de la Cruz, Sophia Dellmann, Paolo Lacovig, Silvano Lizzit, Boris V. Senkovskiy, Alexander Grüneis, Marko Kralj, Jan Knudsen, Jani Kotakoski, Thomas Michely, and Pantelis Bampoulis*



Cite This: *ACS Nano* 2020, 14, 13629–13637



Read Online

ACCESS |



Metrics & More



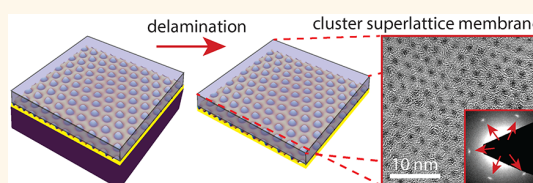
Article Recommendations



Supporting Information

ABSTRACT: Cluster superlattice membranes consist of a two-dimensional hexagonal lattice of similar-sized nanoclusters sandwiched between single-crystal graphene and an amorphous carbon matrix. The fabrication process involves three main steps, the templated self-organization of a metal cluster superlattice on epitaxial graphene on Ir(111), conformal embedding in an amorphous carbon matrix, and subsequent lift-off from the Ir(111) substrate. The mechanical stability provided by the carbon-graphene matrix makes the membrane stable as a free-standing material and enables transfer to other substrates. The fabrication procedure can be applied to a wide variety of cluster materials and cluster sizes from the single-atom limit to clusters of a few hundred atoms, as well as other two-dimensional layer/host matrix combinations. The versatility of the membrane composition, its mechanical stability, and the simplicity of the transfer procedure make cluster superlattice membranes a promising material in catalysis, magnetism, energy conversion, and optoelectronics.

KEYWORDS: nanocluster superlattices, membranes, two-dimensional materials, graphene, moiré



The large number of two-dimensional (2D) materials and their broad range of physicochemical properties have led to considerable efforts toward 2D material-based applications.^{1,2} In view of the respective application requirements, the integration of graphene (Gr) or other 2D materials with functional building blocks such as nanoparticles and molecular species is a strategy to design 2D materials with diverse functionalities. These 2D functional materials combine the exceptional properties of Gr (e.g., mechanical strength, flexibility, and electrical conductivity)^{3–5} with the desirable properties and functionalities of the respective nanoscaled building block.^{6–8} Examples of such hybrid materials are carbon nanomembranes^{9–14} and graphene-nanoparticle composites.^{8,15–17} Here we report on the fabrication of two-dimensional membrane material containing a superlattice of nanoclusters. This free-standing 2D membrane consists of a metal cluster superlattice encapsulated within a stabilizing framework of amorphous carbon (a-C) and Gr and is hereby referred to as cluster superlattice membrane (CSLM). The nanocluster building blocks within the free-standing membrane can be controlled in composition, have a narrow size distribution, a perfect long-range order, and their average size can be tuned during growth from the single-atom limit up to a few hundreds of atoms.

CSLMs are similar to graphene-nanoparticle composites^{8,15–17} and freestanding nanocrystal superlattices,^{18,19} because these materials host nanoclusters and nanoparticles within a stabilizing matrix. The well-defined and well-

controlled size and thickness of CSLMs also make them similar to carbon nanomembranes formed from cross-linked supramolecular networks.^{9–13} They are both largely non-crystalline, rigid, mechanically, and thermally stable 2D materials.

What distinguishes CSLMs from the above examples is the crystalline order of small clusters down to the atomic limit with a small, but not atomic, lattice constant. Lateral long-distance order is absent in graphene-nanoparticle composites,^{8,16,17} only possible by top-down lithography in carbon nanomembranes¹³ and only for large crystals (sizes from 10⁴ to 10⁷ atoms) and small areas in nanocrystal superlattices.¹⁹ In contrast, the clusters in CSLMs are positioned on a superlattice, which extends over macroscopic length scales (mm), with a lattice constant (2.53 nm) that is much shorter than the current state-of-art patterning. The identical environment and the similar size of the clusters in the superlattice can lead to a collective response to external stimuli and prevent smearing out single cluster features.^{20–22}

Received: July 10, 2020

Accepted: September 10, 2020

Published: September 10, 2020



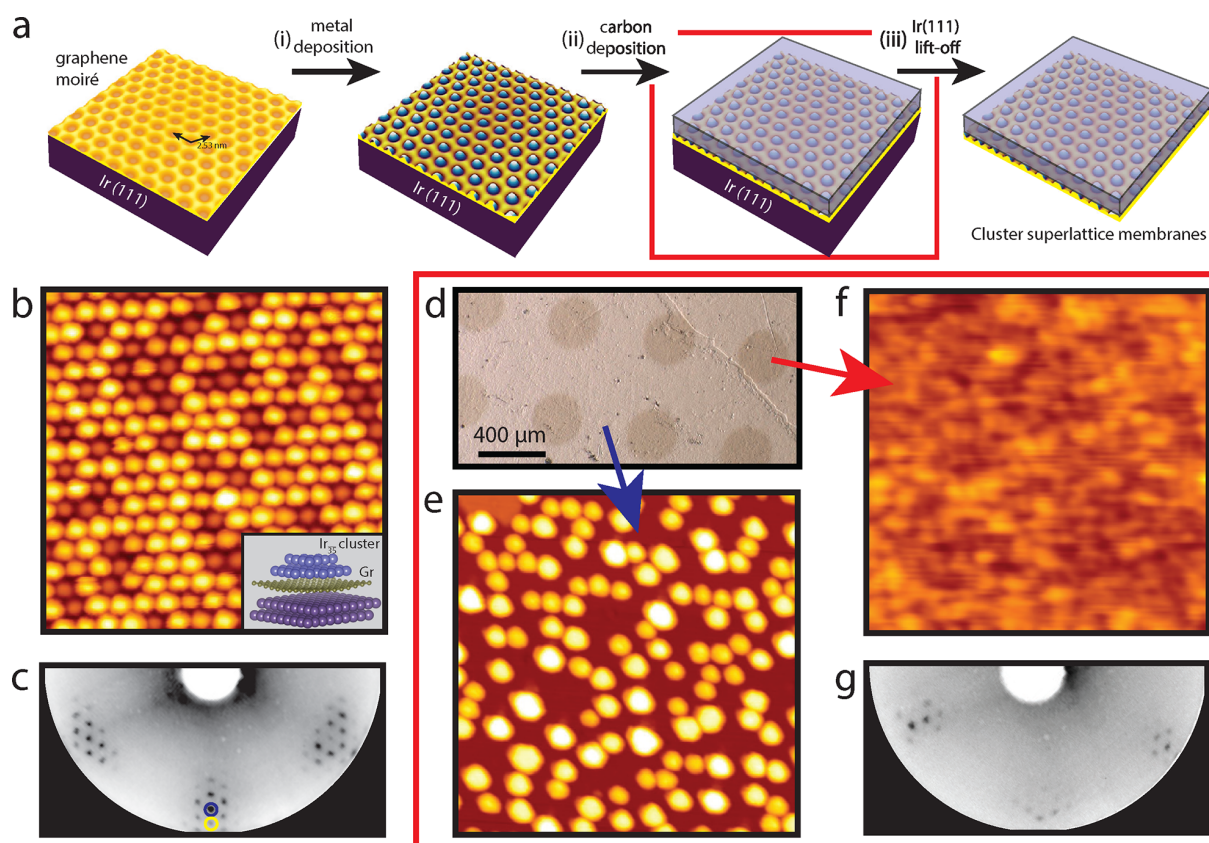


Figure 1. (a) The concept for the fabrication of the cluster superlattice membrane. (i) The growth of a cluster superlattice by metal deposition on the moiré of Gr on Ir(111), (ii) embedding of the cluster superlattice with elemental carbon, and (iii) lift-off from the metal substrate. (b) STM topograph of an Ir₃₅ cluster superlattice formed on the Gr moiré after the deposition of 0.4 ML Ir at 300 K. Inset: a structural model of the Ir₃₅ cluster on Gr/Ir(111). (c) The corresponding LEED image acquired at 72 eV. First order Ir (blue) and Gr (yellow) reflections are encircled. They are surrounded by moiré reflections. (d) Optical image of the Ir/Gr/Ir(111) sample after the deposition of 7 ML carbon through a shadow mask and annealed to 850 K. (e) STM topograph acquired at the regions where carbon is shadowed by the mask, and the Ir cluster superlattice has sintered due to annealing to 850 K. (f) STM topograph of a cluster superlattice embedded in 7 ML carbon and annealed to 850 K. (g) LEED image corresponding to (d) taken at 72 eV. The STM image sizes in panels (b,e,f) are 45 nm × 45 nm.

Moreover, CSLMs are also distinct from cluster arrays grown on a 2D template.^{23,24} Cluster arrays on templates require the presence of the substrate to maintain their order. They are sensitive and only of moderate stability with respect to temperature and gas exposure. CSLMs can be used as suspended sheets or on any substrate. They are robust, being insensitive to temperature variation, and are easy to handle due to their mechanical stability.

RESULTS AND DISCUSSIONS

Membrane Fabrication. The fabrication concept is schematically presented in Figure 1a. It involves three main steps: (i) the growth of a metal cluster superlattice on the Gr moiré on Ir(111), (ii) the embedding with carbon, and (iii) the removal of the carbon matrix-metal-Gr 2D hybrid sheet from the Ir(111) substrate. Step (i) is based on template growth of metal nanoclusters on a 2D layer, such as monolayers of Gr or h-BN on Ir(111).^{23–26} Metal deposition on Gr/Ir(111) induces local Gr rehybridization from sp² to sp³ carbon in the hexagonal close-packed (hcp) regions of the moiré, whereby chemical bonds between the C atoms and the cluster as well as with the substrate metal are formed. This

mechanism induces pinning of the clusters at the hcp areas, leading to cluster superlattice with the moiré periodicity of 2.53 nm.^{20,23,26,27} The clusters were found to have epitaxial growth with their dense-packed planes and their dense-packed directions parallel to those of Gr.^{20,26} Figure 1b shows an STM image of a such a cluster superlattice formed by deposition of 0.4 ML of Ir on the Gr moiré. The clusters' sizes display a Poisson distribution with an average size $s_{av} = 35$ atoms defined by the deposited amount; see the inset of Figure 1b for a structural model. As seen in the LEED pattern of Figure 1c, the Gr, Ir, and moiré reflections are clearly visible after cluster deposition. In contrast to the bare Gr moiré on Ir(111), Figure S1, additional moiré reflections are visible after cluster deposition, as characteristic for a highly ordered cluster superlattice with the same lattice constant as the Gr moiré that covers the whole surface.

The deposition of elemental carbon on the cluster superlattice leads to the conformal embedding of the clusters without disturbing their perfect lateral order; for more details see ref 28. Each cluster is encapsulated in a stable protective cap, which provides exceptional thermal stability against sintering for temperatures up to 1350 K and protection against molecular adsorption.²⁸

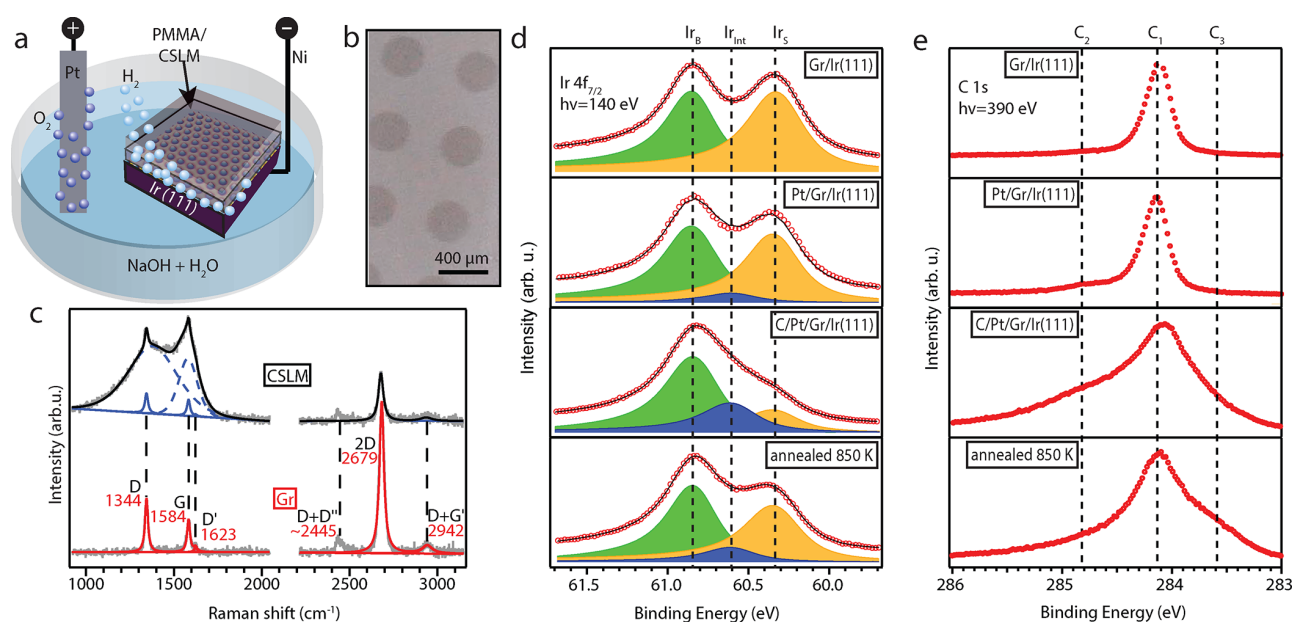


Figure 2. (a) Schematic of the electrolysis setup for the hydrogen bubbling transfer of the membrane. The membrane/Ir sample coated with PMMA is immersed in NaOH solution. The Ir sample serves as the cathode, whereas a Pt wire is the anode. (b) Optical image of the cluster superlattice membranes supported on PMMA. (c) Raman spectra of the free-standing cluster superlattice membrane (blue) and of graphene (red) using a 532 nm laser. (d,e) X-ray photoemission spectra of the Ir 4f_{7/2} and C 1s of the Gr/Ir(111) surface, Pt/Gr/Ir(111), C/Pt/Gr/Ir(111) at room temperature, and after annealing to 850 K, moving from top to bottom. To distinguish the cluster signal from the Ir(111) substrate, a Pt cluster superlattice was used instead of Ir.

To increase the yield of fabrication and enhance delamination (see below), we deposited carbon, step (ii), through a shadow mask of 48 regularly spaced circular holes with a diameter of 300 μm in a square grid arrangement as shown in Figure S2. The mask prevents carbon deposition at the parts of the sample below the shadowed regions. This way multiple cluster membranes can be fabricated at the same time and with identical preparation conditions. In addition, as a requirement for a successful electrochemical delamination (see below), after the deposition of C the sample is annealed to 850 K. The circular areas covered with 7 ML of carbon appear dark under the optical microscope and are surrounded by brighter carbon-free regions; see Figure 1d.

The STM image, depicted in Figure 1e, reveals that in masked areas without carbon the clusters sintered due to annealing. The sintered Ir clusters have an inhomogeneous size distribution and are not ordered. The carbon embedded areas display a rough surface without well-defined structure, see Figure 1f. In Figure 1g, the LEED pattern sampling of both areas with and without the carbon cover displays an enhanced diffuse background together with moiré reflections. We conclude that the moiré reflections must stem from the areas without the carbon cover, because after deposition of the same amount of C without a mask the LEED pattern is only diffuse (LEED is unable to probe the order of the cluster superlattice buried under 7 ML of C, see Figure S1). Therefore, the deposited layer must be considered to be amorphous carbon (a-C), a mixture of sp² and sp³ hybridized C without long-range order. At this step, the membrane's lateral size and shape can be controlled by using differently patterned shadow masks, and its thickness can be controlled by adjusting the deposited amount of carbon.

Transfer. To establish the membranes as a 2D material and in order to make use of them on different substrates, it is

necessary to delaminate them from Ir(111). For delaminating the cluster membrane from the Ir(111), we included two steps that reduce the membrane-Ir adhesion into the fabrication process. Prior to hydrogen bubbling and removal from the UHV chamber, the membranes were (1) heated to 850 K and (2) intercalated with Eu at 750 K. The heating step was decisive, see X-ray Photoemission Spectroscopy, for successful membrane removal, and the Eu intercalation improves further the yield of delaminated membranes. Intercalation of foreign species such as Eu between Gr and Ir(111) breaks the Gr–Ir interfacial bonds and further weakens the adhesion.^{29,30}

After removing the sample from the UHV, a reinforcing poly(methyl methacrylate) (PMMA) film is placed above the CSLMs. For electrochemical delamination, we used a setup similar to refs 31 and 32 shown in the schematic of Figure 2a. The sample is immersed into a 10% NaOH solution and used as the cathode, while a Pt wire serves as the anode. A low negative bias (slightly below the electrode potential of hydrogen evolution, ~1.6 V) is applied for a prolonged time (24 h) to the sample for underpotential intercalation of water and slow water reduction.^{33,34} After delamination, the CSLMs adhering to the PMMA, see Figure 2b, can be placed on a substrate of interest, e.g., SiO₂ or a TEM grid. The Ir crystal can be reused. We note here that the fabrication of smaller membranes (300 μm, through the use of a shadow mask) is beneficial, because the smaller lateral extension of the membranes allows for more effective intercalation of Eu and water and thus more efficient delamination.

Furthermore, attempts to remove unprocessed cluster membranes using conventional electrochemical delamination processes as applied for Gr layers grown on metal surfaces^{31,32} were unsuccessful. This points to a stronger adhesion between the cluster membrane and the Ir(111) surface compared to pristine Gr, which is due to hybridization of the carbon 2p_z

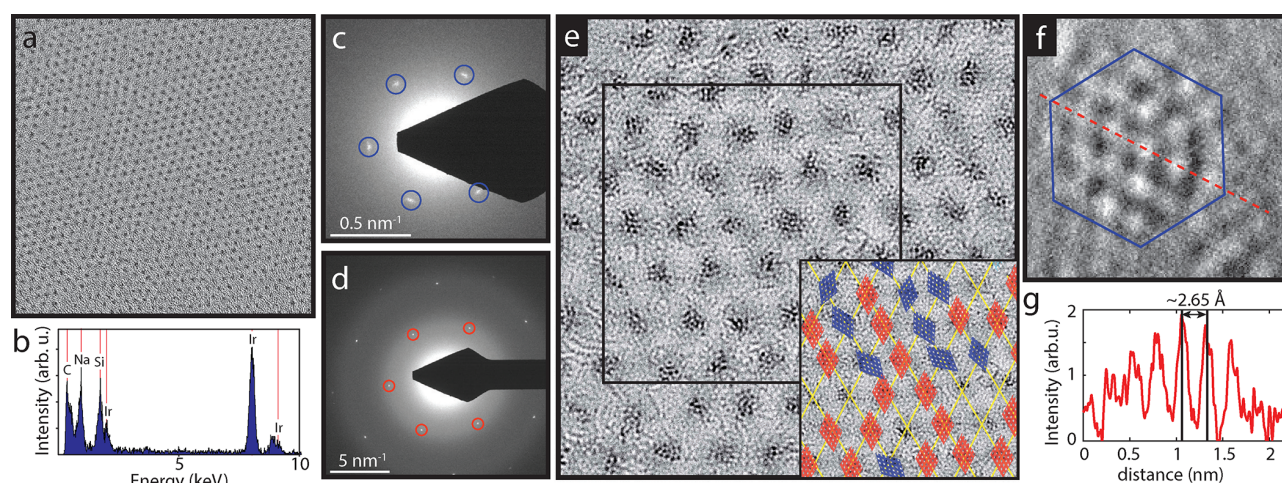


Figure 3. (a) Large scale (77 nm × 77 nm) HRTEM image of the cluster superlattice membrane. (b) EDX spectrum of the membrane showing a strong signal correlated to the presence of Ir. (c,d) Diffraction images recorded on the membrane, showing the cluster lattice (c) and the Gr lattice (d) spots, taken at different magnifications in reciprocal space. Both patterns cannot be represented in one reciprocal space image due to their vastly different scale. The first order spots are marked with blue and red, respectively. (e) A zoom-in HRTEM image (23 nm × 23 nm) of the cluster membrane, showing a closer look of the clusters' crystalline structure. Inset: sketch of the orientation of the clusters within the black square of panel (e); red indicates cluster epitaxy with the Gr lattice and blue shows randomly oriented clusters. (f) A zoom-in on a cluster having a lattice that resembles the (111) Ir plane; the image size is (2 nm × 2 nm). (g) The line profile corresponding to the red dashed line of panel (f).

orbitals of Gr with the substrate $\text{Ir}(d_{3z^2-r^2})$ after the deposition of clusters and capping C, see refs 27 and 35, and our own X-ray photoemission spectroscopy (XPS) results below. The increased binding hinders the intercalation of water and ions during the bubbling process and prevents delamination of the membrane.

To confirm the preservation of the Gr part in the membrane after transfer, we performed Raman spectroscopy characterization. Figure 2c shows the Raman spectra of the CSLM (blue) after transfer to a TEM grid and suspended graphene (red) taken from the region with sintered clusters, that is, the region not covered with a-C. The spectrum of graphene does not contain the contribution from a-C, and the single Raman peaks are fitted with the Lorentzian functions. We identify here the characteristic graphene G mode, defect-induced D and D' modes, and the double resonance Raman modes 2D, D+G', and D+D'.^{36,37} In the spectrum of the CSLM, the double resonance graphene modes are also clearly visible, whereas the G, D, and D' modes overlap with two broad a-C bands (at ~1379 and 1580 cm^{-1}) shown by the dashed lines. The a-C bands fitted with the combination (50/50) of Lorentzian and Gaussian functions are consistent with Raman data on a-C films.³⁸

X-ray Photoemission Spectroscopy. In order to understand the reasons why heating to 850 K is decisive for successful delamination, the UHV steps of the membrane fabrication process were studied with XPS. To be able to distinguish the cluster signal from the Ir(111) substrate, the Ir clusters were replaced with Pt following the same growth procedure as for Ir clusters but this time without the use of the shadow mask. Figure 2d shows the Ir $4f_{7/2}$ core level spectrum of 1 ML of Gr on Ir(111) surface.

The spectrum consists of two distinct peaks at 60.32 and 60.85 eV, corresponding to emission from the surface, Ir_S , and bulk, Ir_B , atoms, respectively.³⁹ Deposition of 0.35 ML Pt at room temperature reduces Ir_S and a new interface component, Ir_{Int} (blue in Figure 2d), appears, centered at 60.60 eV. The

interface component emerges from the Ir surface atoms now chemically binding to Gr. The reason is that due to Pt deposition and cluster formation, the Gr rehybridizes underneath the clusters. Thereby the rehybridized C atoms in Gr not only bind the Pt clusters but also form chemical bonds to Ir surface atoms whereby Ir_{Int} emerges and Ir_S diminishes.⁴⁰ Additional deposition of 2 ML carbon leads to a further increase of Ir_{Int} and a decrease of Ir_S as has been found before for C deposition on Gr/Ir(111).³⁵ The deposited C triggers rehybridization of a large part of the residual sp^2 -hybridized Gr and thereby in turn a transformation of bare Ir surface atoms contributing to Ir_S to Ir surface atoms binding to rehybridized Gr and thus contributing to Ir_{Int} .

As shown in Figure 2d, by heating to 850 K, the Ir_{Int} component decreases significantly while Ir_S recovers, suggesting that interface chemical bonds between the membrane and the Ir surface layer are partly released. Since the embedded metal clusters remain ordered after heating to 850 K under the C film,²⁸ the release of the Ir-membrane chemical bonds must be associated with reorganization in the membrane itself.

We have also tracked the C 1s core level at each relevant step, that is, Gr/Ir(111), deposition of clusters and carbon, and heating to 850 K, Figure 2e. The C 1s peak of pristine sp^2 bonded Gr is sharp and located at 284.12 eV (C_1). Deposition of Pt clusters leads to the formation of a Gr hybridization shoulder at 284.81 eV (C_2),²⁷ which is consistent with the appearance of the interface component Ir_{Int} . After the deposition of 2 ML C, the spectrum broadens as the result of the amorphous character of the deposited C in which the C atoms are in multiple unspecified configurations.

Heating to 850 K results in a reduction in the width of the spectrum, suggesting an increase of the amount of sp^2 bonds in the membrane. At the same time, a shoulder appears at the low binding energy (283.60 eV) side of the C 1s peak, marked as C_3 . One plausible explanation for its emergence is permeation of C through the Gr sheet to the Ir substrate (monomer permeation upon room-temperature deposition was noticed

before in ref 35 and 41), which in turn could result in the formation of small graphene clusters which provide a C 1s component at this location, as was shown by Lacovig et al.³⁹ We also note that room-temperature permeation could contribute to the Ir_{int} component of the Ir 4f_{7/2} core level.

Summarizing the observed changes in the Ir 4f_{7/2} and C 1s core levels, we argue that after heating to 850 K the C atoms in the membrane reorganize, and as a result the Gr–Ir substrate bonds formed during embedding are at least partly released. The resulting weaker binding between Gr and Ir allows for intercalation of water and explains the easier delamination of the CSLM.

Transmission Electron Microscopy. To confirm the presence and order of the metal clusters in the free-standing CSLM, we used high-resolution transmission electron microscopy (HRTEM). Figure 3a shows a large scale HRTEM bright field image of the membrane, where the Ir clusters can be recognized as dark spots forming a hexagonal lattice. The energy-dispersive X-ray spectrum of Figure 3b confirms the dark spots to be Ir clusters (Na and Si are residues from the transfer process). The average cluster diameter is measured to be 12 ± 2 Å, that is, close to the expected value for bilayer clusters of 35 atoms (note that the HRTEM images show a projection of the structure). The long-range periodic arrangement of the Ir nanoclusters is preserved throughout the membrane, evident from the superlattice diffraction pattern of Figure 3c, from which a superlattice parameter of 2.5 nm is derived.

The electron diffraction pattern of Figure 3d, taken at an order of magnitude larger magnification in reciprocal space confirms the presence of Gr in the membrane. Direct comparison between the diffraction patterns for the Gr lattice and the cluster superlattice reveals that the two lattices are generally well-aligned with only a slight deviation in orientation of 1.5° – 2° (note that the cluster superlattice spots are slightly elongated, suggesting domains of slightly different angles); see also Figure S3. Such a small misalignment is typical for a superlattice on Gr/Ir(111) and results from the angular spread of Gr on Ir(111) due to small angle grain boundaries,²⁵ which is magnified by a factor of 10 through the moiré. Moreover, the ratio between the graphene lattice constant and the superlattice constant, $\alpha_{\text{Gr}}/\alpha_{\text{Superlattice}}$ is 0.094, that is, smaller than the expected ratio of 0.097 between the α_{Gr} and the moiré lattice constant $\alpha_{\text{moiré}}$ before cluster deposition. Although the origin of this strain effect is not settled, we speculate that it might result from a graphene expansion underneath the clusters (invisible to HRTEM) and a Gr compression in between, as found in density functional theory calculations,⁴² which could be frozen due to embedding.

Magnified HRTEM images such as the one given in Figure 3e show that the metal clusters are crystalline as obvious from their lattice fringes. Often the fringes resemble the (111) lattice plane of Ir. A zoom-in on an Ir cluster reveals a clear hexagonal structure. The in-plane nearest neighbor distance measured from the line profile of Figure 3 is 2.65 ± 0.05 Å, which is slightly smaller than the Ir bulk value of 2.715 Å.^{20,26} The reduced in-plane cluster nearest neighbor distance compares well with the results of surface X-ray diffraction experiments for similar-sized nonembedded Ir clusters on Gr/Ir(111), where a compressive in-plane strain of 2.5% was measured.²⁰

Because the metal clusters grow epitaxially on Gr prior to embedding and lift-off, their (111) lattice plane is parallel to

the surface and their dense packed atomic rows are parallel to the dense packed rows of the cluster superlattice.²⁶ To uncover whether changes in the cluster orientation and structure take place during embedding and lift-off, we looked at each cluster of Figure 3e individually, marked the directions of their fringes, and compared them with the superlattice directions as shown in Figure S4. About 54% of the clusters' fringes are aligned along the high symmetry lines of the superlattice (marked with red in the inset of Figure 3e) and thus with those of Gr, whereas 24% are now misoriented. Thus, the rest of the clusters do not exhibit any clear structure (19%) or are missing (3%). The induced misorientation of the clusters presumably has taken place during embedding or could be caused by the observed reorganization of the C bonds during annealing to 850 K.

On the basis of the experiments reported here, CSLMs are a robust, flexible, inert, and stable hybrid 2D material. What we show is only the first example of this type of material. While we used Gr/Ir(111) as our prototypical template, the fabrication procedure can be expanded to different cluster template substrates such as Gr or h-BN moiré on Ir(111), Ru(0001), and Rh(111) and thin alumina films.^{24,43–50} Because of this, the fabrication process can include a wide range of cluster materials (alkali metals, transition metals, rare earths, semiconductors)^{26,35,51–53} with different physicochemical properties. In fact, we also were able to form CSLMs with Pt clusters and also with h-BN as the 2D layer. We speculate that the embedding matrix can be formed by a variety of materials of which insulating oxides (e.g., Al₂O₃) would be attractive in view of potential applications in nanocatalysis or nano-optics.

Potential Applications. The properties of the CSLM, being a 2D lattice of small equally sized clusters and itself being mechanically and thermally stable due to its embedding matrix, provide an application potential that still needs to be realized through further steps in material processing and by integration of the CSLM into devices. We argue that CSLMs can be potentially useful in single electron transistors (SETs), phase formation, and application as electrocatalytic electrodes.

SETs use the gate controllable Coulomb blockade of quantum dots to control electrical transport.^{54,55} A cluster superlattice with a narrow size cluster distribution enables the use of a group of clusters for the switching through Coulomb blockade, thereby making the process more robust and simplifying contacting compared to a single cluster device. Moreover, it could also be the basis for fabrication of an entire array of SETs, all with the same Coulomb blockade characteristics. Lastly, a superlattice of metallic clusters is also a playground for the investigation of hopping transport and charge localization, as, for example, demonstrated by Whitham et al.⁵⁶ As detailed in the Supporting Information (compare Figure S5 and corresponding explanations), Pt-CSLMs using h-BN as the 2D layer display discrete energy levels in a tunneling experiment as a result of Coulomb blockade. These energy levels could be effectively used as on and off states through the use of a gate electrode in a SET.

Moreover, the stability of the CSLM under high temperatures could allow the synthesis of phases that require high-temperature processing, for example, the high magnetic anisotropy L1₀ phase of FePt,^{57–59} without losing the regular cluster arrangement. The protection of the clusters from oxidation would also enable the study of magnetic materials in a 2D lattice, for example, an analysis of dipolar interactions of small superparamagnetic clusters in close spacing.⁶⁰

Lastly, postprocessing by etching of the 2D layer and uncovering the cluster metal surface will make the membrane active for catalytic applications and enable the development of efficient catalysts of high selectivity.^{47,61–65} Of specific interest is the exploration of few or single atom cluster superlattices for use in single atom catalysis.^{61,62}

CONCLUSIONS

In conclusion, we have fabricated the first free-standing cluster superlattice membrane. The cluster superlattice is self-organized on the Gr moiré on Ir(111) and encapsulated within an inert and stable nanometer-thick amorphous C film. A prerequisite for lift-off from the Ir(111) is weakening of the membrane binding to the substrate by annealing. Annealing causes internal matrix reorganization and enables subsequent intercalation which further weakens binding. After the removal of the membrane from the Ir(111) substrate with electrochemical methods, HRTEM measurements confirmed the presence of a highly regular cluster superlattice with intercluster distance of ~ 2.5 nm. The Gr lattice is preserved throughout the membrane, confirmed by diffraction spots. In the example presented here, the cluster average diameter is 1.2 ± 0.2 nm, consistent with bilayer Ir clusters of 35 atoms. The cluster size and composition, as well as the membrane thickness and shape, can be controlled during the bottom-up fabrication procedure. The use of different 2D layer templates, cluster materials, and sizes, as well as embedding materials, make cluster superlattice membranes a diverse material with a wide range of physicochemical properties.

EXPERIMENTAL METHODS

The sample preparation, STM imaging, and LEED were done in an ultrahigh vacuum system in Cologne with a base pressure in the 10^{-11} mbar regime. The Ir(111) crystal was cleaned using several cycles of 2 keV Xe⁺ sputtering and flash annealing to 1550 K. The Gr monolayer was grown on Ir(111) by a two-step process: adsorption of ethylene until saturation at room temperature and subsequent thermal decomposition at 1300 K, and 300 s ethylene exposure at 1300 K in ethylene pressure of 1×10^{-7} mbar. The resulting Gr coverage was close to 100%, as checked with LEED and STM.

Ir and C were evaporated on Gr/Ir(111) at room temperature from an e-beam evaporator using high purity rods with a deposition rate of $\sim 10^{-2}$ ML/s at an evaporation pressure below 5×10^{-10} mbar. The deposited amount θ was calibrated by deposition of C and Ir on the clean Ir(111) surface and subsequent annealing to 1470 K for C and 800 K for Ir. The heating step leads to the formation of compact monolayer islands of Gr or Ir islands, respectively. STM imaging was used for the determination of the island coverage and thus the deposition flux. The deposited amount of C is given in monolayers with respect to the atomic density in Gr, while the deposited amount of Ir is specified in monolayers with respect to the surface atomic density of Ir(111).

STM imaging was done at room temperature, using tunneling currents I in the range from $I = 0.1$ – 0.6 nA and sample bias voltages U_s in the range $U_s = -(0.8$ – $2.0)$ V. The average cluster size of 35 atoms for 0.4 ML of Ir was obtained using the equation $s_{av} = A_m \theta / n$, where n is the cluster number density equal to 1, θ is the metal coverage, and A_m is the area of the moiré cell equal to $A_m = 87$ Ir substrate unit cells.²³ The STM data were processed (background subtraction and contrast adjustment) using the WSxM software.⁶⁶

Optical microscopy imaging was done with a Keyence VHX-6000 in Cologne. The Raman spectra were acquired in the backscattering geometry using a 532 nm laser and the Renishaw inVia confocal Raman microscope with a 100 \times objective (NA = 0.85). The integration time per spectrum was 60 s, and the laser power was 0.1 mW. During the measurements, no change in Raman spectra was

observed ruling out sample degradation. From the fit of the single Raman peaks with Lorentzian functions, we obtained full width at half-maximum of ~ 10 cm⁻¹ for G, D, and D' modes for both suspended graphene and graphene in the CSLM.

The HRTEM imaging, EDX, and selected area electron diffraction (SAED) images were acquired using FEI TITAN 80–300 equipped with image side aberration corrector for the objective lens in Vienna. The microscope was operated at 80 kV accelerating voltage to reduce the potential knock-on damage at the sample. HRTEM images were acquired in negative Cs (~ 10 μ m) imaging condition, providing strong local contrast at the atomic site. For electron diffraction patterns, two different camera lengths were used, a smaller length of 240 mm for graphene spots and a relatively larger length of about 1.7 m for the spots of the superlattice which appear quite close to the direct spot because of the larger lattice periodicity.

The UHV X-ray high resolution photoemission spectroscopy experiments were conducted at the SuperESCA beamline of the synchrotron radiation source Elettra (Trieste, Italy). The Ir(111) crystal was spot-welded on a Ta wire and mounted on a manipulator with a W filament placed behind the sample. The samples were prepared *in situ* using similar procedures as described in the STM section with the same evaporators and very similar rates in a background pressure below 10^{-10} mbar. The quality of the Gr/Ir(111) was checked by LEED and by verifying the absence of C and O contaminants in the XP spectra after cluster growth. The XP spectra were acquired at variable temperatures in normal emission. The Ir 4f_{7/2} and C 1s core level spectra were measured in normal incidence using photon energies of 140 and 390 eV, respectively, with overall energy resolution (photon beam and electron energy analyzer) better than 50 meV. For the fitting of Ir 4f_{7/2}, we subtracted a Shirley-type background and corrected to the Fermi edge. The Ir 4f_{7/2} spectra components were then fitted with an asymmetric Doniach-Sunjić function convoluted with a Gaussian as is typical for transition metal core levels.

ASSOCIATED CONTENT

Supporting Information

The Supporting Information is available free of charge at <https://pubs.acs.org/doi/10.1021/acsnano.0c05740>.

Figure S1 shows the LEED images of the Gr/Ir(111) and the CSLM on Ir(111), Figure S2 shows a 3D rendered image of the shadow mask, Figure S3 shows the diffraction images of the cluster superlattice and graphene lattice, Figure S4 shows a zoom-in HRTEM image of the cluster symmetry, Figure S5 shows Coulomb blockade measured in CSLM and the corresponding description (PDF)

AUTHOR INFORMATION

Corresponding Author

Pantelis Bampoulis – II. Physikalisches Institut, Universität zu Köln, Cologne D-50937, Germany; orcid.org/0000-0002-2347-5223; Email: bampoulis@ph2.uni-koeln.de

Authors

Tobias Hartl – II. Physikalisches Institut, Universität zu Köln, Cologne D-50937, Germany

Moritz Will – II. Physikalisches Institut, Universität zu Köln, Cologne D-50937, Germany; orcid.org/0000-0003-4822-9122

Davor Čapeta – Institute of Physics, 10000 Zagreb, Croatia

Rajendra Singh – Faculty of Physics, Vienna University, 1090 Vienna, Austria

Daniel Scheinecker – Faculty of Physics, Vienna University, 1090 Vienna, Austria

Virginia Boix de la Cruz – MAX IV Laboratory and Division of Synchrotron Radiation Research, Lund University, 22100 Lund, Sweden; orcid.org/0000-0002-1152-8201

Sophia Dellmann – II. Physikalisches Institut, Universität zu Köln, Cologne D-50937, Germany

Paolo Lacovig – Elettra-Sincrotrone Trieste S.C.p.A., I-34149 Trieste, Italy; orcid.org/0000-0001-7001-7930

Silvano Lizzit – Elettra-Sincrotrone Trieste S.C.p.A., I-34149 Trieste, Italy; orcid.org/0000-0003-1620-7228

Boris V. Senkovskiy – II. Physikalisches Institut, Universität zu Köln, Cologne D-50937, Germany; orcid.org/0000-0003-1443-6780

Alexander Grüneis – II. Physikalisches Institut, Universität zu Köln, Cologne D-50937, Germany; orcid.org/0000-0003-2448-6060

Marko Kralj – Institute of Physics, 10000 Zagreb, Croatia; orcid.org/0000-0002-9786-3130

Jan Knudsen – MAX IV Laboratory and Division of Synchrotron Radiation Research, Lund University, 22100 Lund, Sweden

Jani Kotakoski – Faculty of Physics, Vienna University, 1090 Vienna, Austria; orcid.org/0000-0002-1301-5266

Thomas Michely – II. Physikalisches Institut, Universität zu Köln, Cologne D-50937, Germany

Complete contact information is available at:
<https://pubs.acs.org/10.1021/acsnano.0c05740>

Notes

The authors declare no competing financial interest.

ACKNOWLEDGMENTS

P.B. gratefully acknowledges financial support from the Alexander von Humboldt foundation. D.C. and M. K. acknowledge support from the European Regional Development Fund for the “Center of Excellence for Advanced Materials and Sensing Devices” (No. KK.01.1.1.01.0001). V.B. and J. K. acknowledge financial support from the Swedish Research Council Grant 2017-04840 and the Craaford foundation. B.S. and A.G. acknowledge the ERC-Grant 648589 “SUPER-2D”.

REFERENCES

- (1) Das, S.; Robinson, J. A.; Dubey, M.; Terrones, H.; Terrones, M. Beyond Graphene: Progress in Novel Two-Dimensional Materials and van der Waals Solids. *Annu. Rev. Mater. Res.* **2015**, *45*, 1–27.
- (2) Akinwande, D.; Huyghebaert, C.; Wang, C.-H.; Serna, M. I.; Goossens, S.; Li, L.-J.; Wong, H.-S. P.; Koppens, F. H. Graphene and Two-Dimensional Materials for Silicon Technology. *Nature* **2019**, *573*, 507–518.
- (3) Novoselov, K. S.; Geim, A. K.; Morozov, S. V.; Jiang, D.; Zhang, Y.; Dubonos, S. V.; Grigorieva, I. V.; Firsov, A. A. Electric Field Effect in Atomically Thin Carbon Films. *Science* **2004**, *306*, 666–669.
- (4) Booth, T. J.; Blake, P.; Nair, R. R.; Jiang, D.; Hill, E. W.; Bangert, U.; Bleloch, A.; Gass, M.; Novoselov, K. S.; Katsnelson, M. I.; Geim, A. K. Macroscopic Graphene Membranes and Their Extraordinary Stiffness. *Nano Lett.* **2008**, *8*, 2442–2446.
- (5) Castro Neto, A. H.; Guinea, F.; Peres, N. M. R.; Novoselov, K. S.; Geim, A. K. The Electronic Properties of Graphene. *Rev. Mod. Phys.* **2009**, *81*, 109.
- (6) Zhang, Y.; Tang, Z.-R.; Fu, X.; Xu, Y.-J. TiO₂-Graphene Nanocomposites for Gas-Phase Photocatalytic Degradation of Volatile Aromatic Pollutant: Is TiO₂-Graphene Truly Different from Other TiO₂-Carbon Composite Materials? *ACS Nano* **2010**, *4*, 7303–7314.

(7) Kamat, P. V. Graphene-Based Nanoarchitectures. Anchoring Semiconductor and Metal Nanoparticles on a Two-Dimensional Carbon Support. *J. Phys. Chem. Lett.* **2010**, *1*, 520–527.

(8) Liu, J.; Ma, Q.; Huang, Z.; Liu, G.; Zhang, H. Recent Progress in Graphene-Based Noble-Metal Nanocomposites for Electrocatalytic Applications. *Adv. Mater.* **2019**, *31*, 1800696.

(9) Eck, W.; Küller, A.; Grunze, M.; Völkel, B.; Götzhäuser, A. Freestanding Nanosheets from Crosslinked Biphenyl Self-Assembled Monolayers. *Adv. Mater.* **2005**, *17*, 2583–2587.

(10) Turchanin, A.; Götzhäuser, A. Carbon Nanomembranes from Self-Assembled Monolayers: Functional Surfaces Without Bulk. *Prog. Surf. Sci.* **2012**, *87*, 108–162.

(11) Angelova, P.; Vieker, H.; Weber, N.-E.; Matei, D.; Reimer, O.; Meier, I.; Kurasch, S.; Biskupek, J.; Lorbach, D.; Wunderlich, K.; Chen, L.; Terfort, A.; Klapper, M.; Müllen, K.; Kaiser, U.; Götzhäuser, A.; Turchanin, A. A Universal Scheme to Convert Aromatic Molecular Monolayers into Functional Carbon Nanomembranes. *ACS Nano* **2013**, *7*, 6489–6497.

(12) Ai, M.; Shishatskiy, S.; Wind, J.; Zhang, X.; Nottbohm, C. T.; Mellech, N.; Winter, A.; Vieker, H.; Qiu, J.; Dietz, K.-J.; Götzhäuser, A.; Beyer, A. Carbon Nanomembranes (CNMs) Supported by Polymer: Mechanics and Gas Permeation. *Adv. Mater.* **2014**, *26*, 3421–3426.

(13) Turchanin, A.; Götzhäuser, A. Carbon Nanomembranes. *Adv. Mater.* **2016**, *28*, 6075–6103.

(14) Yang, Y.; Hillmann, R.; Qi, Y.; Korzetz, R.; Biere, N.; Emmrich, D.; Westphal, M.; Büker, B.; Hütten, A.; Beyer, A.; Anselmetti, D.; Götzhäuser, A. Ultrahigh Ionic Exclusion through Carbon Nanomembranes. *Adv. Mater.* **2020**, *32*, 1907850.

(15) Lightcap, I. V.; Kosel, T. H.; Kamat, P. V. Anchoring Semiconductor and Metal Nanoparticles on a Two-Dimensional Catalyst Mat. Storing and Shuttling Electrons with Reduced Graphene Oxide. *Nano Lett.* **2010**, *10*, 577–583.

(16) Shang, L.; Bian, T.; Zhang, B.; Zhang, D.; Wu, L.-Z.; Tung, C.-H.; Yin, Y.; Zhang, T. Graphene-Supported Ultrafine Metal Nanoparticles Encapsulated by Mesoporous Silica: Robust Catalysts for Oxidation and Reduction Reactions. *Angew. Chem., Int. Ed.* **2014**, *53*, 250–254.

(17) Sarkar, C.; Pendem, S.; Shrotri, A.; Dao, D. Q.; Pham Thi Mai, P.; Nguyen Ngoc, T.; Chandaka, D. R.; Rao, T. V.; Trinh, Q. T.; Sherburne, M. P.; Mondal, J. Interface Engineering of Graphene-Supported Cu Nanoparticles Encapsulated by Mesoporous Silica for Size-Dependent Catalytic Oxidative Coupling of Aromatic Amines. *ACS Appl. Mater. Interfaces* **2019**, *11*, 11722–11735.

(18) Rao, S.; Si, K. J.; Yap, L. W.; Xiang, Y.; Cheng, W. Free-Standing Bilayered Nanoparticle Superlattice Nanosheets with Asymmetric Ionic Transport Behaviors. *ACS Nano* **2015**, *9*, 11218–11224.

(19) Shi, Q.; Gómez, D. E.; Dong, D.; Sikdar, D.; Fu, R.; Liu, Y.; Zhao, Y.; Smilgies, D.-M.; Cheng, W. 2D Freestanding Janus Gold Nanocrystal Superlattices. *Adv. Mater.* **2019**, *31*, 1900989.

(20) Franz, D.; Runte, S.; Busse, C.; Schumacher, S.; Gerber, T.; Michely, T.; Mantilla, M.; Kilic, V.; Zegenhagen, J.; Stierle, A. Atomic Structure and Crystalline Order of Graphene-Supported Ir Nanoparticle Lattices. *Phys. Rev. Lett.* **2013**, *110*, No. 065503.

(21) Billinge, S. Materials Science: Nanoparticle Structures Served up on a Tray. *Nature* **2013**, *495*, 453–454.

(22) Meiwees-Broer, K.-H. *Metal Clusters at Surfaces: Structure, Quantum Properties, Physical Chemistry*; Springer Science & Business Media: Heidelberg, 2000.

(23) N'Diaye, A. T.; Bleikamp, S.; Feibelman, P. J.; Michely, T. Two-Dimensional Ir Cluster Lattice on a Graphene Moiré on Ir(111). *Phys. Rev. Lett.* **2006**, *97*, 215501.

(24) Will, M.; Atodiresei, N.; Caciuc, V.; Valerius, P.; Herbig, C.; Michely, T. A Monolayer of Hexagonal Boron Nitride on Ir(111) as a Template for Cluster Superlattices. *ACS Nano* **2018**, *12*, 6871–6880.

(25) Coraux, J.; N'Diaye, A. T.; Busse, C.; Michely, T. Structural Coherency of Graphene on Ir (111). *Nano Lett.* **2008**, *8*, 565–570.

- (26) N'Diaye, A. T.; Gerber, T.; Busse, C.; Myslivecek, J.; Coraux, J.; Michely, T. A Versatile Fabrication Method for Cluster Superlattices. *New J. Phys.* **2009**, *11*, 103045.
- (27) Knudsen, J.; Feibelman, P. J.; Gerber, T.; Grå näs, E.; Schulte, K.; Stratmann, P.; Andersen, J. N.; Michely, T. Clusters Binding to the Graphene Moiré on Ir (111): X-Ray Photoemission Compared to Density Functional Calculations. *Phys. Rev. B: Condens. Matter Mater. Phys.* **2012**, *85*, No. 035407.
- (28) Will, M.; Bampoulis, P.; Hartl, T.; Valerius, P.; Michely, T. Conformal Embedding of Cluster Superlattices with Carbon. *ACS Appl. Mater. Interfaces* **2019**, *11*, 40524–40532.
- (29) Schumacher, S.; Wehling, T. O.; Lazić, P.; Runte, S.; Förster, D. F.; Busse, C.; Petrović, M.; Kralj, M.; Blügel, S.; Atodiresei, N.; Caciuc, V.; Michely, T. The Backside of Graphene: Manipulating Adsorption by Intercalation. *Nano Lett.* **2013**, *13*, S013–S019.
- (30) Petrović, M.; Rakić, I. Š.; Runte, S.; Busse, C.; Sadowski, J.; Lazić, P.; Pletikosić, I.; Pan, Z.-H.; Milun, M.; Pervan, P.; Atodiresei, N.; Brako, R.; Šokčević, D.; Valla, T.; T. M.; Kralj, M. The Mechanism of Caesium Intercalation of Graphene. *Nat. Commun.* **2013**, *4*, 1–8.
- (31) Gao, L.; Ren, W.; Xu, H.; Jin, L.; Wang, Z.; Ma, T.; Ma, L.-P.; Zhang, Z.; Fu, Q.; Peng, L.-M.; Bao, X.; Chengothers, H.-M. Repeated Growth and Bubbling Transfer of Graphene with Millimetre-Size Single-Crystal Grains Using Platinum. *Nat. Commun.* **2012**, *3*, 699.
- (32) Rakić, I. Š.; Čapeta, D.; Plodinec, M.; Kralj, M. Large-Scale Transfer and Characterization of Macroscopic Periodically Nano-Rippled Graphene. *Carbon* **2016**, *96*, 243–249.
- (33) Koren, E.; Sutter, E.; Bliznakov, S.; Ivars-Barcelo, F.; Sutter, P. Isolation of High Quality Graphene from Ru by Solution Phase Intercalation. *Appl. Phys. Lett.* **2013**, *103*, 121602.
- (34) Cherian, C. T.; Giustiniano, F.; Martin-Fernandez, I.; Andersen, H.; Balakrishnan, J.; Özyilmaz, B. Bubble-Free Electrochemical Delamination of CVD Graphene Films. *Small* **2015**, *11*, 189–194.
- (35) Herbig, C.; Knispel, T.; Simon, S.; Schröder, U. A.; Martínez-Galera, A. J.; Arman, M. A.; Teichert, C.; Knudsen, J.; Krashennikov, A. V.; Michely, T. From Permeation to Cluster Arrays: Graphene on Ir(111) Exposed to Carbon Vapor. *Nano Lett.* **2017**, *17*, 3105–3112.
- (36) Ferrari, A. C.; Basko, D. M. Raman Spectroscopy as a Versatile Tool for Studying the Properties of Graphene. *Nat. Nanotechnol.* **2013**, *8*, 235.
- (37) Heller, E. J.; Yang, Y.; Kocia, L.; Chen, W.; Fang, S.; Borunda, M.; Kaxiras, E. Theory of Graphene Raman Scattering. *ACS Nano* **2016**, *10*, 2803–2818.
- (38) Scheibe, H.-J.; Drescher, D.; Alers, P. Raman Characterization of Amorphous Carbon Films. *Fresenius' J. Anal. Chem.* **1995**, *353*, 695–697.
- (39) Lacovig, P.; Pozzo, M.; Alfe, D.; Vilmercati, P.; Baraldi, A.; Lizzit, S. Growth of Dome-Shaped Carbon Nanoislands on Ir (111): The Intermediate between Carbide Clusters and Quasi-Free-Standing Graphene. *Phys. Rev. Lett.* **2009**, *103*, 166101.
- (40) Gerber, T.; Grå näs, E.; Schröder, U. A.; Stratmann, P.; Schulte, K.; Andersen, J. N.; Knudsen, J.; Michely, T. Stability and Reactivity of Graphene-Templated Nanoclusters. *J. Phys. Chem. C* **2016**, *120*, 26290–26299.
- (41) Presel, F.; Tache, C. A.; Tetlow, H.; Curcio, D.; Lacovig, P.; Kantorovich, L.; Lizzit, S.; Baraldi, A. Spectroscopic Fingerprints of Carbon Monomers and Dimers on Ir (111): Experiment and Theory. *J. Phys. Chem. C* **2017**, *121*, 11335–11345.
- (42) Feibelman, P. J. Pinning of Graphene to Ir (111) by Flat Ir Dots. *Phys. Rev. B: Condens. Matter Mater. Phys.* **2008**, *77*, 165419.
- (43) Degen, S.; Becker, C.; Wandelt, K. Thin Alumina Films on Ni₃Al(111): A Template for Nanostructured Pd Cluster Growth. *Faraday Discuss.* **2004**, *125*, 343–356.
- (44) Schmid, M.; Kresse, G.; Buchsbaum, A.; Napetschnig, E.; Gritschneider, S.; Reichling, M.; Varga, P. Nanotemplate with Holes: Ultrathin Alumina on Ni₃Al (111). *Phys. Rev. Lett.* **2007**, *99*, 196104.
- (45) Sutter, E.; Albrecht, P.; Wang, B.; Bocquet, M.-L.; Wu, L.; Zhu, Y.; Sutter, P. Arrays of Ru Nanoclusters with Narrow Size Distribution Templated by Monolayer Graphene on Ru. *Surf. Sci.* **2011**, *605*, 1676–1684.
- (46) Sitja, G.; Moal, S. L.; Marsault, M.; Hamm, G.; Leroy, F.; Henry, C. R. Transition from Molecule to Solid State: Reactivity of Supported Metal Clusters. *Nano Lett.* **2013**, *13*, 1977–1982.
- (47) Henry, C. R. 2D-Arrays of Nanoparticles as Model Catalysts. *Catal. Lett.* **2015**, *145*, 731–749.
- (48) Sitja, G.; Henry, C. R. Molecular Beam Study of the Oxidation of Carbon Monoxide on a Regular Array of Palladium Clusters on Alumina. *J. Phys. Chem. C* **2017**, *121*, 10706–10712.
- (49) Düll, F.; Bauer, U.; Späth, F.; Bachmann, P.; Steinhauer, J.; Steinrück, H.-P.; Papp, C. Bimetallic Pd–Pt Alloy Nanocluster Arrays on Graphene/Rh (111): Formation, Stability, and Dynamics. *Phys. Chem. Chem. Phys.* **2018**, *20*, 21294–21301.
- (50) Martínez-Galera, A. J.; Gómez-Rodríguez, J. M. Pseudo-Ordered Distribution of Ir Nanocrystals on h-BN. *Nanoscale* **2019**, *11*, 2317–2325.
- (51) Baltic, R.; Pivetta, M.; Donati, F.; Wäckerlin, C.; Singha, A.; Dreiser, J.; Rusponi, S.; Brune, H. Superlattice of Single Atom Magnets on Graphene. *Nano Lett.* **2016**, *16*, 7610–7615.
- (52) Mousadakis, D.; Pivetta, M.; Brune, H.; Rusponi, S. Sm Cluster Superlattice on Graphene/Ir (111). *New J. Phys.* **2017**, *19*, 123021.
- (53) Petrović, M.; Lazić, P.; Runte, S.; Michely, T.; Busse, C.; Kralj, M. Moiré-Regulated Self-Assembly of Cesium Adatoms on Epitaxial Graphene. *Phys. Rev. B: Condens. Matter Mater. Phys.* **2017**, *96*, No. 085428.
- (54) Willing, S.; Lehmann, H.; Volkmann, M.; Klinke, C. Metal Nanoparticle Film–Based Room Temperature Coulomb Transistor. *Sci. Adv.* **2017**, *3*, No. e1603191.
- (55) Godel, F.; Mouafo, L. D. N.; Froehlicher, G.; Doudin, B.; Berciaud, S.; Henry, Y.; Dayen, J.-F.; Halley, D. Conductance Oscillations in a Graphene/Nanocluster Hybrid Material: Toward Large-Area Single-Electron Devices. *Adv. Mater.* **2017**, *29*, 1604837.
- (56) Whitham, K.; Yang, J.; Savitzky, B. H.; Kourkoutis, L. F.; Wise, F.; Hanrath, T. Charge Transport and Localization in Atomically Coherent Quantum Dot Solids. *Nat. Mater.* **2016**, *15*, 557–563.
- (57) Sun, S.; Murray, C. B.; Weller, D.; Folks, L.; Moser, A. Monodisperse FePt Nanoparticles and Ferromagnetic FePt Nanocrystal Superlattices. *Science* **2000**, *287*, 1989–1992.
- (58) Weller, D.; Parker, G.; Mosendz, O.; Lyberatos, A.; Mitin, D.; Safonova, N. Y.; Albrecht, M. FePt Heat Assisted Magnetic Recording Media. *J. Vac. Sci. Technol., B: Nanotechnol. Microelectron.: Mater., Process., Meas., Phenom.* **2016**, *34*, No. 060801.
- (59) Capiod, P.; Bardotti, L.; Tamion, A.; Boisson, O.; Albin, C.; Dupuis, V.; Renaud, G.; Ohresser, P.; Tournus, F. Elaboration of Nanomagnet Arrays: Organization and Magnetic Properties of Mass-Selected FePt Nanoparticles Deposited on Epitaxially Grown Graphene on Ir (111). *Phys. Rev. Lett.* **2019**, *122*, 106802.
- (60) Fabris, F.; Tu, K.-H.; Ross, C.; Nunes, W. Influence of Dipolar Interactions on the Magnetic Properties of Superparamagnetic Particle Systems. *J. Appl. Phys.* **2019**, *126*, 173905.
- (61) Cheng, N.; Stambula, S.; Wang, D.; Banis, M. N.; Liu, J.; Riese, A.; Xiao, B.; Li, R.; Sham, T.-K.; Liu, L.-M.; Botton, G. A.; Sun, X. Platinum Single-Atom and Cluster Catalysis of the Hydrogen Evolution Reaction. *Nat. Commun.* **2016**, *7*, 1–9.
- (62) Liu, L.; Corma, A. Metal Catalysts for Heterogeneous Catalysis: From Single Atoms to Nanoclusters and Nanoparticles. *Chem. Rev.* **2018**, *118*, 4981–5079.
- (63) Bartholomew, C. H. Mechanisms of Catalyst Deactivation. *Appl. Catal., A* **2001**, *212*, 17–60.
- (64) Gerber, T.; Knudsen, J.; Feibelman, P. J.; Granas, E.; Stratmann, P.; Schulte, K.; Andersen, J. N.; Michely, T. CO-Induced Smoluchowski Ripening of Pt Cluster Arrays on the Graphene/Ir(111) Moiré. *ACS Nano* **2013**, *7*, 2020–2031.
- (65) Lu, J.; Fu, B.; Kung, M. C.; Xiao, G.; Elam, J. W.; Kung, H. H.; Stair, P. C. Coking-and Sintering-Resistant Palladium Catalysts Achieved through Atomic Layer Deposition. *Science* **2012**, *335*, 1205–1208.

(66) Horcas, I.; Fernández, R.; Gomez-Rodriguez, J.; Colchero, J.; Gómez-Herrero, J.; Baro, A. WSXm: A Software for Scanning Probe Microscopy and a Tool for Nanotechnology. *Rev. Sci. Instrum.* **2007**, 78, No. 013705.

Supporting Information:

Cluster Superlattice Membranes

Tobias Hartl,[†] Moritz Will,[†] Davor Čapeta,[‡] Rajendra Singh,[¶] Daniel Scheinecker,[¶] Virginia Boix de la Cruz,[§] Sophia Dellmann,[†] Paolo Lacovig,^{||} Silvano Lizzit,^{||} Boris V. Senkovskiy,[†] Alexander Grüneis,[†] Marko Kralj,[‡] Jan Knudsen,[§] Jani Kotakoski,[¶] Thomas Michely,[†] and Pantelis Bampoulis*,[†]

[†]*II. Physikalisches Institut, Universität zu Köln, Cologne, D-50937, Germany*

[‡]*Institute of Physics, Bijenička cesta 46, 10000, Zagreb, Croatia*

[¶]*Faculty of Physics, Vienna University, Boltzmanngasse 5, 1090, Vienna, Austria*

[§]*MAX IV Laboratory and Division of Synchrotron Radiation Research, Lund University, Box 118, 22100 Lund, Sweden*

^{||}*Elettra-Sincrotrone Trieste S.C.p.A., Strada Statale 14 Km 163.5, I-34149 Trieste, Italy*

E-mail: bampoulis@ph2.uni-koeln.de

Diffraction

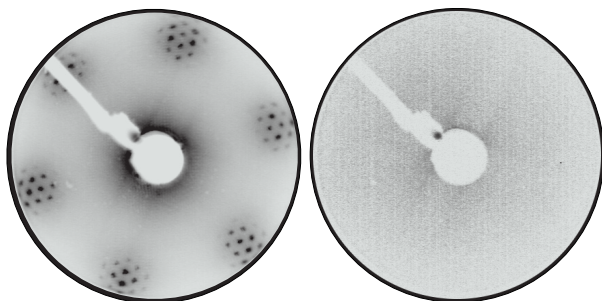


Figure S1: LEED patterns acquired at 72 eV of the Gr/Ir(111) (left) and the CSLM (right) covering the whole (6 mm) Ir(111) crystal.

Shadow mask

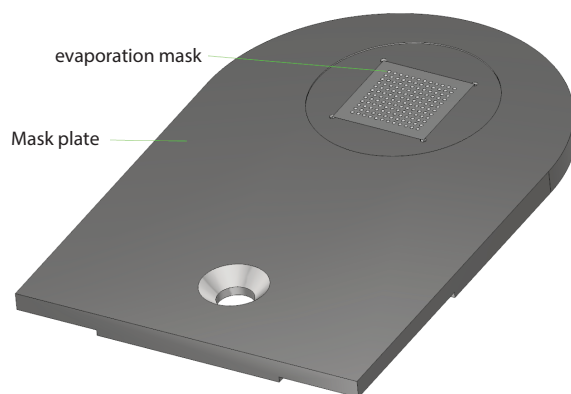


Figure S2: 3D rendered image of the mask plate with the evaporation mask, consisting of 48 holes of $300\text{ }\mu\text{m}$ diameter.

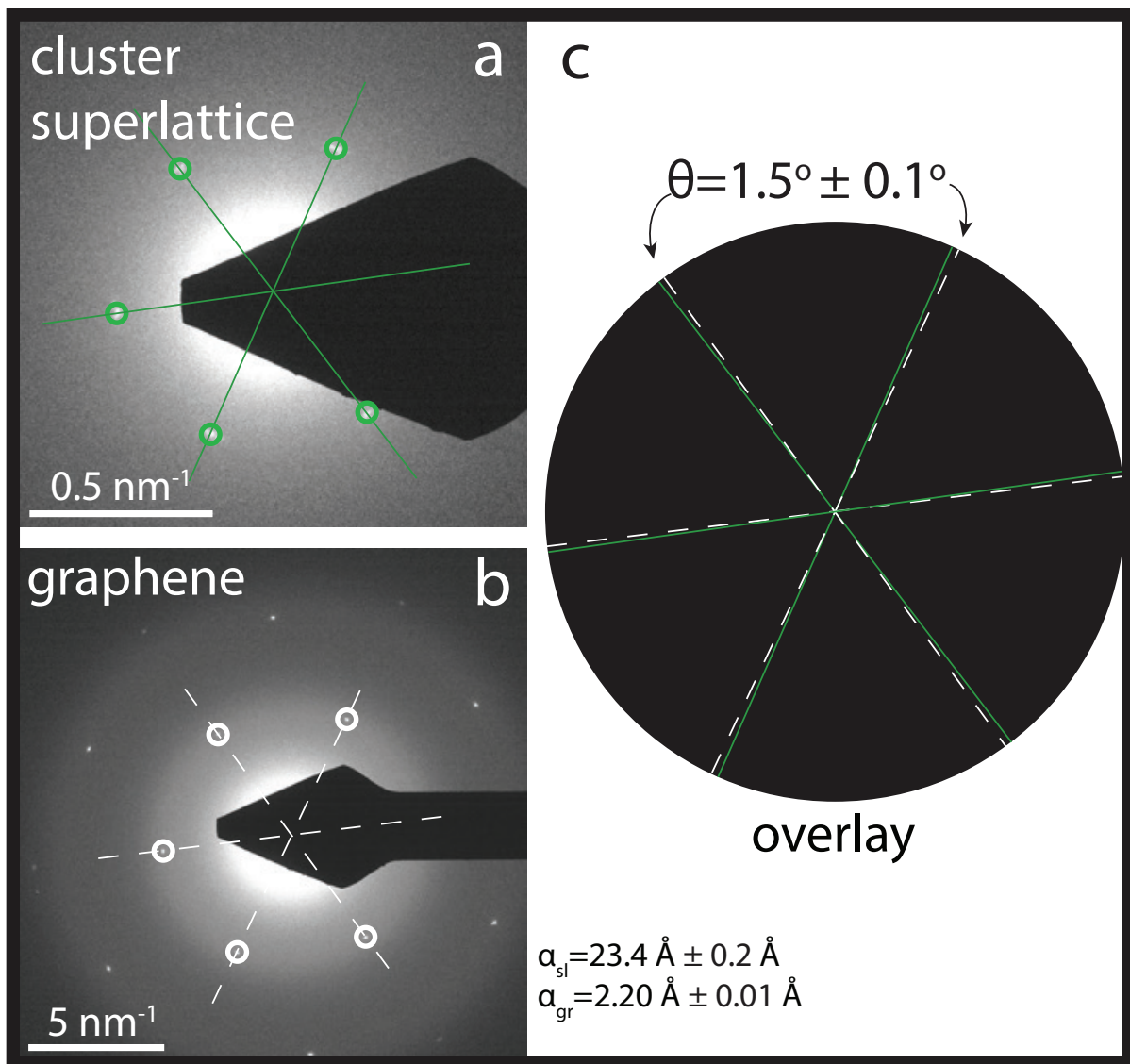


Figure S3: Diffraction patterns of the cluster superlattice (a) and graphene (b) acquired on the membrane. Overlaying of the directions of the two diffraction patterns showing a misalignment of 1.5° .

Cluster symmetry

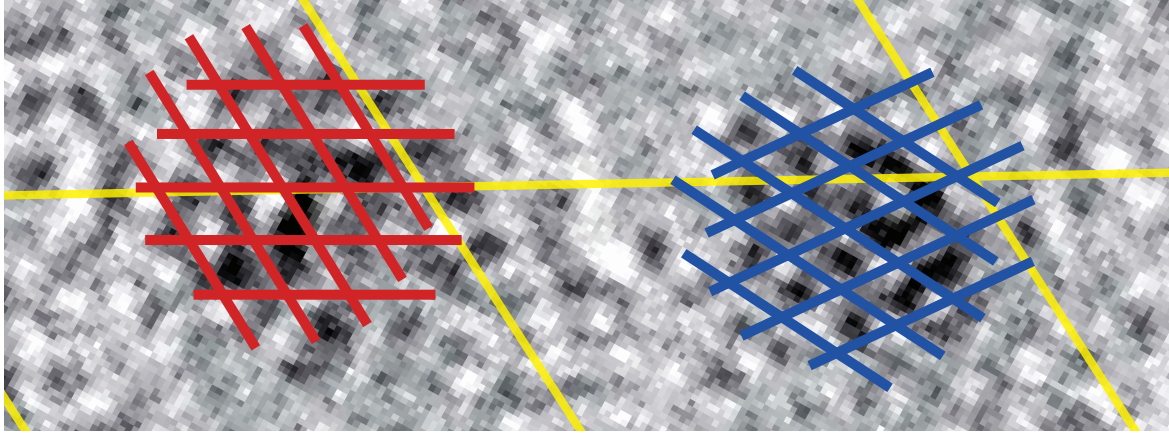


Figure S4: A zoom-in TEM image of two Ir clusters in the membrane. The directions of the fringes observed in the clusters are marked and compared with the high symmetry directions of the superlattice, red indicates cluster epitaxy with the superlattice and blue randomly oriented clusters.

Coulomb blockade

To demonstrate the functionality of the CSLM, we have designed a CSLM in which Pt_{55} clusters are encapsulated within insulating h-BN and semiconducting a-C (1.6 ML). When contacting with STM, the system is effectively a double barrier tunnel junction, in which the two tunnel junctions are the Ir/h-BN/clusters and clusters/(a-C/tunnel barrier)/tip, see the schematic in Figure S5a. Room temperature I-V spectra acquired through this set-up, reflect Coulomb blockade and Coulomb oscillations phenomena, characteristic of a single electron tunneling. An example is shown in Figure S5a, the I-V spectrum displays sharp step-like changes with a period of 0.35 V, a Coulomb staircase. As a consequence, the differential conductance of the CSLM, Figure S5b, has discrete electronic energy levels with the same period. These distinct energy levels resulted from Coulomb oscillations could be effectively used as on and off states through the use of a gate electrode, in a single-electron transistor (contrary to the semiconducting gap used in field-effect transistors, a SET relies on the Coulomb energy gap). The use of a superlattice of clusters over single nanoparticles simplifies the fabrication process and reduces the involved costs (compared to contacting a

single cluster device), making a SET device industrially feasible.

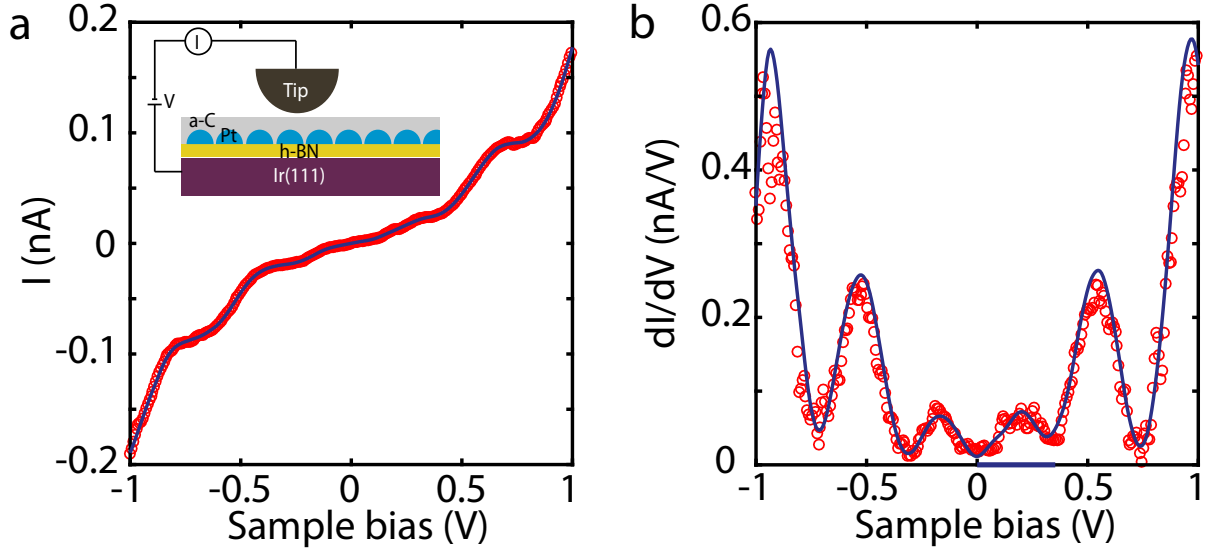


Figure S5: a) I-V characteristic recorded with an STM tip at room temperature on a CSLM consisting of 1.6 ML a-C/Pt clusters/ h-BN on Ir(111). The system forms a double barrier junction resulting in a Coulomb staircase. Inset: The experimental set-up, showing the two tunnel barriers; clusters/h-BN/Ir and clusters/(a-C/tunneling barrier)/tip. b) The differential conductance obtained by numerical derivation of panel (a), showing discrete energy levels as a result of Coulomb oscillations. The red circles denote experimental data and the blue solid line serves as a guide to the eye. set points: -1.5 V, 0.5 nA

4 Manuscript 2: Carbon Embedding of Pt Cluster Superlattices Templated by Hexagonal Boron Nitride on Ir(111)

This chapter wholly consists of the above-named manuscript and its supplement, published 19th of October 2021 at J. Phys. Chem. C.

The experiments were proposed by T. Hartl, P. Bampoulis and T. Michely. All sample growth and measurements performed at ATHENE were conducted by T. Hartl and D. Herrmann. SXRD measurements were taken at the Petra III beamline at Desy Hamburg, Germany by T. Hartl, P. Bampoulis, D. Herrmann, S. Chung and V. Vonk. A. Stierle assisted in the interpretation of the results. XPS measurements were taken at the Elettra Synchrotron in Trieste, Italy, by T. Hartl, M. Will, P. Bampoulis, P. Lacovig, VB. de la Cruz, S. Lizzit and J. Knudsen. Analysis of all XPS and STM data was performed by T. Hartl. P. Valerius, C. Herbig and J. Knudsen gave guidance during the work with the XPS data. All work was supervised by T. Michely.

T. Hartl wrote the main part of the manuscript and finalized it in close collaboration with T. Michely.

Some of the results shown in this chapter can be found in the Bachelor's thesis of D. Herrmann.

Carbon Embedding of Pt Cluster Superlattices Templated by Hexagonal Boron Nitride on Ir(111)

Tobias Hartl,* Moritz Will, Pantelis Bampoulis, Daniel Herrmann, Philipp Valerius, Charlotte Herbig, Virginia Boix de la Cruz, Paolo Lacovig, Vedran Vonk, Simon Chung, Andreas Stierle, Silvano Lizzit, Jan Knudsen, and Thomas Michely

Cite This: *J. Phys. Chem. C* 2021, 125, 23435–23444

Read Online

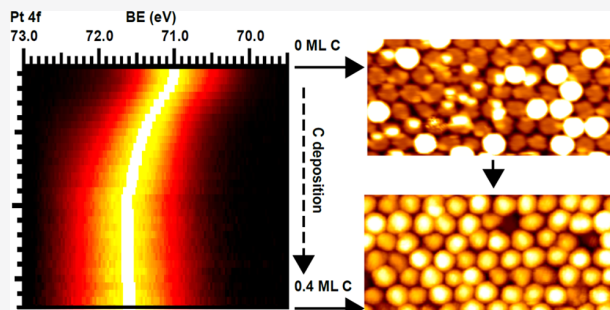
ACCESS |

Metrics & More

Article Recommendations

Supporting Information

ABSTRACT: With the goal to develop the fabrication of a new type of Pt-nanoparticle carbon-support electrocatalyst, we investigate the carbon embedding of Pt cluster superlattices grown on the moiré of a monolayer of hexagonal boron nitride (h-BN) on Ir(111). Our combined scanning tunneling microscopy (STM) and X-ray photoelectron spectroscopy (XPS) study establishes conformal C embedding of the Pt clusters on h-BN/Ir(111) without deterioration of superlattice order, preferential and strong binding of the embedding carbon to the Pt clusters, and upon annealing the formation of a homogeneous amorphous carbon (a-C) matrix. There are indications that while the a-C matrix and the Pt clusters bind strongly to each other, upon annealing both weaken their binding to h-BN.



INTRODUCTION

Novel 2D materials and material systems offer new research opportunities and applications. Examples range from the magic angle bilayer graphene (Gr) that displays superconductivity¹ to carbon nanomembranes that offer new ways for efficient filtering of gases and liquids.^{2,3}

Recently, a first example of a cluster superlattice membrane (CSLM) was fabricated: a new 2D material consisting of a superlattice of similar sized Ir clusters sandwiched between Gr and an amorphous carbon matrix.⁴ The fabrication of this material is based on (i) the templated growth of a superlattice of clusters atop the moiré of a 2D material, e.g., Gr, with a metal substrate, (ii) the embedding of the cluster superlattice into a matrix, e.g., amorphous carbon (a-C), and (iii) the lift-off of the hybrid material from the substrate. CSLMs have potential for new research opportunities in nanocatalysis. For the case of a Pt superlattice, once the 2D layer is stripped off from the membrane, an a-C membrane with very densely spaced Pt catalyst particles of similar size would result. Because of the unique synthesis method, the Pt particles are size-tunable to the atomic limit. As we will show, the Pt particles can be expected to be firmly bound to the a-C matrix and assumed to resist aggregation even under harsh conditions. These properties would make such a membrane an attractive electrocatalyst for fuel cell research.^{5,6}

In the present work we investigate a decisive step in the formation of a Pt cluster superlattice membrane, namely, the embedding into an a-C matrix. The complementary chemical

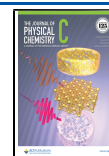
information from XPS and structural information from STM yields a comprehensive picture of the embedding process.

Pt cluster superlattices were templated previously on Gr/Ir(111),^{7,8} Gr/Ru(0001),⁹ alumina films on Ni₃Al(111),¹⁰ monolayer hexagonal boron nitride on Rh(111),^{11,12} and h-BN on Ir(111).¹³ Here we investigate the carbon embedding for Pt/h-BN/Ir(111) because this system has excellent superlattice order and high sintering resistance (no effect up to 650 K)¹³ which make it an attractive candidate for CSLM formation. Because all components of the system (substrate, 2D-layer, clusters, and embedding matrix) are composed of different elements, the chemical processes during carbon embedding can be tracked without ambiguity through XPS. The present study extends our previous combined XPS/STM investigation of binding and thermal stability for Pt/h-BN/Ir(111)¹³ and compares to our carbon embedding investigation for Ir/Gr/Ir(111).¹⁴ The latter had the disadvantage of having the embedding matrix and the 2D-layer being composed of the same chemical element, C, making it difficult to disentangle the processes with XPS.

Received: August 2, 2021

Revised: September 23, 2021

Published: October 19, 2021



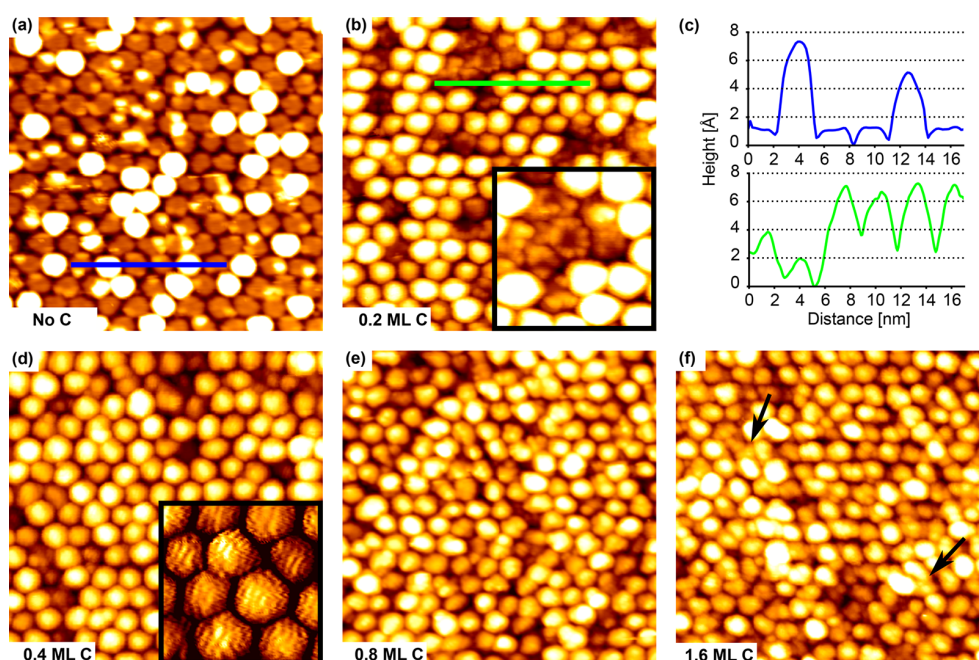


Figure 1. STM topographs of Pt cluster superlattices on h-BN/Ir(111) formed by deposition of 0.55 ML Pt at 300 K (a) without and (b, d–f) with additional C deposited. Carbon amounts are (b) 0.2, (d) 0.4, (e) 0.8, and (f) 1.6 ML. (c) shows the height along the blue line in (a) and the green line in (b). The inset in (d) is a composite of the topograph and its derivative to increase the contrast of the molecular orbital resolution (see text). The image size is 34 nm \times 34 nm in all cases.

Here we thoroughly investigate the structural evolution and the changes in binding between the different membrane components upon increasing amounts of carbon deposited and upon additional thermal annealing. Our investigation establishes not only conformal C-embedding of the Pt clusters on h-BN/Ir(111) without deterioration of superlattice order but also an excellent thermal stability of the embedded Pt superlattice up to 850 K.

Before we present our results, we briefly summarize the knowledge on the h-BN/Ir(111) and Pt cluster superlattices templated thereon to prepare for the results presented below. h-BN/Ir(111) forms a moiré superstructure with (11.7×11.7) h-BN unit cells matching (10.7×10.7) Ir surface unit cells, which results in a 29.1 Å repeat distance. The layer displays one chemisorbed and reactive valley in each moiré unit cell within an otherwise flat, physisorbed mesa.¹⁵ In the valleys, defined by the locations in the moiré where N atoms sit atop Ir substrate atoms, the sp^2 -hybridized h-BN displays partial sp^3 character whereby bonds with the Ir substrate and a reactive spot toward the vacuum are formed.¹⁵ Note that an sp^3 -hybridized layer displays σ -bonds normal to the layer into both half-spaces. Upon deposition of Pt, clusters are formed in the reactive valleys, whereby the sp^3 binding motif is modified and strengthened. Pt clusters are stable against sintering up to 650 K, while for higher temperatures the superlattice decays through intercalation and cluster coalescence.¹³

METHODS

STM was conducted in the ultrahigh-vacuum system Athene in Cologne, and XPS data were recorded at the SuperESCA beamline of Elettra, the synchrotron radiation facility in Trieste, Italy. The base pressure of both systems is in the 10^{-11} mbar range. Ir(111) was cleaned by O_2 glowing at $T = 1100$ K in a pressure of $p_{O_2} = 1 \times 10^{-6}$ mbar for 600 s, followed by

sequences of 2 keV noble gas sputtering and flash annealing to 1500 K.

A gas dosing tube with a pressure enhancement factor of 80 compared to the readout of the ion gauge was used for growth of h-BN in Cologne. At 1250 K the sample was exposed to an ion gauge pressure of $p = 5 \times 10^{-9}$ mbar of borazine ($B_3H_6N_3$) for 30 s, resulting in well-oriented h-BN monolayer islands. Areas without h-BN coverage were later used to calibrate the deposited amount of Pt. At Elettra the borazine pressure was increased to 1×10^{-6} mbar, as no gas dosing tube was installed and the time was increased to 300 s. The absence of room temperature CO adsorption in the XP spectra was used to confirm a 1 ML coverage of h-BN. The h-BN was shown to consist of well-ordered domains via low-energy electron diffraction, both in Cologne and in Trieste.

Pt or C was deposited on the sample from a multiple e-beam evaporator at a typical rate on the order of 5×10^{-3} ML/s, with the Pt ML corresponding to a full layer of pseudomorphic Pt on Ir(111) and the C ML to a fully closed Gr layer. The pressure remained below 2×10^{-10} and 2×10^{-9} mbar during Pt and C deposition, respectively. To enable fast XPS measurements of the sample during deposition, the evaporator was mounted adjacent to the analyzer. The deposition rates were calibrated by determination of the coverage of either Gr or pseudomorphic Pt islands formed on Ir(111) via STM in Cologne with a relative error of about 5% and via the intensity of the C 1s core level in relation to the Ir 4d core level in Trieste with a relative error of 15%.

STM was conducted at room temperature with tunneling currents on the order of $I = 0.5$ nA and a sample bias in the range of $V = \pm 2$ V. STM images have been processed by using the WSxM software.¹⁶

All XP core level spectra were measured in normal emission with an energy resolution better than 50 meV. Ir 4f and Pt 4f

spectra were recorded at a photon energy of $h\nu = 140$ eV, C 1s spectra were measured at $h\nu = 390$ eV, B 1s at $h\nu = 320$ eV, and N 1s at $h\nu = 500$ eV. After calibration of the binding energy (BE) to the Fermi edge a polynomial background was subtracted from the data. Doniach–Šunjić functions convoluted with a Gaussian were used to fit the Ir, C, and N spectra. The Pt core level was fitted with asymmetric pseudo-Voigt functions.

XRD data shown in the Supporting Information were collected at beamline P23 of Petra III/DESY in Hamburg. The sample was prepared in Cologne, exposed to ambient conditions, and later reintroduced into a vacuum of $p = 10^{-8}$ mbar in Hamburg.

RESULTS AND DISCUSSION

Carbon Embedding Characterized by STM. For reference, Figure 1a displays a cluster superlattice on h-BN/Ir(111) after deposition of 0.55 ML Pt at 300 K, without any additional carbon deposition. Each moiré unit cell contains precisely one Pt cluster with a (111) plane parallel to the substrate. Although the clusters are of similar size in atom number with an average of $s_{av} = 63 \pm 8$ atoms per cluster, only clusters of monolayer and trilayer height or above are visible. The height distribution and lack of two layer clusters are a consequence of the collapse of metastable monolayer clusters on the h-BN/Ir(111) moiré as described by Will et al.¹³

Upon deposition of 0.2 ML carbon, many clusters reshape into a multilayer configuration. Remaining monolayer clusters (roughly 15%) show clear signs of carbon adsorption, with carbon decorating the rim of the monolayer clusters as visible in the inset of Figure 1b. Figure 1c shows the line profiles before the deposition of C (blue) and after the deposition of 0.2 ML C (green). Note that the baseline of height in the profiles is somewhat uncertain, as the tip does not reach down to the Gr with certainty. At 0.4 ML carbon deposited (Figure 1d), the cluster superlattice has become more uniform in cluster shape. Molecular orbital resolution, stemming from the adsorbed carbon, is now visible. Still all clusters are distinct and confined to their own moiré unit cell. At higher coverages of 0.8 or 1.6 ML, represented by Figures 1e and 1f, the carbon starts to fill in the space between the clusters and to form a network (see arrows in Figure 1f). Based on the STM topographs, there is no indication that the order of the cluster superlattice is disturbed by C embedding. This is supported by the SXRD data presented in Figure S1 of the Supporting Information, where an Ir cluster superlattice embedding on h-BN/Ir(111) was investigated.¹⁷ In conclusion, the carbon embedding of the Pt cluster lattice on h-BN/Ir(111) proceeds similar as for an Ir cluster lattice on Gr/Ir(111) investigated in ref 14.

Carbon Embedding Analyzed by XPS. XPS measurements, following C deposition, were performed for a Pt cluster superlattice formed by deposition of 0.1 ML Pt on h-BN on Ir(111). The Ir 4f_{7/2} core level of the substrate was measured and fitted with three components: Ir_B attributed to the Ir bulk atoms at the binding energy 60.86 eV (blue in Figure 2a), Ir_S attributed to Ir surface atoms without bonds to h-BN or adsorbates at 60.34 eV (brown in Figure 2a), and Ir_{int} attributed to Ir surface atoms chemically binding to the h-BN at 60.63 eV (ochre in Figure 2a), following the approach of Orlando et al. in ref 18. From the comparison of the two data points in Figure 2b for the relative intensity of Ir_{int} at zero carbon coverage, it is obvious that the interface component is

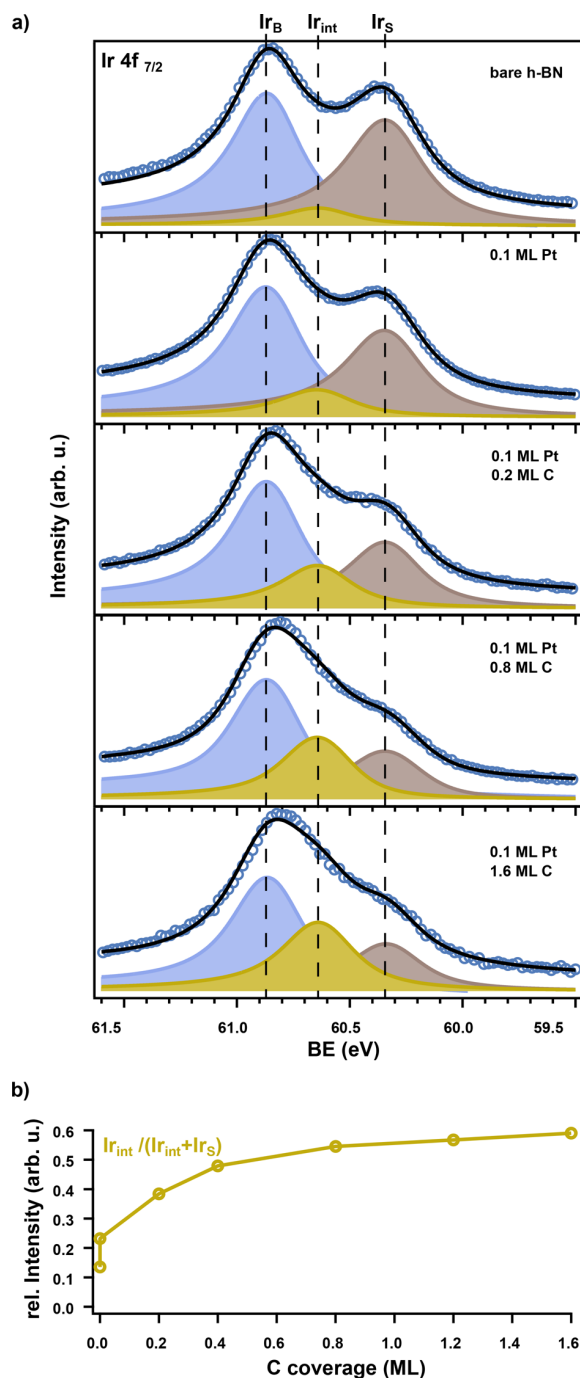


Figure 2. (a) XP spectra of the Ir 4f_{7/2} core level of the Ir(111) substrate with a monolayer of h-BN and after subsequent deposition of 0.1 ML Pt and increasing amounts of carbon measured at a photon energy of $h\nu = 140$ eV at room temperature. The measured data are indicated by blue circles, and the fit is a black line. From top to bottom: pristine h-BN prior to deposition, after deposition of 0.1 ML Pt resulting in bare clusters and after embedding in 0.2, 0.8, and 1.6 ML carbon. (b) Intensity of the interface component (Ir_{int}) normalized to the sum of the interface and surface component (Ir_{int} + Ir_S) as a function of carbon coverage. The lower and upper data points at zero coverage represent the system before and after deposition of 0.1 ML Pt, respectively.

already increased by deposition of 0.1 ML Pt when compared to pristine h-BN on Ir(111). This is due to the formation of Pt clusters, which enlarge the moiré valleys and thus the sp^3 -hybridized h-BN areas binding to Ir surface atoms.^{13,19} After the deposition of 0.2 ML C, the I_{int} component has grown significantly at the expense of the I_{S} component. In good agreement with the observed behavior in the STM topographs, the increase in intensity of the I_{int} peak normalized to the intensity from all Ir surface atoms slows down significantly above 0.8 ML C (Figure 2b), indicating that from this point on the changes taking place are mostly carbon–carbon based interactions. The increase of I_{int} implies an increase of sp^3 hybridization of h-BN, which in turn has to be triggered by chemical bond formation between C and the h-BN sheet. We will see below that these bonds are formed predominantly at the cluster rim.

During carbon embedding the Pt $4f_{7/2}$ core level was monitored via fast-XPS with a time resolution of 1 min per spectrum. As obvious from Figure 3, a significant shift of the

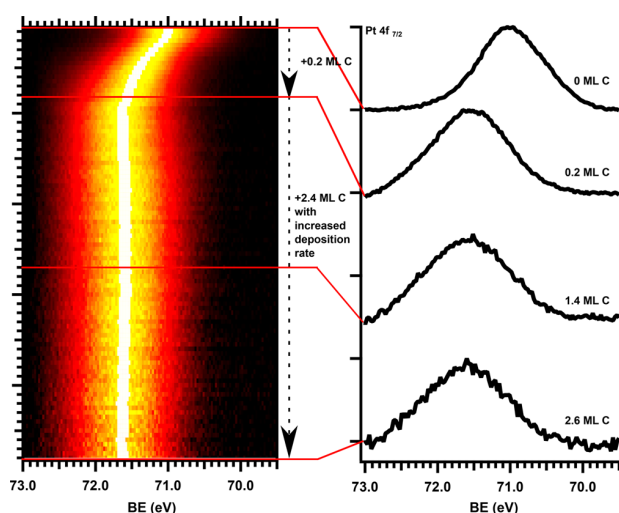


Figure 3. Time-resolved XP spectra of the Pt $4f_{7/2}$ core level during the embedding process of a 0.1 ML Pt cluster superlattice on h-BN/Ir(111). Selected spectra are displayed on the right as line profiles for C coverages of 0, 0.2, 1.4, and 2.6 ML, from top to bottom.

BE from 71.0 to 71.6 eV takes place during the initial stages of the carbon deposition, accompanied by a broadening of the peak. Beyond a C coverage of 0.2 ML the peak position and width remain constant. We interpret these changes as follows: Initially, the deposited C preferentially covers the Pt clusters, similar to the C embedding of iridium clusters.¹⁴ These Pt–C bonds cause a rapid change of the Pt $4f$ level up to 0.2 ML C deposited. Then, the clusters are entirely covered, and no more changes of the Pt $4f$ core level take place.

To obtain insight into the formation of the embedding carbon matrix, the C 1s core level was measured after stepwise deposition of carbon on the cluster superlattice as shown in Figure 4. Because of the multitude of possible binding configurations, the C 1s peak is notoriously difficult to fit for C in an inhomogeneous environment. Here we simplify the situation through a four component fit as shown for the spectrum in Figure 4a, which was recorded after 0.2 ML C deposition. The first component C_{sp^1} at 283.55 eV is attributed to carbon in an sp^1 configuration, that is, linear carbon

multimers or C bound with single bonds to Pt.^{20,21} Note that the majority of carbon species in the vapor arriving at the surface are linear carbon trimers.²² The components C_{sp^2} at 284.1 eV and C_{sp^3} at 285 eV result from sp^2 (graphitic) or sp^3 (diamond-like) hybridized carbon atoms.^{7,23,24} The origin of a broad fourth component C_X , fitted at a BE of 286.9 eV, and of a fifth component C_B indicated in Figure 4a, but not fitted, will be discussed below. The increase in carbon coverage allows the carbon to form bonds to other carbon atoms shifting the intensity from the original C_{sp^1} into the C_{sp^2} and C_{sp^3} components. Figure 4b displays the C 1s spectrum with the same components fitted to it as in (a) after the deposition of 1.6 ML C. The C_{sp^1} component is significantly decreased, while the increase of the C_{sp^2} and C_{sp^3} components signifies that the embedding matrix is an amorphous carbon film with a mixture of sp^2 and sp^3 bonding. The plot of the relative intensities of the fitted components in Figure 4d confirms that the membrane consists of a network of sp^2 - and sp^3 -bonded carbon. The relative and absolute intensity of C_{sp^1} drops because the ratio of carbon in direct contact with the Pt clusters and the h-BN surface shrinks and sp^1 -bonded multimers are integrated into the network, as more and more carbon is deposited.

The broad component C_X , not discussed yet, covers two carbon configurations. First, we have evidence for a slight CO adsorption on clusters from the O 1s core level (data not shown). The corresponding C 1s signature for CO is in the range of 286.9 eV, matching roughly the BE of C_X .²⁵ Moreover, C that forms C–N bonds contributes to C_X . The BE of C–N bonds in the C 1s core level was found to be 287.1 eV, matching the position of C_X quite well.²⁶ Further evidence for the formation of C–N bonds stems from the analysis of the N 1s core level, discussed below. As expected, the relative intensity of C_X drops with increasing amount of C deposited (compare Figures 4b and 4d).

Figure 4a also indicates a component C_B , which has not been fitted, with an estimated BE of 281.5 eV. It decreases with an increase in coverage and appears to vanish at a coverage of 0.8 ML f C (compare Figure 4c). A peak at the same energy and with similar intensity is also present in the C 1s core level spectrum after 0.3 ML carbon deposition on bare h-BN, in the absence of metal clusters (compare Figure S2). A peak with similar binding energy has been observed in C 1s spectra of compounds with a low carbon to boron ratio.^{27,28} Even though the origin of this peak cannot rigorously be deduced, we propose that the peak stems from single C atoms initially forming bonds to the B and disappears when the C is incorporated into the matrix, forming bonds to other C atoms and gaining more of an sp^2/sp^3 character.

The last chemical signatures monitored during embedding are the N 1s and B 1s core levels of the h-BN, shown in Figures 5a and 5b. As h-BN remains intact as a 2D material upon adsorption, changes in both signals are subtle. The broadening of the N 1s and B 1s peaks with C deposition indicates an increased chemical variety of the boron and nitrogen bonds, caused by the interaction of the h-BN layer with the carbon. As obvious from the quantitative analysis of the evolution of the full width at half-maximum (FWHM) with C coverage, the broadening is significantly slowing down as the coverage reaches 0.8 ML (Figure 5c). For 0.8 ML C the h-BN is almost

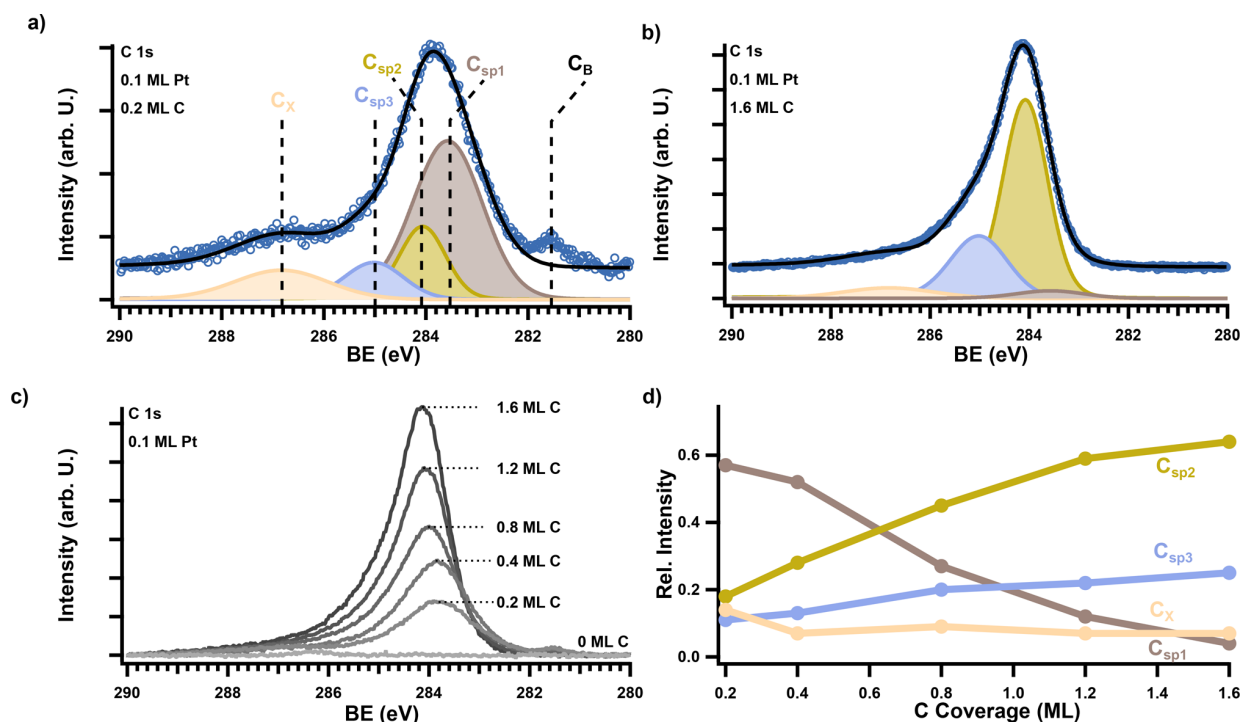


Figure 4. (a, b) XP spectra of the C 1s core level of the embedding carbon covering a 0.1 ML Pt cluster superlattice on h-BN/Ir(111): (a) after embedding in 0.2 ML C and (b) 1.6 ML C. As fit components C_{sp^1} (brown), C_{sp^2} (ochre), and C_{sp^3} (blue) of sp^1 -, sp^2 -, and sp^3 -bonded carbon at BEs of 283.55, 284.1, and 285 eV were used, respectively. An additional component C_x (beige) centered at a BE of 286.9 eV is used to fit the shoulder at the high-energy side (see text). Additionally an unfitted component C_B at a BE of 281.5 eV is indicated (see text). (c) XP C 1s core level spectra after increasing amounts of C deposited on Pt/h-BN/Ir(111). (d) Change of the relative intensities of the fit components in (a, b) as a function of carbon coverage. Lines to guide the eye.

completely covered by C, and newly arriving C binds to already deposited C rather than to h-BN.

The N 1s core level spectrum is fitted with three components. The first two are the N_{mesa} component at 397.62 eV and the N_{valley} component at 398.50 eV, as introduced by Orlando et al.¹⁸ for bare h-BN on Ir(111). The third component N_C , located at the binding energy of 399.4 eV, evolves with carbon deposition (see Figure 5e) and is attributed to carbon–nitrogen bonds, consistent with Yan et al.²⁶ N atoms contributing to this component form bonds with C atoms, which correspond to the C 1s C_x component introduced above. From the intensity of the N_C component it is obvious that only a small fraction of N atoms of the h-BN bind to C atoms (Figure 5e).

Altogether, the XPS data suggest three stages of C embedding for the Pt cluster superlattice. (i) Initially, the deposited C binds preferentially to the Pt clusters and the rehybridized h-BN area along their rim. The small Pt clusters are well saturated with carbon already after deposition of 0.2 ML (compare Figure 3a), and at the rim C–N and C–B bonds are formed (Figure 5c), which reflect through the sp^3 binding motif of h-BN also down to the Ir substrate (Figure 2a). (ii) Upon subsequent deposition more C–N and C–B bonds are formed, but as the geometry for rehybridization is less favorable in the mesa, the induced changes slow down (compare Figures 2a and 5c). (iii) Beyond 0.8 ML deposited essentially the entire h-BN layer including the clusters are covered by C. Therefore, further C deposition leaves the Ir 4f, the B 1s, and N 1s core levels unchanged (compare Figures 2b

and 5c). The closed C film grows in thickness, and changes are only present in the C 1s core level (compare Figure 4).

Annealing and Thermal Stability of an Embedded Cluster Superlattice on h-BN. Besides of fundamental interest, the thermal stability of embedded cluster superlattices is of decisive importance for their subsequent use. Specifically, lift-off of an embedded cluster superlattice from the metal substrate for application in nanocatalysis requires in the case of the Gr/Ir(111) intercalation at elevated temperatures and annealing up to 850 K.⁴ A similar requirement is to be expected for the membrane lift-off from the h-BN/Ir(111) template.

Figure 6 displays STM topographs of an annealing sequence for a 0.55 ML Pt cluster superlattice, embedded with 1.6 ML carbon. The sample without annealing is shown in Figure 6a as a reference. The visible order decreases at 850 K as shown in Figure 6b. The clusters are mostly intact. No large-scale sintering has taken place, as in the case of bare cluster superlattices.¹³ Further annealing to 1050 and 1250 K as shown in Figures 6c and 6d hardly changes the morphology, and even at the highest annealing temperature the carbon cover of the clusters stays intact. The stability of the embedding matrix is quite similar to the case of carbon embedding of Ir cluster superlattices on Gr/Ir(111).¹⁴ However, STM imaging is limited to the embedding matrix, and no information about the encased Pt clusters can be inferred from these topographs.

To gain information about the thermal stability of embedded clusters themselves, fast-XPS measurements of the Pt 4f_{7/2} core level spectrum of a 0.1 ML Pt cluster superlattice were taken

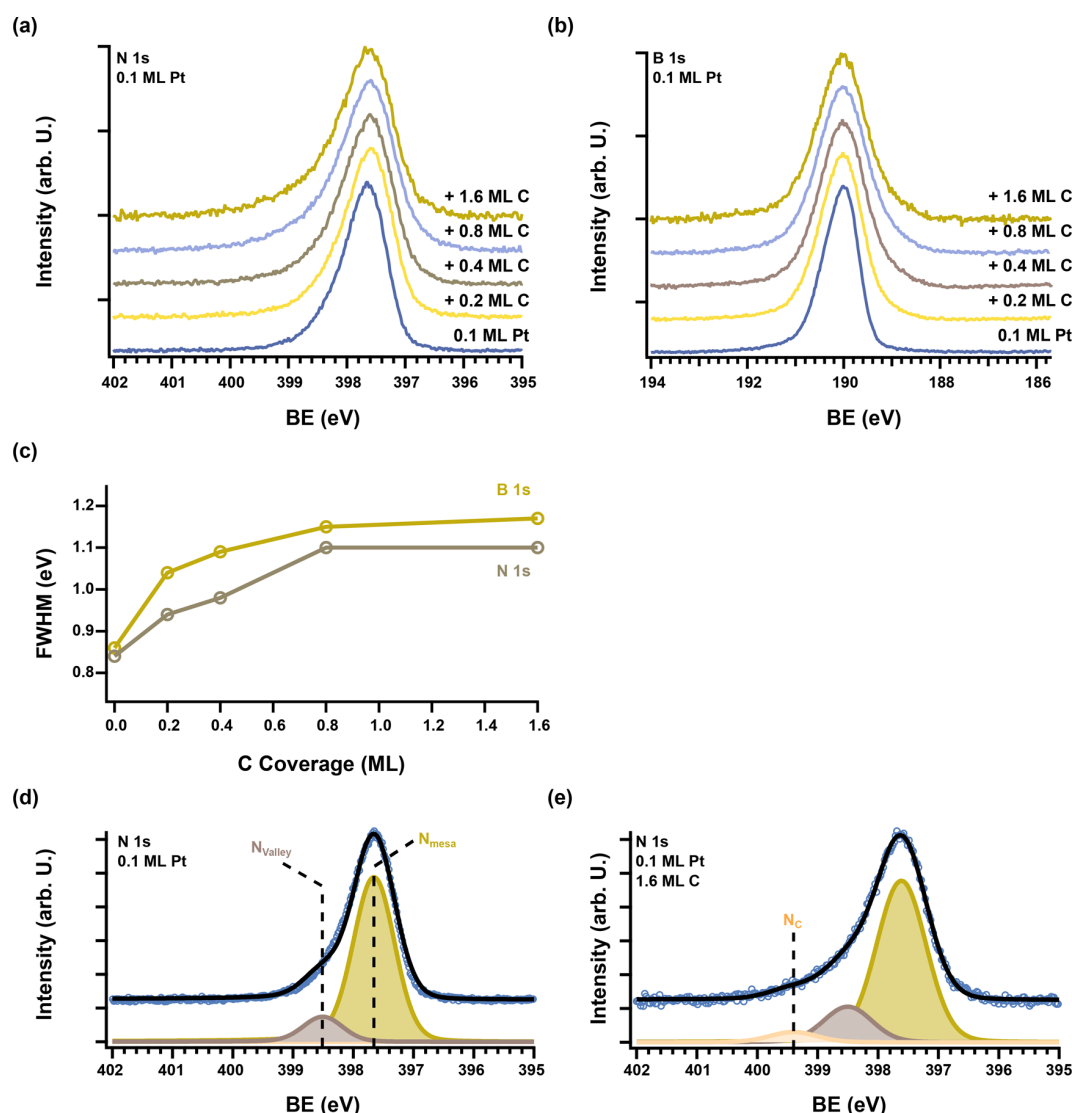


Figure 5. (a, b) Normalized spectra of the (a) N 1s and (b) B 1s peaks of h-BN on Ir(111) with a 0.1 ML Pt cluster superlattice and after stepwise deposition of carbon. (c) Full width at half-maximum of the B 1s and N 1s peaks as a function of carbon coverage. (d, e) Three-component fit of the N 1s peaks of (d) without and (e) with an additional 1.6 ML carbon deposited.

during annealing of the sample as shown in Figure 7a. Two effects of the annealing are visible: A gradual shift toward lower binding energies sets in above 600 K and is finalized at 1000 K. At high temperatures the peak also becomes narrower in the region around its maximum. After the sample has reached 1200 K the heating was switched off, and fast XPS measurements continued during cooling of the sample to 500 K (see bottom part of Figure 7a). During cooldown, thermal broadening diminishes and consequently the Pt $4f_{7/2}$ peak sharpens, without changing its position. The core level shift by about 350 meV toward lower binding energy and the sharpening of the peak indicate irreversible changes in the cluster superlattice.

For quantitative analysis high-resolution spectra after stepwise flash annealing and subsequent cooling to room temperature are more suitable, as thermal broadening is largely absent and equal for all spectra. Figure 7b displays four such spectra fitted with two components: The first component Pt_{cluster} (ochre) is attributed to Pt atoms in the clusters on h-BN, initially centered at 71.8 eV, with freedom to move to

lower binding energies. It matches in FWHM and energetic position the core level spectrum of the unannealed and embedded Pt cluster superlattice, shown as the first spectrum in Figure 7b. The second component, Pt_{int} is attributed to Pt atoms that escaped from their carbon cages and now are intercalated and in direct contact with Ir, as either monolayer island or surface alloy. Its width and energetic position at 71.0 eV are chosen to be identical with the width and energetic position of Pt deposited directly onto Ir(111) and annealed to 1250 K, as shown in the core level spectrum of Figure 7c. We note that the component Pt_{int} cannot be attributed to bulk-like Pt in large compact clusters on h-BN, as according to Figure 6d even after annealing to 1250 K no such clusters formed.

At 850 K the cluster component has slightly shifted in BE down to 71.55 eV, and a small percentage (<5%) of Pt has intercalated. The downshift in binding energy at 850 K is likely to be caused by a reconfiguration of carbon bonds in contact with cluster metal. During this process the bonds are changed, but not lost, as the bare Pt clusters exhibit a BE maximum at

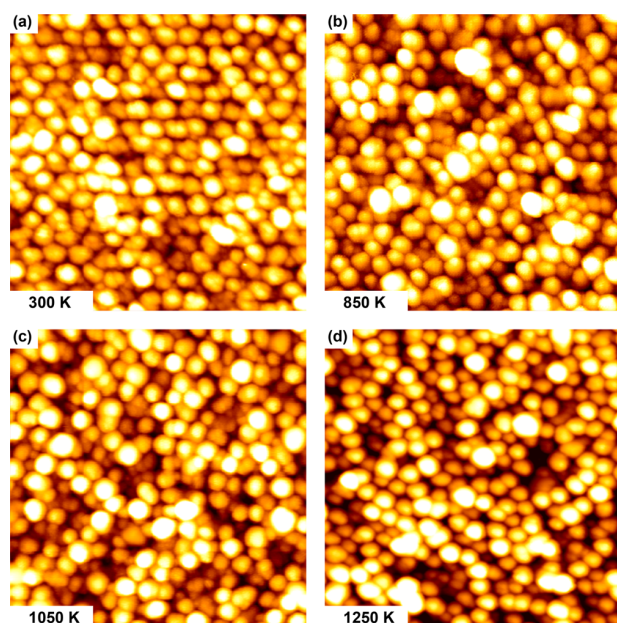


Figure 6. STM topographs of an embedded Pt cluster superlattice, formed by 300 K deposition of 0.55 ML Pt and 1.6 ML C on h-BN/Ir(111): (a) as grown and embedded at room temperature, (b) after annealing to 850 K, (c) after annealing to 1050 K, and (d) after annealing to 1250 K. All images are 34 nm \times 34 nm.

71.0 eV. After annealing to 1050 K roughly 15% of the Pt has intercalated, increasing up to 50% at 1250 K as apparent from Figure 7d. The Pt_{int} signal is additionally attenuated by the h-BN layer, while the $Pt_{cluster}$ is not. In Figure 7d we corrected the intensity for this via $Pt_{int} = Pt_{int,0} \times \exp[d/\lambda]$, with $d = 3.3$ Å, the distance between h-BN and the Ir(111) surface,¹⁵ and λ

$= 9$ Å, the inelastic mean free path, as described in ref 29. Further photoelectron diffraction effects were ignored in this analysis.

Evidently, intercalation is the key decay mechanism of a CSLM based on a monolayer of hexagonal boron nitride. The driving force for intercalation is the substantial energy gain, when the cluster Pt penetrates h-BN and becomes adsorbed to Ir(111). For a CSLM lifted off and flipped around such that the h-BN layer is facing the vacuum, the situation is evidently changed. The cluster metal does not find a better binding site after penetration of the h-BN layer, but just the vacuum. When additionally the amorphous carbon matrix is made thick, e.g., 10 ML instead of 1.6 ML, also penetration of cluster material through the matrix to the new substrate is suppressed. Thus, a higher thermal stability of the CSLMs in this situation can be expected.

The mechanism of Pt intercalation into the space between Ir(111) and h-BN remains elusive. Intercalation through preexisting point defects is one obvious possibility. Such point defects exist in substantial number for h-BN/Ir(111) (compare Figure 4b of ref 19). For the isostructural material Gr and for graphite, point defects were indeed proven to be of crucial relevance for the intercalation of many transition and rare earth metals.^{30–34} A second possible mechanism of intercalation is etching of the engaged Pt metal through the h-BN layer, i.e., high-temperature creation of defects enabling permeation. In fact, metal adatoms were shown to lower the vacancy formation energy in Gr substantially.³⁵

The evolution of the C 1s component during stepwise annealing, plotted in Figure 8, is indicative of a reorganization of the amorphous carbon membrane into a homogeneous amorphous carbon film with a high sp^2 content with increasing temperature. A fit of the data using the same components as for the core level spectra taken during embedding in Figure 4

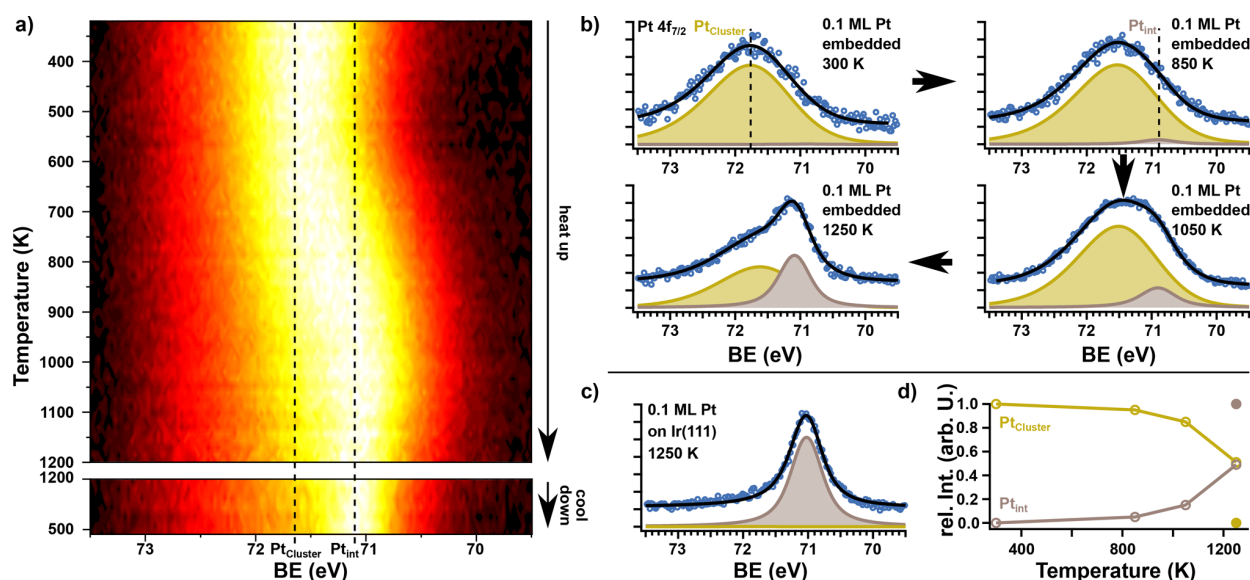


Figure 7. (a) Time-resolved normalized XP spectra of the Pt $4f_{7/2}$ core level during annealing of a 0.1 ML Pt cluster superlattice embedded in 1.6 ML C from 400 to 1200 K (top panel) and subsequently cooling to 500 K (bottom panel). (b) High-resolution spectra of the Pt $4f_{7/2}$ core level fitted with the components $Pt_{cluster}$ for Pt in clusters and Pt_{int} for intercalated Pt. (c) High-resolution spectrum of the Pt $4f_{7/2}$ peak of 0.1 ML Pt directly deposited on Ir(111), annealed to 1250 K, and cooled to RT. (d) Relative intensities of the two components as a function of annealing temperature. The filled circles at 1250 K correspond to the direct Pt on Ir(111) deposition and the open circles to the Pt clusters on h-BN. Lines are to guide the eye.

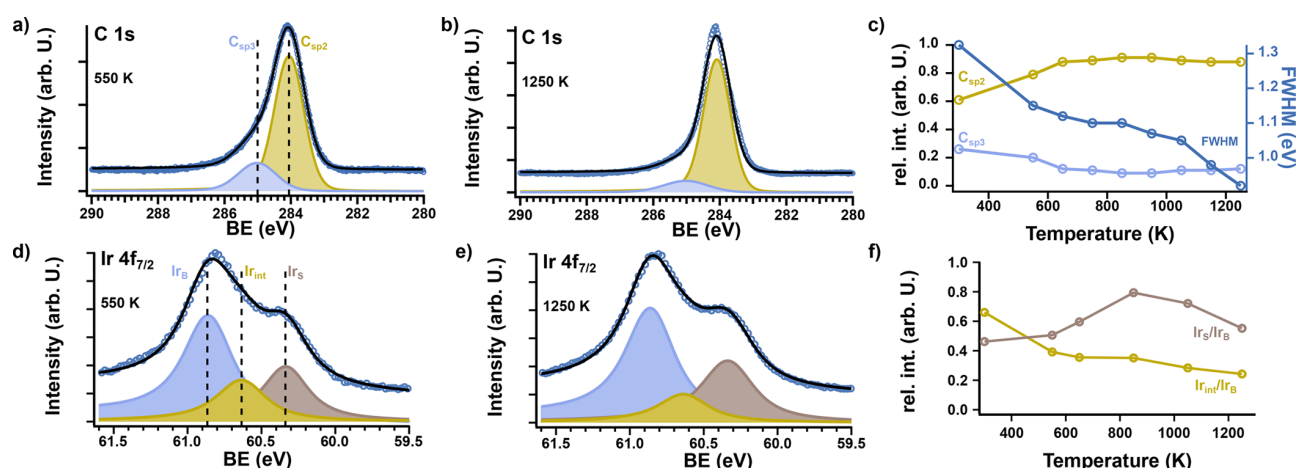


Figure 8. (a, b) XP spectra of the C 1s core level after annealing the 0.1 ML Pt cluster superlattice embedded in 1.6 ML C to (a) 550 K and (b) 1250 K, fitted with the components C_{sp^2} and C_{sp^3} (compare Figure 4). (c) Changes in the integrated relative intensities of the C_{sp^2} and C_{sp^3} components (left y-axis) as well as the total FWHM of the peak (right y-axis) as a function of annealing temperature. (d, e) Spectra of the corresponding Ir 4f_{7/2} core levels of the substrate. The fit uses the same components Ir_B , Ir_S , and Ir_{int} as for the core level spectra in Figure 2. (f) Relative intensities of Ir_S and Ir_{int} plotted as a function of annealing temperature. Lines are to guide the eye.

reveals already after annealing to 550 K (Figure 8a) that the spectrum can be described by only the two components C_{sp^2} and C_{sp^3} . The C_{sp^1} and C_X components have completely vanished. The disappearance of C_{sp^1} shows that the remaining sp^1 -hybridized C has integrated into the C network forming sp^2 or sp^3 bonds, whereby the membrane is stabilized. The disappearance of the C_X component can be traced back to two changes. For CO, which might be trapped in the membrane, the increase in temperature leads to desorption. Moreover, the C–N bonds, which we proposed to contribute to C_X , are apparently broken due to the reorganization of carbon into more favorable bond configurations. The fit after annealing to 1250 K shown in Figure 8b shows that at this point the peak of the C 1s core level has significantly sharpened and consists mostly of sp^2 -hybridized carbon. Figure 8c gives the relative integrated intensities of C_{sp^2} and C_{sp^3} components as a function of annealing temperature. The changes in relative intensities are large until 650 K. Beyond that the relative intensities are almost constant. The strong initial decrease of the FWHM is caused by the decrease of the relative intensity of the C_{sp^3} component, while the decrease above 850 K is due to a decrease in the Gaussian FWHM of the C_{sp^2} component, indicating further reconfiguration in the carbon membrane toward a more uniform embedding matrix.

Lastly, the corresponding Ir 4f_{7/2} core level fits are plotted in Figures 8d and 8e. The quantitative analysis in Figure 8f shows the normalized intensities of the Ir_S and Ir_{int} components as a function of temperature. Up to 850 K the two components evolve complementarily— Ir_S increases and Ir_{int} decreases. Our interpretation is as follows: Upon annealing, the entire membrane reorganizes, whereby the binding between the membrane and the Ir substrate is weakened. Considering that binding of h-BN normal to its plane, i.e., to the substrate and to cluster and a-C matrix, is through the sp^3 binding motif, a weakened binding of h-BN to Ir(111) implies thus also a weakened binding of h-BN to clusters and the a-C matrix. Indeed, the absence of all indications for C–N and C–B bonds in the C 1s spectra after annealing is consistent with this interpretation. Also, scratching experiments with the STM tip

show that the embedding matrix together with the clusters can be removed from the h-BN after heating (compare Figure S3), while this is impossible when Gr is used as a 2D layer.¹⁴ Thus, it appears open whether a lift-off procedure will delaminate the membrane between Ir(111) and the 2D layer—as for Gr—or between the 2D layer and the a-C matrix with the enclosed clusters. The latter would be in fact not unwanted when considering the potential use of the membrane for electrocatalysis, where the Pt metal cluster must display an open surface exposed to the reactants. Experiments to explore the lift-off of the cluster superlattice membrane with h-BN as a 2D layer after annealing to ~850 K are therefore of great interest. Heating beyond 850 K causes intercalation of the Pt cluster material, whereby Ir_{int} decreases—the component characteristic for clusters present in the valleys of the h-BN layer. Ir_S decreases as well, since the intercalated Pt now forms bonds with the surface atoms, whereby these Ir atoms do not contribute anymore to Ir_S .

CONCLUSIONS

We established, through STM topographs and XPS core level analysis, three regimes in the carbon embedding process of cluster superlattices templated on h-BN on Ir(111). First, the incoming carbon binds to the metal clusters and the sp^3 rehybridized area along their rim. This process also leads to a reshaping from the metastable monolayer clusters into multilayer clusters. Second, further C deposition onto the covered clusters then leads to an increase in valley size as more h-BN becomes sp^3 -hybridized. The geometry for hybridization of the h-BN becomes less favorable further away from the original valley and thus limits the amount of C that can form bonds to the h-BN. Third, after all possible bonds are saturated, C starts forming a closed carbon film, which is tunable in thickness and consists mostly of sp^2 - and sp^3 -hybridized carbon compounds. The thermal stability and evolution of the cluster membrane were studied via the same methods, and the embedded clusters were found to be stable up to 850 K. After annealing to this temperature, the amorphous carbon matrix was shown to form a more coherent sp^2/sp^3 -hybridized carbon membrane which is only loosely

bound to the h-BN. Above 850 K the clusters decay via intercalation between h-BN and the Ir substrate. Some clusters remain in the matrix until the highest observed temperature of 1250 K.

■ ASSOCIATED CONTENT

SI Supporting Information

The Supporting Information is available free of charge at <https://pubs.acs.org/doi/10.1021/acs.jpcc.1c06829>.

Reciprocal space map of the ($H = 0, K, L$) plane of a C-embedded cluster superlattice; XP spectra of the C 1s core level of carbon deposited directly on h-BN/Ir(111); STM topograph of a C-embedded cluster superlattice on h-BN/Ir(111) after scratching the surface with the STM tip (PDF)

■ AUTHOR INFORMATION

Corresponding Author

Tobias Hartl – II. Physikalisches Institut, University of Cologne, 50937 Cologne, Germany; orcid.org/0000-0002-3881-5462; Phone: +49 (0)221 470-3480; Email: hartl@ph2.uni-koeln.de

Authors

Moritz Will – II. Physikalisches Institut, University of Cologne, 50937 Cologne, Germany; orcid.org/0000-0003-4822-9122

Pantelis Bampoulis – II. Physikalisches Institut, University of Cologne, 50937 Cologne, Germany; Physics of Interfaces and Nanomaterials, MESA+ Institute for Nanotechnology, University of Twente, 7500 AE Enschede, The Netherlands

Daniel Herrmann – II. Physikalisches Institut, University of Cologne, 50937 Cologne, Germany

Philipp Valerius – II. Physikalisches Institut, University of Cologne, 50937 Cologne, Germany

Charlotte Herbig – II. Physikalisches Institut, University of Cologne, 50937 Cologne, Germany; Department of Physics, University of California, Berkeley, Berkeley, California 94720, United States

Virginia Boix de la Cruz – Division of Synchrotron Radiation Research, Lund University, SE-22100 Lund, Sweden; orcid.org/0000-0002-1152-8201

Paolo Lacovig – Elettra-Sincrotrone Trieste S.C.p.A., I-34149 Trieste, Italy; orcid.org/0000-0001-7001-7930

Vedran Vonk – Deutsches Elektronen-Synchrotron (DESY), 22607 Hamburg, Germany; orcid.org/0000-0001-9854-1101

Simon Chung – Deutsches Elektronen-Synchrotron (DESY), 22607 Hamburg, Germany; orcid.org/0000-0001-8087-8793

Andreas Stierle – Deutsches Elektronen-Synchrotron (DESY), 22607 Hamburg, Germany; orcid.org/0000-0002-0303-6282

Silvano Lizzit – Elettra-Sincrotrone Trieste S.C.p.A., I-34149 Trieste, Italy

Jan Knudsen – Division of Synchrotron Radiation Research, Lund University, SE-22100 Lund, Sweden; MAX IV Laboratory, Lund University, SE-22100 Lund, Sweden

Thomas Michely – II. Physikalisches Institut, University of Cologne, 50937 Cologne, Germany

Complete contact information is available at: <https://pubs.acs.org/doi/10.1021/acs.jpcc.1c06829>

Notes

The authors declare no competing financial interest.

■ ACKNOWLEDGMENTS

This work was funded by the Deutsche Forschungsgemeinschaft (DFG, German Research Foundation) within the project “Cluster Superlattice Membranes” (project no. 452340798). P.B. gratefully acknowledges the financial support from the Alexander von Humboldt Foundation. V.B. and J.K. are grateful for the financial support from the Swedish Research Council Grant 2017-04840 and from the Crafoord Foundation.

■ DEDICATION

This paper is dedicated to the memory of our colleague and friend Patrica A. Thiel, who passed away in September 2020.

■ REFERENCES

- (1) Yankowitz, M.; Chen, S.; Polshyn, H.; Zhang, Y.; Watanabe, K.; Taniguchi, T.; Graf, D.; Young, A. F.; Dean, C. R. Tuning superconductivity in twisted bilayer graphene. *Science* **2019**, *363*, 1059–1064.
- (2) Yang, Y.; Hillmann, R.; Qi, Y.; Korzetz, R.; Biere, N.; Emmrich, D.; Westphal, M.; Büker, B.; Hütten, A.; Beyer, A.; et al. Ultrahigh Ionic Exclusion through Carbon Nanomembranes. *Adv. Mater.* **2020**, *32*, 1907850.
- (3) Naberezhnyi, D.; Götzhäuser, A.; Dementyev, P. Water-Assisted Permeation of Gases in Carbon Nanomembranes. *J. Phys. Chem. Lett.* **2019**, *10*, 5598–5601.
- (4) Hartl, T.; Will, M.; Capeta, D.; Singh, R.; Scheinecker, D.; Boix de la Cruz, V.; Dellmann, S.; Lacovig, P.; Lizzit, S.; Senkovskiy, B. V.; et al. Cluster Superlattice Membranes. *ACS Nano* **2020**, *14*, 13629–13637.
- (5) Ren, X.; Lv, Q.; Liu, L.; Liu, B.; Wang, Y.; Liu, A.; Wu, G. Current progress of Pt and Pt-based electrocatalysts used for fuel cells. *Sustain. Energy Fuels* **2020**, *4*, 15–30.
- (6) Kodama, K.; Nagai, T.; Kuwaki, A.; Jinnouchi, R.; Morimoto, Y. Challenges in applying highly active Pt-based nanostructured catalysts for oxygen reduction reactions to fuel cell vehicles. *Nat. Nanotechnol.* **2021**, *16*, 140–147.
- (7) Knudsen, J.; Feibelman, P. J.; Gerber, T.; Grånäs, E.; Schulte, K.; Stratmann, P.; Andersen, J. N.; Michely, T. Clusters binding to the graphene moiré on Ir (111): X-ray photoemission compared to density functional calculations. *Phys. Rev. B: Condens. Matter Mater. Phys.* **2012**, *85*, 035407.
- (8) N'Diaye, A. T.; Gerber, T.; Busse, C.; Myslivecek, J.; Coraux, J.; Michely, T. A versatile fabrication method for cluster superlattices. *New J. Phys.* **2009**, *11*, 103045.
- (9) Donner, K.; Jakob, P. Structural properties and site specific interactions of Pt with the graphene/Ru (0001) moiré overlayer. *J. Chem. Phys.* **2009**, *131*, 164701.
- (10) Sitja, G.; Bailly, A.; De Santis, M.; Heresanu, V.; Henry, C. R. Regular Arrays of Pt Clusters on Alumina: A New Superstructure on Al₂O₃/Ni₃Al (111). *J. Phys. Chem. C* **2019**, *123*, 24487–24494.
- (11) Düll, F.; Freiburger, E. M.; Bachmann, P.; Steinhauer, J.; Papp, C. Pt Nanoclusters Sandwiched between Hexagonal Boron Nitride and Nanographene as van Der Waals Heterostructures for Optoelectronics. *ACS Appl. Nano Mater.* **2019**, *2*, 7019–7024.
- (12) Düll, F.; Steinhauer, J.; Späth, F.; Bauer, U.; Bachmann, P.; Steinrück, H.-P.; Wickert, S.; Denecke, R.; Papp, C. Ethylene: Its adsorption, reaction, and coking on Pt/h-BN/Rh (111) nanocluster arrays. *J. Chem. Phys.* **2020**, *152*, 224710.
- (13) Will, M.; Hartl, T.; Boix de la Cruz, V.; Lacovig, P.; Lizzit, S.; Knudsen, J.; Michely, T.; Bampoulis, P. Growth, Stability, and Electronic Decoupling of Pt Clusters on h-BN/Ir (111). *J. Phys. Chem. C* **2021**, *125*, 3880.

- (14) Will, M.; Bampoulis, P.; Hartl, T.; Valerius, P.; Michely, T. Conformal Embedding of Cluster Superlattices with Carbon. *ACS Appl. Mater. Interfaces* **2019**, *11*, 40524–40532.
- (15) Farwick zum Hagen, F. H.; Zimmermann, D. M.; Silva, C. C.; Schlueter, C.; Atodiressei, N.; Jolie, W.; Martinez-Galera, A. J.; Dombrowski, D.; Schroder, U. A.; Will, M.; et al. Structure and growth of hexagonal boron nitride on Ir (111). *ACS Nano* **2016**, *10*, 11012–11026.
- (16) Horcas, I.; Fernández, R.; Gomez-Rodriguez, J.; Colchero, J.; Gómez-Herrero, J.; Baro, A. WSXM: a software for scanning probe microscopy and a tool for nanotechnology. *Rev. Sci. Instrum.* **2007**, *78*, 013705.
- (17) Franz, D.; Runte, S.; Busse, C.; Schumacher, S.; Gerber, T.; Michely, T.; Mantilla, M.; Kilic, V.; Zegenhagen, J.; Stierle, A. Atomic structure and crystalline order of graphene-supported Ir nanoparticle lattices. *Phys. Rev. Lett.* **2013**, *110*, 065503.
- (18) Orlando, F.; Larciprete, R.; Lacovig, P.; Boscarato, I.; Baraldi, A.; Lizzit, S. Epitaxial growth of hexagonal boron nitride on Ir (111). *J. Phys. Chem. C* **2012**, *116*, 157–164.
- (19) Will, M.; Atodiressei, N.; Caciuc, V.; Valerius, P.; Herbig, C.; Michely, T. A monolayer of hexagonal boron nitride on Ir (111) as a template for cluster superlattices. *ACS Nano* **2018**, *12*, 6871–6880.
- (20) Hu, A.; Rybachuk, M.; Alkhesho, I.; Lu, Q.-B.; Duley, W. Nanostructure and sp¹/sp² clustering in tetrahedral amorphous carbon thin films grown by femtosecond laser deposition. *J. Laser Appl.* **2008**, *20*, 37–42.
- (21) Rodriguez, N.; Anderson, P.; Wootsch, A.; Wild, U.; Schlögl, R.; Paál, Z. XPS, EM, and catalytic studies of the accumulation of carbon on Pt black. *J. Catal.* **2001**, *197*, 365–377.
- (22) Weltner, W., Jr.; Van Zee, R. J. Carbon molecules, ions, and clusters. *Chem. Rev.* **1989**, *89*, 1713–1747.
- (23) Chavanne, A.; Arnault, J.-C.; Barjon, J.; Arabski, J. Bias-enhanced nucleation of diamond on iridium: A comprehensive study of the first stages by sequential surface analysis. *Surf. Sci.* **2011**, *605*, 564–569.
- (24) Herbig, C.; Knispel, T.; Simon, S.; Schroeder, U. A.; Martinez-Galera, A. J.; Arman, M. A.; Teichert, C.; Knudsen, J.; Krashennnikov, A. V.; Michely, T. From permeation to cluster arrays: graphene on Ir (111) exposed to carbon vapor. *Nano Lett.* **2017**, *17*, 3105–3112.
- (25) Björneholm, O.; Nilsson, A.; Tillborg, H.; Bennich, P.; Sandell, A.; Hernnäs, B.; Puglia, C.; Mårtensson, N. Overlayer structure from adsorbate and substrate core level binding energy shifts: CO, CCH₃ and O on Pt (111). *Surf. Sci.* **1994**, *315*, L983–L989.
- (26) Yan, X.; Xu, T.; Chen, G.; Yang, S.; Liu, H.; Xue, Q. Preparation and characterization of electrochemically deposited carbon nitride films on silicon substrate. *J. Phys. D: Appl. Phys.* **2004**, *37*, 907.
- (27) Ottaviani, B.; Derré, A.; Grivei, E.; Mahmoud, O. A. M.; Guimon, M.-f.; Flandrois, S.; Delhaès, P. Boronated carbons: structural characterization and low temperature physical properties of disordered solids. *J. Mater. Chem.* **1998**, *8*, 197–203.
- (28) Oliveira, M. N.; Botelho do Rego, A. M.; Conde, O. XPS investigation of BxNyCz coatings deposited by laser assisted chemical vapour desposition. *Surf. Coat. Technol.* **1998**, *100-101*, 398–403.
- (29) Sutter, P.; Sutter, E. Thickness determination of few-layer hexagonal boron nitride films by scanning electron microscopy and Auger electron spectroscopy. *APL Mater.* **2014**, *2*, 092502.
- (30) Lii-Rosales, A.; Han, Y.; Evans, J. W.; Jing, D.; Zhou, Y.; Tringides, M. C.; Kim, M.; Wang, C.-Z.; Thiel, P. A. Formation of multilayer Cu islands embedded beneath the surface of graphite: characterization and fundamental insights. *J. Phys. Chem. C* **2018**, *122*, 4454–4469.
- (31) Liu, Y.; Liu, X.; Wang, C.-Z.; Han, Y.; Evans, J. W.; Lii-Rosales, A.; Tringides, M. C.; Thiel, P. A. Mechanism of Metal Intercalation under Graphene through Small Vacancy Defects. *J. Phys. Chem. C* **2021**, *125*, 6954–6962.
- (32) Sicot, M.; Leicht, P.; Zusan, A.; Bouvron, S.; Zander, O.; Weser, M.; Dedkov, Y. S.; Horn, K.; Fonin, M. Size-selected epitaxial nanoislands underneath graphene moiré on Rh (111). *ACS Nano* **2012**, *6*, 151–158.
- (33) Coraux, J.; N'Diaye, A. T.; Rougemaille, N.; Vo-Van, C.; Kimouche, A.; Yang, H.-X.; Chshiev, M.; Bendiab, N.; Fruchart, O.; Schmid, A. K. Air-protected epitaxial graphene/ferromagnet hybrids prepared by chemical vapor deposition and intercalation. *J. Phys. Chem. Lett.* **2012**, *3*, 2059–2063.
- (34) Schumacher, S.; Huttman, F.; Petrović, M.; Witt, C.; Förster, D. F.; Vo-Van, C.; Coraux, J.; Martinez-Galera, A. J.; Sessi, V.; Vergara, I.; et al. Europium underneath graphene on Ir (111): Intercalation mechanism, magnetism, and band structure. *Phys. Rev. B: Condens. Matter Mater. Phys.* **2014**, *90*, 235437.
- (35) Boukhvalov, D.; Katsnelson, M. Destruction of graphene by metal adatoms. *Appl. Phys. Lett.* **2009**, *95*, 023109.

Supporting Information: Carbon Embedding of Pt Cluster Superlattices Templated by Hexagonal Boron Nitride on Ir(111)

Tobias Hartl,^{*,†} Moritz Will,[†] Pantelis Bampoulis,^{†,⊥} Daniel Herrmann,[†] Virginia
Boix de la Cruz,[‡] Paolo Lacovig,[¶] Vedran Vonk,[§] Simon Chung,[§] Andreas
Stierle,[§] Silvano Lizzit,[¶] Jan Knudsen,^{‡,||} and Thomas Michely[†]

[†]*II. Physikalisches Institut, University of Cologne, 50937 Cologne, Germany*

[‡]*Division of Synchrotron Radiation Research, Lund University, Box 188, SE-22100 Lund,
Sweden*

[¶]*Elettra-Sincrotrone Trieste S.C.p.A., Strada Statale 14 Km 163.5, I-34149 Trieste, Italy*

[§]*Deutsches Elektronen-Synchrotron (DESY), 22607 Hamburg, Germany.*

^{||}*MAX IV Laboratory, Lund University, Box 118, SE-22100 Lund, Sweden*

[⊥]*Physics of Interfaces and Nanomaterials, MESA+ Institute for Nanotechnology,
University of Twente, P.O. Box 217, 7500 AE Enschede, The Netherlands*

E-mail: hartl@ph2.uni-koeln.de

Phone: +49 (0)221 470-3480

Supporting Information Available

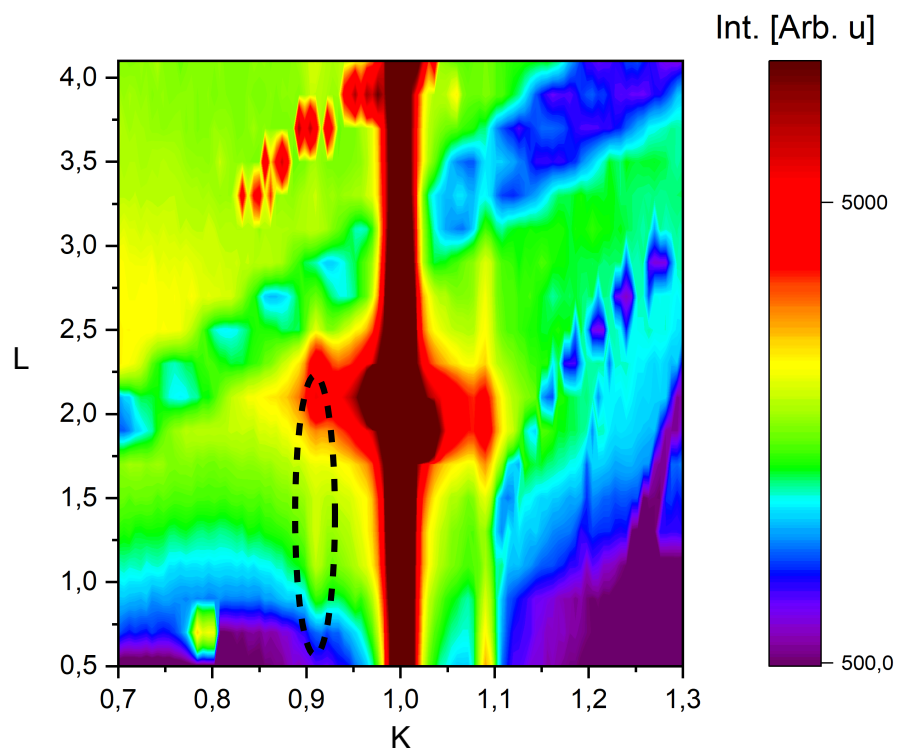


Figure S1: Reciprocal space map of the ($H=0, K, L$) plane after the deposition of 0.5 ML Ir clusters on h-BN/Ir(111) embedded in 2 ML C. The signal at ($H=0, K=0.91, L$), highlighted by the dashed ellipse, indicates the presence of a cluster superlattice below the carbon embedding. The correlation length, derived from profiles at constant L is 20 nm.¹

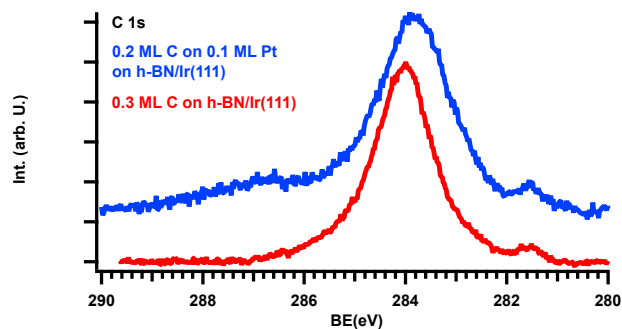


Figure S2: XP Spectra of the C 1s core level of carbon deposited either directly on h-BN/Ir(111) (red), or on 0.1 ML Pt clusters on h-BN/Ir(111) (blue).

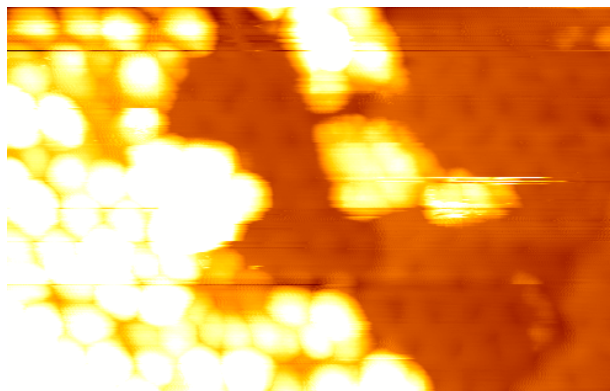


Figure S3: STM topograph of 0.55 ML Pt deposited on h-BN, embedded in 1.6 ML C after annealing to 1250 K and scratching the surface with the STM tip (right side). The carbon matrix with the clusters (left side) can be entirely removed from the h-BN, a process that is impossible if Gr is used as a 2D layer. The image size is 43 nm x 28 nm.

References

- (1) Franz, D.; Runte, S.; Busse, C.; Schumacher, S.; Gerber, T.; Michely, T.; Mantilla, M.; Kilic, V.; Zegenhagen, J.; Stierle, A. Atomic structure and crystalline order of graphene-supported Ir nanoparticle lattices. *Phys. Rev. Lett.* **2013**, *110*, 065503.

5 Manuscript 3: Silicon Cluster Arrays on the Monolayer of Hexagonal Boron Nitride on Ir(111)

This chapter wholly consists of the above-named manuscript, published 6th of April 2022 at J. Phys. Chem. C.

The experiments were proposed by T. Hartl, P. Bampoulis and T. Michely. All sample growth and measurements performed at ATHENE were conducted by T. Hartl and P. Bampoulis. STM analysis was performed by T. Hartl. STS analysis was performed by P. Bampoulis. Y. Falke and A. Grüneis gave experimental guidance. All work was supervised by T. Michely.

The manuscript was written in close collaboration by T. Hartl, T. Michely and P. Bampoulis

Silicon Cluster Arrays on the Monolayer of Hexagonal Boron Nitride on Ir(111)

Tobias Hartl, Daniel Herrmann, Moritz Will, Yannic Falke, Alexander Grüneis, Thomas Michely, and Pantelis Bampoulis*



Cite This: *J. Phys. Chem. C* 2022, 126, 6809–6814



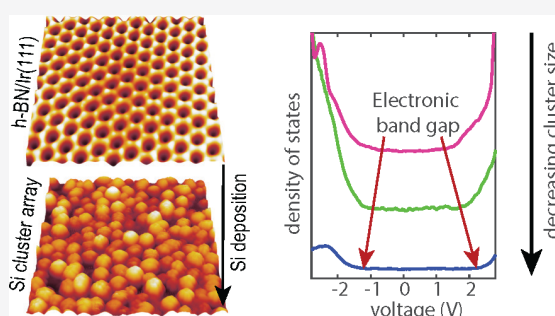
Read Online

ACCESS |

Metrics & More

Article Recommendations

ABSTRACT: Periodic structures of silicon are of interest in quantum-dot-based applications because of their unique optical and electronic properties. We report on the fabrication of stable quasi-ordered Si nanocluster arrays on the moiré of a hexagonal boron nitride (h-BN) monolayer on Ir(111). The h-BN monolayer promotes the growth of regular Si nanoclusters at 130 K and electronically decouples the clusters from the underlying metallic substrate. Using scanning tunneling microscopy and spectroscopy, we have investigated the cluster binding sites, their electronic structure, and their thermal stability. We find that the clusters display a size-dependent bandgap and that they are stable up to 577 K, after which cluster coalescence degrades the arrays.



INTRODUCTION

Nanostructured materials exhibit novel and tunable properties that are much different from their bulk counterparts, and therefore hold great promise to advance current applications and inspire future ones.^{1–3} Recent advancements in the formation of cluster superlattices with exceptional long-range order and controllable cluster sizes provide a roadmap to design bottom-up functional materials with the desired catalytic and electronic properties.^{4–11} The fabrication of a silicon cluster superlattice is motivated by the clusters' potential in electronic and spintronic devices. For example, Si quantum dots have shown promise as active materials in qubit architectures for quantum computing^{12–14} and display interesting charge transport characteristics.¹⁵ Moreover, the photoluminescence and high quantum yield of Si nanoclusters make them also an interesting material for optoelectronic applications. The quantum size effect, resulting in a blue-shift of the energy gap, and surface passivation effects, limiting nonradiative recombination processes, are believed to be the heart of these optical properties.^{16–22}

Despite the significance of Si to the current electronic industry, superlattices of small and stable Si nanoclusters have yet to be realized. Fabrication reproducibility and cluster disorder pose significant challenges, which could potentially limit the effectiveness and predictability of Si-cluster-based systems. The scalable fabrication of well-ordered arrays of Si nanoclusters integrated on an insulating substrate is anticipated to enable better utilization of their properties and encourage the use of Si clusters to advance the existing information technology. The use of similar-sized cluster arrays will allow

easy patterning of electrical contacts anywhere on the array, making devices containing the desired cluster density.²³ Furthermore, the identical environment and similar size of the clusters will provide a collective response without smearing out the single cluster properties.

A monolayer of h-BN on Ir(111) system is an excellent template to grow arrays of similar-sized clusters. It provides (i) periodic nucleation sites where deposition of atoms lead to the growth of epitaxial and similar sized clusters,^{24,25} (ii) the large bandgap of h-BN electronically decouples nanoclusters from the metallic Ir(111), preserving and allowing to measure their electronic structure.²⁵ We demonstrate that Si forms a quasi-ordered network of small clusters on h-BN when deposited at 130 K and have identified their binding sites. The Si nanoclusters display a wide range of sizes implying a large variety of the number of atoms between different clusters. Moreover, the nanoclusters are electronically decoupled from the underlying substrate and have a size-dependent energy bandgap.

EXPERIMENTAL METHODS

Sample preparation, STM, and LEED imaging were conducted in the ultrahigh-vacuum system ATHENE in Cologne. The

Received: January 28, 2022

Revised: March 25, 2022

Published: April 6, 2022



background base pressure was in the 10^{-11} mbar regime. Cleaning of the Ir(111) crystal was done by using several cycles of 2 keV Xe⁺ sputtering and flash annealing to 1550 K. The h-BN monolayer was grown on Ir(111) by exposure to a background pressure of 5×10^{-9} mbar of borazine (B₃N₃H₆) at 1230 K. Borazine exposure was through a gas dosing tube which enhances the pressure at the sample location by a factor of 80. The h-BN monolayer was grown to near completion coverage as confirmed by STM and LEED experiments.

Si was evaporated on h-BN/Ir(111) and Ir(111) at 130 and 300 K from a home-built Si evaporator with a deposition rate of 0.11 MLE/min at an evaporation pressure around 1×10^{-9} mbar. The deposited amount θ was calibrated by Si deposition onto clean Ir(111) and subsequent annealing to 670 K for 30 min. The heating step leads to the formation of compact Si-induced islands. As we show in the main text, STM imaging was used for the determination of the island coverage and thus the deposition flux. The deposited amount of Si is given in monolayers with respect to the surface atomic density of Ir(111).

STM imaging was done at room temperature by using tunneling currents I in the range $I = 0.1$ – 0.6 nA and sample bias voltages U_s in the range $U_s = -(0.8$ – $2.0)$ V. The STM data were processed (background subtraction and contrast adjustment) by using the WSxM software.²⁶

RESULTS AND DISCUSSION

Figure 1a shows a large-scale scanning tunneling microscopy (STM) image of the Ir(111) surface after exposure to Si vapor at 300 K and annealing to 670 K for 30 min. The inset depicts structures (small clusters and wires) formed just after Si deposition at 300 K. After annealing, small Si-induced islands (marked with a black dashed outline) cover about 10% of the surface. The patches are grouped into two domains rotated by 13° with respect to each other as seen also in the fast Fourier transformation (FFT) of the topograph in Figure 1b. Figure 1c shows an atomically resolved image of a Si-induced island next to bare Ir(111). The island exhibits a complex reconstruction strongly resembling the $(\sqrt{19} \times \sqrt{19}) R23^\circ$ reconstruction of the Si/Pt(111) system seen in STM and diffraction experiments.^{27,28} Similar to Si/Pt(111), (i) the reconstructed Si/Ir(111) surface is located in the same atomic layer as the Ir(111)-(1 \times 1), and the Ir(111)-(1 \times 1) surface has the same level of apparent height with the basis of the Si-induced reconstruction; (ii) the reconstructed surface is modified by triangular-shaped features of dark and bright contrast rotated by about 23° with respect to the main directions of Ir(111); and (iii) it can be accurately described as a $(\sqrt{19} \times \sqrt{19}) R23^\circ$ superstructure. The unit cell of the superstructure is indicated in Figure 1c, in which bright and dark triangular intrusions are in the unit cell. Therefore, the same atomistic model as for Si/Pt(111), in which the building block of the reconstruction is a Si₃Pt tetramer, can be adapted to Si/Ir(111). These observations rule out the growth of silicene on Ir(111) for submonolayer amounts of Si, in line with ref 29.

To limit Si–Ir alloying during cluster formation, we cover the Ir(111) crystal with a complete monolayer of h-BN. Figure 2a is a large-scale STM image of h-BN on Ir(111). The lattice mismatch between the two surfaces leads to the formation of a long-range moiré. The moiré periodicity amounts to 2.91 nm, a consequence of (11.7×11.7) h-BN unit cells matching (10.7×10.7) Ir unit cells.³⁰ Atomic-scale STM imaging (inset of

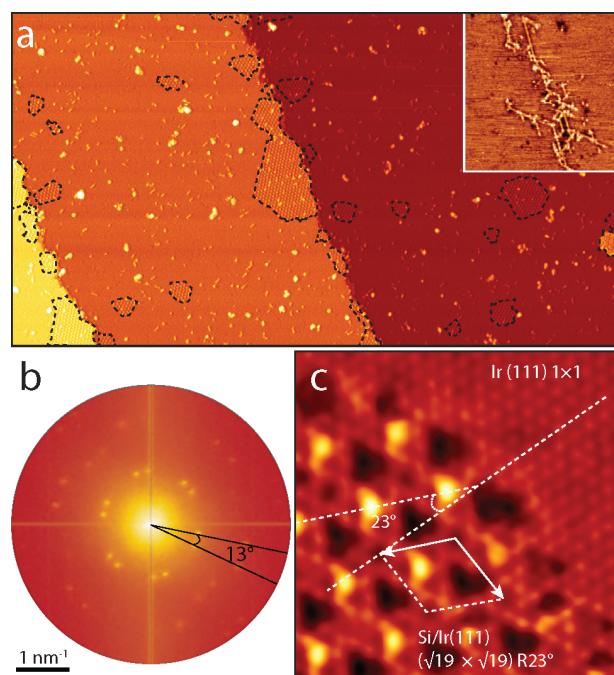


Figure 1. (a) Scanning tunneling microscopy (STM) topograph of Si-induced islands (marked with a black dashed outline) on Ir(111) after the deposition of Si at 300 K and annealing to 670 K for 30 min. Inset: Si-induced surface structures before the annealing step. (b) The corresponding FFT image revealing the two domains of the islands rotated by 13° . (c) An atomic scale STM image at the boundary of a Si-induced island and the Ir(111) pristine surface. The unit cell of the $(\sqrt{19} \times \sqrt{19}) R23^\circ$ superstructure is overlaid on the image. The image sizes are $220 \text{ nm} \times 120 \text{ nm}$ in (a), $33 \text{ nm} \times 33 \text{ nm}$ in the inset of (a), and $5 \text{ nm} \times 5 \text{ nm}$ in (c).

Figure 2a) reveals the h-BN atomic lattice—a honeycomb lattice with a period of 0.248 nm.³⁰ The corresponding FFT (Figure 2b) shows the first- and second-order moiré spots. Chemisorbed valleys appear as either dark depressions or bright protrusions with a darker interior depending on sample bias. They are separated by flat physisorbed mesas.³⁰ In the valleys, N atoms sit atop Ir atoms, leading to a partial sp^3 hybridization in h-BN and a higher reactivity at these sites.³⁰ Deposition of metals or C atoms on h-BN/Ir(111) results in the formation of regular arrays of clusters.^{24,25} The clusters bind at the chemisorbed valleys modifying and strengthening the sp^3 binding motif.²⁵ Almost perfect superlattices of a variety of elements have been already created on h-BN/Ir(111).^{24,25} These cluster superlattices display high thermal stability. For example, Ir and Pt cluster superlattices on h-BN/Ir(111) retain their order and number density up to 700 K,^{24,25} more than 100 K higher temperatures than on h-BN/Rh(111)^{31,32} and about 200 K higher than on Gr/Ir(111).³³ In addition, h-BN provides electronic decoupling of the clusters from the underlying metallic substrate.²⁵

Deposition of 0.2 ML of Si on h-BN/Ir(111) at 300 K leads to the formation of small clusters and islands randomly scattered across the h-BN; compare Figure 2c and the corresponding FFT image in Figure 2d. This is in sharp contrast to the well-defined metal cluster superlattices,^{24,25} indicating high mobility of the Si atoms on h-BN/Ir(111) at 300 K. To reduce the mobility of Si atoms, 0.2 ML of Si was deposited on h-BN at 130 K. At variance with the 300 K

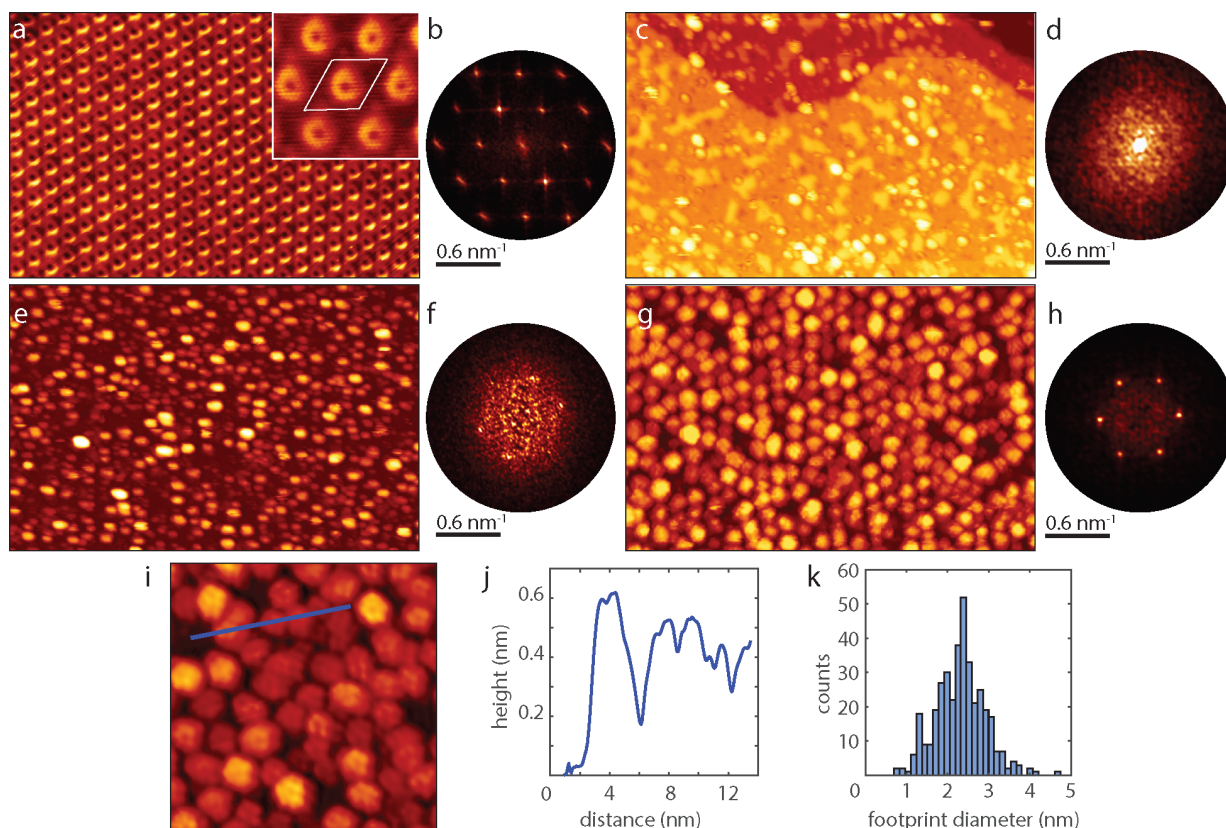


Figure 2. (a) Large-scale STM topograph of h-BN/Ir(111) showing the moiré superlattice. Inset: atomically resolved STM image of the h-BN/Ir(111) moiré superlattice with moiré unit cell indicated by the diamond of black lines. (b) The corresponding FFT image reveals the moiré spots. (c) The same sample after deposition of 0.2 ML of Si at 300 K; small Si clusters and islands are randomly scattered across the surface. This is also reflected by the diffuse FFT image in (d). (e) STM image of small Si clusters formed after deposition of 0.2 ML of Si on the clean h-BN/Ir(111) at 130 K. The Si nanoclusters display first signs of order reflected in the appearance of faint moiré spots in the FFT image in (f). (g) STM image of a Si cluster array formed after deposition of 0.4 ML of Si on the clean h-BN/Ir(111) at 130 K. The Si nanoclusters are quasi-ordered. (h) The corresponding FFT image shows the moiré spots. (i) Atomically resolved STM image of the Si nanoclusters on the h-BN/Ir(111) moiré. (j) Line profile across several clusters acquired along the blue line in (i). (k) A distribution of the footprint diameter of the clusters depicted in panel (g). The image sizes are 60 nm \times 40 nm in (a), (c), (e), and (g), 13 nm \times 13 nm in (i), and 7.5 nm \times 7.5 nm in the inset of (a).

results, Si deposition at 130 K promotes self-organization of Si into small clusters covering the surface. The previously observed islands are absent (Figure 2e). Note that STM imaging is conducted at room temperature. The clusters show the first signs of order; weak but visible moiré spots can be discerned in the corresponding FFT image (Figure 2f).

Deposition of 0.4 ML of Si at 130 K improves cluster ordering and regularity. Figure 2g is an STM image recorded at room temperature of Si clusters formed after the deposition of 0.4 ML of Si on h-BN at 130 K. The corresponding FFT image (Figure 2h) shows well-defined hexagonal spots, indicating that many of the clusters follow the moiré periodicity of h-BN on Ir(111), forming an imperfect Si cluster superlattice. Several clusters are displaced from the superlattice points. There is also a small fraction of clusters occupying more than one lattice site.

High-resolution imaging of the clusters (Figure 2i) reveals a cluster structure resembling the molecular orbitals observed on C clusters,³⁴ fullerenes,^{35,36} and sp^2 -nanodiamonds.³⁷ This observation indicates that the Si clusters might be predominantly sp^2 -hybridized. The observation is in line with the notion of endohedral Si fullerenes as a stable structural model for Si clusters consisting of a few tens of atoms.^{38–40} In earlier theoretical studies the most stable cluster motif assumes a

spherical compact structure, similar to the carbon fullerene cages. But in contrast to the empty C fullerenes, endohedral Si fullerenes consist of two shells of atoms. The outer shell is a fullerene-like sp^2 -hybridized cage surrounding the inner shell, which is composed of stable atoms with saturated dangling bonds.³⁸ Figure 2j shows a line profile across several Si clusters (the location is indicated with the blue line in Figure 2i). The clusters have a height of about 0.5 nm, indicating a monolayer or a bilayer atom cage. Moreover, the clusters exhibit a wider range of lateral sizes (see the distribution of the footprint diameter in Figure 2k) compared to regular cluster superlattices,^{24,25} implying a substantial variation of the number of Si atoms between different clusters. As is obvious from the STM and corresponding FFT images of Figure 2, the Si clusters have inferior order compared to the lattices formed by Pt, Ir, and C clusters on h-BN/Ir(111).^{24,25}

To determine the preferred binding sites of Si clusters on h-BN, we intentionally removed several Si nanoclusters with the STM tip (Figure 3). This is achieved by scanning under low tunneling resistance conditions, suggesting a weak binding between Si and h-BN. The underlying h-BN moiré superlattice becomes again visible after cluster removal but appears to be defective. Nevertheless, the moiré lattice directions and the valley regions (darker regions) can be identified; these are the

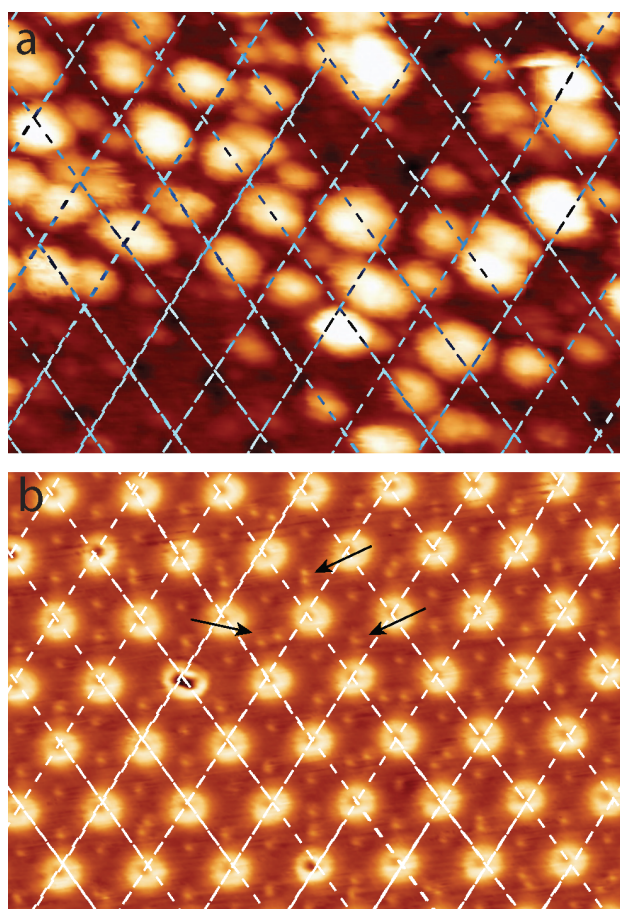


Figure 3. (a) STM topograph after deposition of 0.4 ML Si at 130 K and imaging at 300 K. In the lower half, the Si clusters have been removed with the STM tip. The grid of white dashed lines is matched to the center of the h-BN moiré valleys. (b) Atomically resolved STM image of the h-BN/Ir(111) moiré superlattice containing point defects (indicated with the black arrows) at the h-BN mesas. The image size is 20 nm \times 15 nm in (a) and (b).

positions where the overlaid white dashed lines in Figure 3a cross each other. Surprisingly most of the clusters sit within mesa regions of the h-BN or are off-centered from the valleys. This observation suggests a preference toward the binding of Si to the mesa of h-BN. In comparison, clusters of Pt, Ir, and C bind at the more reactive valleys, i.e., regions where h-BN hybridizes with Ir.^{24,25} At the mesa regions, it is common to find point defects already prior to deposition of Si, such as the ones visible in Figure 3b. The dangling bonds associated with such point defects and the orientation-specific Si bonds (contrary to metals) could be the cause of the stronger binding of Si at these locations. These competing binding sites lead to the imperfect order of the clusters.

Scanning tunneling spectroscopy was employed to study the electronic structure of Si nanoclusters on h-BN. Figure 4 shows numerically derived dI/dV (V) curves obtained on small (footprint diameter smaller than 1.5 nm), intermediate (footprint diameter of 2 ± 0.5 nm), and large Si clusters (footprint diameter larger than 2.5 nm) compared to the bare h-BN regions. Each curve is the result of averaging about 100 obtained on different but similarly sized clusters marked with blue for small clusters, green for intermediate clusters, and magenta for large clusters. While hBN exhibits no clear

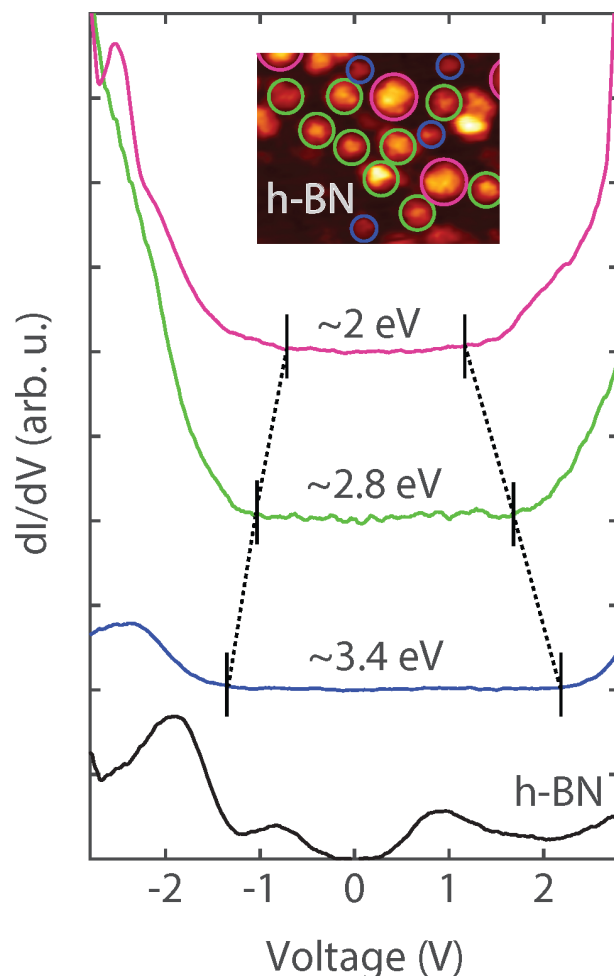


Figure 4. (a) Differential conductance dI/dV as a function of bias voltage V taken on h-BN/Ir(111) (black), small (blue), intermediate (green), and large (magenta) clusters, marked with the corresponding color in the topography inset (size: 13 nm \times 16 nm). The spectra are the result of averaging over single spectra recorded at the center of Si clusters of similar size.

bandgap as a result of the hybridization of h-BN with Ir, the nanoclusters are clearly semiconductive. The h-BN template has sufficiently decoupled the nanoclusters from the underlying metal. Quantum confinement in the nanoclusters leads to an electronic bandgap that strongly depends on their size. Small clusters have a bandgap of about 3.4 eV, intermediate of 2.8 eV, and large of 2 eV. For the determination of the bandgaps, the curves were plotted in a logarithmic scale. The band edges were then estimated to be the points where the dI/dV signal starts to deviate with respect to the noise level. These bandgap values are significantly larger than the energy bandgap of bulk Si (1.1 eV) and are well within the theoretical calculations for small amorphous and crystalline Si clusters.⁴¹

Lastly, we have investigated the stability of the Si arrays upon annealing to high temperatures. Figure 5a shows a large-scale STM image of a Si nanocluster array formed at 130 K and imaged at 300 K. Figure 5b is the corresponding FFT image with the well-defined moiré spots. The quasi-ordered arrays of Si nanoclusters are stable up to 577 K. Annealing of the clusters to 577 K has no apparent influence on their size, shape, density, and order; see the topography in Figure 5c and the corresponding FFT in Figure 5d. Annealing to higher

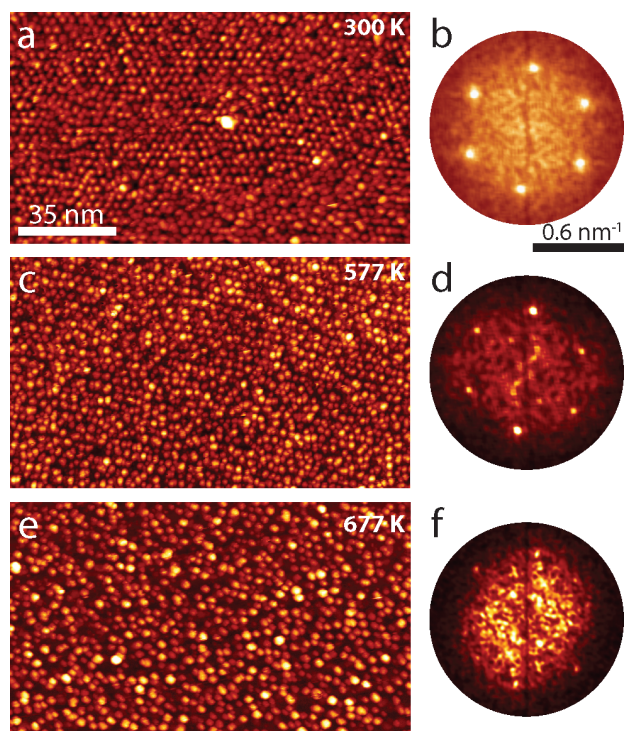


Figure 5. STM topographs and the corresponding FFT images of Si clusters formed on h-BN/Ir(111) by 0.4 ML Si deposition at 130 K. (a) The Si clusters were imaged at 300 K. (b) The corresponding FFT image of the STM image in (a). (c, d) STM image and the corresponding FFT after annealing to 577 K. (e, f) STM image and the corresponding FFT after annealing to 677 K. The image size in all panels is 130 nm \times 75 nm.

temperatures leads to degradation of the arrays. Figures 5e and 5f show the STM and its FFT after the sample was annealed 677 K. The clusters arrays have lost their order, apparent from the weakened moiré spots and the increase of the diffuse background near the center of the FFT image. Many larger clusters are found across the surface, suggesting cluster array degradation through coalescence. Metal cluster arrays on h-BN/Ir(111) and Gr/Ir(111) degrade also through cluster coalescence albeit at higher annealing temperatures.^{24,25,42}

CONCLUSIONS

The interaction of Si with the Ir(111) and the monolayer of h-BN on Ir(111) was investigated with scanning tunneling microscopy. Submonolayer amounts of Si form a surface alloy with the Ir(111) with a $(\sqrt{19} \times \sqrt{19}) R23^\circ$ reconstruction. Deposition of Si on monolayer h-BN on Ir(111) at 130 K leads to the growth of an imperfect Si cluster superlattice. The nanocluster superlattice remains stable up to annealing temperatures of 677 K. The h-BN monolayer effectively decouples the nanoclusters from the underlying Ir(111) substrate, allowing to measure their size-dependent electronic bandgap. Small clusters have a bandgap of 3.4 eV, which decreases with increasing the size of the cluster, reaching a value of 2 eV for large Si clusters. We have identified the preferred Si binding site to be the mesa regions of h-BN, which is in contrast to the metal and C clusters formed similarly on h-BN. Point defects at the h-BN mesas possibly cause Si to bind at these locations.

AUTHOR INFORMATION

Corresponding Author

Pantelis Bampoulis – II. Physikalisches Institut, Universität zu Köln, Cologne D-50937, Germany; Physics of Interfaces and Nanomaterials, MESA+ Institute for Nanotechnology, University of Twente, 7500 AE Enschede, The Netherlands; orcid.org/0000-0002-2347-5223; Email: p.bampoulis@utwente.nl

Authors

Tobias Hartl – II. Physikalisches Institut, Universität zu Köln, Cologne D-50937, Germany; orcid.org/0000-0002-3881-5462

Daniel Herrmann – II. Physikalisches Institut, Universität zu Köln, Cologne D-50937, Germany

Moritz Will – II. Physikalisches Institut, Universität zu Köln, Cologne D-50937, Germany; orcid.org/0000-0003-4822-9122

Yannic Falke – II. Physikalisches Institut, Universität zu Köln, Cologne D-50937, Germany

Alexander Grüneis – II. Physikalisches Institut, Universität zu Köln, Cologne D-50937, Germany; orcid.org/0000-0003-2448-6060

Thomas Michely – II. Physikalisches Institut, Universität zu Köln, Cologne D-50937, Germany

Complete contact information is available at: <https://pubs.acs.org/10.1021/acs.jpcc.2c00694>

Notes

The authors declare no competing financial interest.

ACKNOWLEDGMENTS

This work was funded by the Deutsche Forschungsgemeinschaft (DFG, German Research Foundation) within the project “Cluster Superlattice Membranes” (project no. 452340798). P.B. gratefully acknowledges financial support from the Alexander von Humboldt Foundation.

REFERENCES

- Alivisatos, A. P. Semiconductor Clusters, Nanocrystals, and Quantum Dots. *Science* **1996**, 271, 933–937.
- Heiz, U.; Landman, U. *Nanocatalysis*; Springer Science & Business Media: Heidelberg, 2007.
- Meiwes-Broer, K.-H. *Metal Clusters at Surfaces: Structure, Quantum Properties, Physical Chemistry*; Springer Science & Business Media: Heidelberg, 2000.
- N'Diaye, A. T.; Bleikamp, S.; Feibelman, P. J.; Michely, T. Two-Dimensional Ir Cluster Lattice on a Graphene Moiré on Ir(111). *Phys. Rev. Lett.* **2006**, 97, 215501.
- Angelova, P.; Vieker, H.; Weber, N.-E.; Matei, D.; Reimer, O.; Meier, I.; Kurasch, S.; Biskupek, J.; Lorbach, D.; Wunderlich, e. A.; et al. Katrin A Universal Scheme to Convert Aromatic Molecular Monolayers into Functional Carbon Nanomembranes. *ACS Nano* **2013**, 7, 6489–6497.
- Billinge, S. Materials Science: Nanoparticle Structures Served up on a Tray. *Nature* **2013**, 495, 453–454.
- Henry, C. R. 2D-Arrays of Nanoparticles as Model Catalysts. *Catal. Lett.* **2015**, 145, 731–749.
- Baltic, R.; Pivetta, M.; Donati, F.; Wäckerlin, C.; Singha, A.; Dreiser, J.; Rusponi, S.; Brune, H. Superlattice of Single Atom Magnets on Graphene. *Nano Lett.* **2016**, 16, 7610–7615.
- Shi, Q.; Gómez, D. E.; Dong, D.; Sikdar, D.; Fu, R.; Liu, Y.; Zhao, Y.; Smilgies, D.-M.; Cheng, W. 2D Freestanding Janus Gold Nanocrystal Superlattices. *Adv. Mater.* **2019**, 31, 1900989.

- (10) Will, M.; Bampoulis, P.; Hartl, T.; Valerius, P.; Michely, T. Conformal Embedding of Cluster Superlattices with Carbon. *ACS Appl. Mater. Interfaces* **2019**, *11*, 40524–40532.
- (11) Hartl, T.; Will, M.; Capeta, D.; Singh, R.; Scheinecker, D.; Boix de la Cruz, V.; Dellmann, S.; Lacovig, P.; Lizzit, S.; Senkovskiy, E. A.; Boris, V.; et al. Cluster Superlattice Membranes. *ACS Nano* **2020**, *14*, 13629–13637.
- (12) Fuechsle, M.; Mahapatra, S.; Zwanenburg, F. A.; Friesen, M.; Eriksson, M. A.; Simmons, M. Y. Spectroscopy of Few-electron Single-crystal Silicon Quantum Dots. *Nat. Nanotechnol.* **2010**, *5*, 502–505.
- (13) Stepina, N.; Zinov'eva, A.; Deryabin, A.; Zinov'ev, V.; Volodin, V.; Shklyayev, A.; Dvurechenskii, A.; Gaponenko, S. Formation and Structural Features of Silicon Quantum Dots in Germanium. *Optoelectron. Instrum. Data Process.* **2013**, *49*, 434–439.
- (14) Cheng, J.-Y.; Fisher, B. L.; Guisinger, N. P.; Lilley, C. M. Atomically Manufactured Nickel–Silicon Quantum Dots Displaying Robust Resonant Tunneling and Negative Differential Resistance. *npj Quantum Mater.* **2017**, *2*, 1–6.
- (15) Roland, C.; Meunier, V.; Larade, B.; Guo, H. Charge Transport Through Small Silicon Clusters. *Phys. Rev. B* **2002**, *66*, 035332.
- (16) Cullis, A.; Canham, L. Visible Light Emission Due to Quantum Size Effects in Highly Porous Crystalline Silicon. *Nature* **1991**, *353*, 335–338.
- (17) Trwoga, P.; Kenyon, A.; Pitt, C. Modeling the Contribution of Quantum Confinement to Luminescence from Silicon Nanoclusters. *J. Appl. Phys.* **1998**, *83*, 3789–3794.
- (18) Dasog, M.; De los Reyes, G. B.; Titova, L. V.; Hegmann, F. A.; Veinot, J. G. Size vs Surface: Tuning the Photoluminescence of Freestanding Silicon Nanocrystals Across the Visible Spectrum via Surface Groups. *ACS Nano* **2014**, *8*, 9636–9648.
- (19) Ledoux, G.; Guillois, O.; Porterat, D.; Reynaud, C.; Huisken, F.; Kohn, B.; Paillard, V. Photoluminescence Properties of Silicon Nanocrystals as a Function of their Size. *Phys. Rev. B* **2000**, *62*, 15942.
- (20) Evlyukhin, A. B.; Reinhardt, C.; Seidel, A.; Luk'yanchuk, B. S.; Chichkov, B. N. Optical Response Features of Si-nanoparticle Arrays. *Phys. Rev. B* **2010**, *82*, 045404.
- (21) Li, Q.; Jin, R. Photoluminescence from Colloidal Silicon Nanoparticles: Significant Effect of Surface. *Nanotechnol. Rev.* **2017**, *6*, 601–612.
- (22) Park, N.-M.; Kim, T.-S.; Park, S.-J. Band Gap Engineering of Amorphous Silicon Quantum Dots for Light-Emitting Diodes. *Appl. Phys. Lett.* **2001**, *78*, 2575–2577.
- (23) Whitham, K.; Yang, J.; Savitzky, B. H.; Kourkoutis, L. F.; Wise, F.; Hanrath, T. Charge Transport and Localization in Atomically Coherent Quantum Dot Solids. *Nat. Mater.* **2016**, *15*, 557–563.
- (24) Will, M.; Atodiresi, N.; Caciuc, V.; Valerius, P.; Herbig, C.; Michely, T. A Monolayer of Hexagonal Boron Nitride on Ir(111) as a Template for Cluster Superlattices. *ACS Nano* **2018**, *12*, 6871–6880.
- (25) Will, M.; Hartl, T.; Boix de la Cruz, V.; Lacovig, P.; Lizzit, S.; Knudsen, J.; Michely, T.; Bampoulis, P. Growth, Stability, and Electronic Decoupling of Pt Clusters on h-BN/Ir (111). *J. Phys. Chem. C* **2021**, *125*, 3880–3889.
- (26) Horcas, I.; Fernández, R.; Gómez-Rodríguez, J.; Colchero, J.; Gómez-Herrero, J.; Baro, A. WSXM: A Software for Scanning Probe Microscopy and a Tool for Nanotechnology. *Rev. Sci. Instrum.* **2007**, *78*, 013705.
- (27) Diebold, U.; Zhang, L.; Anderson, J. F.; Mrozek, P. Surface Segregation of Silicon in Platinum (111). *J. Vac. Sci. Technol.* **1996**, *14*, 1679–1683.
- (28) Švec, M.; Hapala, P.; Ondráček, M.; Merino, P.; Blanco-Rey, M.; Mutombo, P.; Vondráček, M.; Polyak, Y.; Cháb, V.; Gago, E. A.; et al. JA Martin Silicene Versus Two-dimensional Ordered Silicide: Atomic and Electronic Structure of Si-(19×19) R 23.4°/Pt (111). *Phys. Rev. B* **2014**, *89*, 201412.
- (29) Satta, M.; Lacovig, P.; Apostol, N.; Dalmiglio, M.; Orlando, F.; Bignardi, L.; Bana, H.; Travaglia, E.; Baraldi, A.; Lizzit, S.; Larciprete, R. The Adsorption of Silicon on an Iridium Surface Ruling out Silicene Growth. *Nanoscale* **2018**, *10*, 7085–7094.
- (30) Farwick zum Hagen, F. H.; Zimmermann, D. M.; Silva, C. C.; Schlueter, C.; Atodiresi, N.; Jolie, W.; Martínez-Galera, A. J.; Dombrowski, D.; Schroder, U. A.; et al. Moritz Structure and Growth of Hexagonal Boron Nitride on Ir (111). *ACS Nano* **2016**, *10*, 11012–11026.
- (31) Martínez-Galera, A. J.; Gómez-Rodríguez, J. M. Pseudo-ordered Distribution of Ir Nanocrystals on h-BN. *Nanoscale* **2019**, *11*, 2317–2325.
- (32) Düll, F.; Meusel, M.; Späth, F.; Schötz, S.; Bauer, U.; Bachmann, P.; Steinhauer, J.; Steinrück, H.-P.; Bayer, A.; Papp, C. Growth and Stability of Pt Nanoclusters from 1 to 50 atoms on h-BN/Rh (111). *Phys. Chem. Chem. Phys.* **2019**, *21*, 21287–21295.
- (33) N'Diaye, A. T.; Gerber, T.; Busse, C.; Mysliveček, J.; Coraux, J.; Michely, T. A Versatile Fabrication Method for Cluster Superlattices. *New J. Phys.* **2009**, *11*, 103045.
- (34) Herbig, C.; Knispel, T.; Simon, S.; Schröder, U. A.; Martínez-Galera, A. J.; Arman, M. A.; Teichert, C.; Knudsen, J.; Krashennnikov, A. V.; Michely, T. From Permeation to Cluster Arrays: Graphene on Ir(111) Exposed to Carbon Vapor. *Nano Lett.* **2017**, *17*, 3105–3112.
- (35) Lamb, L. D.; Huffman, D. R.; Workman, R. K.; Howells, S.; Chen, T.; Sarid, D.; Ziolo, R. F. Extraction and STM Imaging of Spherical Giant Fullerenes. *Science* **1992**, *255*, 1413–1416.
- (36) Mararov, V. V.; Gruznev, D. V.; Bondarenko, L. V.; Tupchaya, A. Y.; Zotov, A. V.; Saranin, A. A. Comparative STM Analysis of C60 and C70 Fullerene Adsorption Sites on Pristine and Al-modified Si (111) 7×7 Surfaces. *J. Vac. Sci. Technol.* **2016**, *34*, 061402.
- (37) Pawlak, R.; Glatzel, T.; Pichot, V.; Schmidlin, L.; Kawai, S.; Frey, S.; Spitzer, D.; Meyer, E. Local Detection of Nitrogen-Vacancy Centers in a Nanodiamond Monolayer. *Nano Lett.* **2013**, *13*, 5803–5807.
- (38) Röthlisberger, U.; Andreoni, W.; Parrinello, M. Structure of Nanoscale Silicon Clusters. *Phys. Rev. Lett.* **1994**, *72*, 665.
- (39) Ho, K.-M.; Shvartsburg, A. A.; Pan, B.; Lu, Z.-Y.; Wang, C.-Z.; Wacker, J. G.; Fye, J. L.; Jarrold, M. F. Structures of Medium-sized Silicon Clusters. *Nature* **1998**, *392*, 582–585.
- (40) Yoo, S.; Shao, N.; Zeng, X. C. Structures and Relative Stability of Medium-and Large-sized Silicon Clusters. VI. Fullerene Cage Motifs for Low-lying Clusters Si₃₉, Si₄₀, Si₅₀, Si₆₀, Si₇₀, and Si₈₀. *J. Chem. Phys.* **2008**, *128*, 104316.
- (41) Allan, G.; Delerue, C.; Lannoo, M. Electronic Structure of Amorphous Silicon Nanoclusters. *Phys. Rev. Lett.* **1997**, *78*, 3161.
- (42) Gerber, T.; Knudsen, J.; Feibelman, P. J.; Granas, E.; Stratmann, P.; Schulte, K.; Andersen, J. N.; Michely, T. CO-Induced Smoluchowski Ripening of Pt Cluster Arrays on the Graphene/Ir(111) Moiré. *ACS Nano* **2013**, *7*, 2020–2031.

6 Transfer Methods for Cluster Superlattice Membranes

6.1 Introduction

The emergence of two-dimensional (2D) materials has revolutionized the field of materials science, offering extraordinary properties and promising prospects for a wide range of technological applications [156]. Graphene, the pioneering 2D material, ignited tremendous interest due to its exceptional electrical, thermal, and mechanical properties [157]. However, researchers soon realized that the realm of 2D materials extends far beyond graphene. A diverse family of 2D materials, including transition metal dichalcogenides (TMDs), hexagonal boron nitride (h-BN), phosphorene, and their respective van der Waals heterostructures, have since been discovered, each with their own unique set of properties and exciting potential [158–161].

While the synthesis and characterization of 2D materials have witnessed substantial progress, the successful integration of these materials into practical devices remains a significant challenge [162]. One critical aspect that demands attention is the transfer of 2D materials from their growth substrate onto desired substrates or device platforms. The transfer process not only affects the quality, stability, and uniformity of the transferred material but also determines its compatibility with specific applications [163].

The transfer of 2D materials involves delicately separating the material from its original substrate and placing it onto a target substrate or device while preserving its structural integrity and desired properties. This seemingly straightforward task presents a host of technical hurdles due to the extreme fragility and vulnerability of 2D materials to environmental factors, as well as the need for precise alignment and controlled adhesion [164–166].

Cluster superlattice membranes (CSLMs) represent a unique class of heterogeneous 2D materials, characterized by one side composed of an amorphous carbon layer, and the other side featuring a cluster superlattice encapsulated by a templating layer of graphene or h-BN [135]. Both the process of separating CSLMs from their growth substrate and their subsequent han-

dling require specialized procedures to ensure the preservation of membrane integrity and proper orientation upon transfer to the desired substrate. This chapter aims to provide a comprehensive overview of the transfer methods specifically developed and employed for CSLMs, offering a practical guide encompassing the preparation techniques and crucial steps involved in the processing of this intriguing material.

6.2 Experimental Methods

Shadow masks with different hole sizes and geometries were manufactured by the in-house mechanical workshop. Polydimethylsiloxan (PDMS) is acquired from Gel-Pak and the GEL-FILM PF-60-X4 and PF-60-X0 are used. Polymethylmethacrylat (PMMA) was bought from Allresist as AR 300-12. Trichlormethane and 1 Mol NaOH solution are sourced from Carl Roth. Power is supplied via a Keithley 2200-20-5.

A commercially available 2D heterostructure transfer system, consisting of an optical microscope mounted above a temperature controlled sample platform and stamping stage with multiple micro-manipulators from HQ Graphene was placed inside a laminar flow box to ensure clean working conditions. For additional manual preparations, manual steps and characterization a stereo microscope was also placed in the same laminar flow box.

6.3 Modified Bubbling Transfer Method

One major development in the transfer process was a step away from the traditional hydrogen bubbling method applied in [135]. In the traditional approach the 2D material is coated with a supporting polymer layer (e.g. PMMA) and then removed from the substrate together with the polymer layer in an electrochemical cell. The growth substrate (in our case Ir(111)) with the 2D material is submerged in a NaOH solution (typically 1 Mol/L) and put on a negative potential of minimum ~ 1.5 V. A Pt foil acts as the anode. The reactions taking place are as follows:

Cathode:



Anode:



The evolution of gases happens at the interface of the electrodes and, in the case of the Ir, the edges of the 2D material, slowly splitting it off from the crystal. After the material is fully delaminated it floats up in the solution, supported by the polymer layer, from where it can be picked up and processed further.

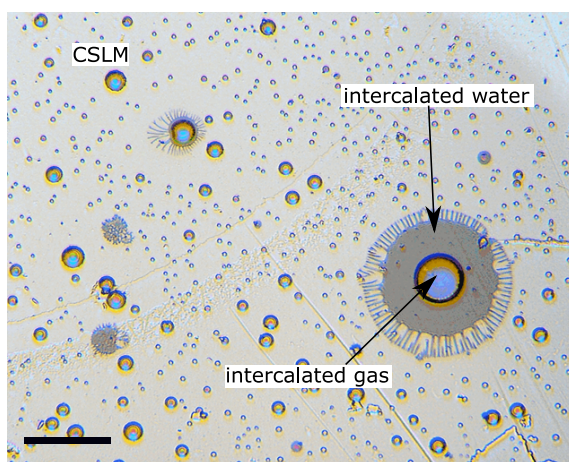


Figure 6.1: Optical microscope image of a cluster superlattice membrane on Ir(111) in 1 mol NaOH solution on a 1.65 V potential. The arrows point out the areas of gas and fluid intercalation as well as the accompanying contrast change. The scale bar is 100 μm .

While this process is used successfully for the delamination and transfer of many 2D materials, it relies on the polymer to support it throughout the process [167–169]. In our modified approach the Ir(111) crystal is placed in the NaOH solution without any polymer supporting the 2D material. Intentionally keeping the bubbling process slow and controlled can lead to the intercalation of the membrane with gaseous H_2 or liquid H_2O without detachment of the membrane itself. The process is observed via optical microscopy, where the intercalated areas are easily visible (see Figure 6.1). Membranes intercalated this way can then be picked up by the stamping methods described later in this chapter. It is important to perform the stamping in a timely manner after the Ir crystal is removed from the solution, as the water drying out below the membrane will lead to its firm reattachment to the Ir substrate. Our experiments have shown that only membranes intercalated by either water or gas can be removed via stamping, making the large scale intercalation of the 2D material vital to the success of this method. A number of factors that influence the intercalation are discussed in the following.

6.4 Effects of CSLM Preparation

Following the growth of the cluster superlattice (as described in Chapter 3), various preparation methods can be employed, impacting the subsequent intercalation process of the membranes. These factors include the size of the membranes, the thickness of the carbon layer, oxygen etching of the sample, and post-annealing of the membrane. The optimization of these parameters plays a crucial role in determining the efficiency and outcome of the delamination process.

Both oxygen etching and annealing should, in principle, enable an easier separation of the membrane from the substrate. While in situ oxygen etching removes the templating layer in between the carbon covered regions of the sample and thus enable easier intercalation of H_2O from the side of the membranes, the number of prepared samples was not large enough to make a strong statement about the effectiveness of this method. Due to it being non destructive to the actual membrane however, it was applied in the fabrication of most samples. Annealing has been shown to reduce the binding between the templating layer and the substrate and is a crucial step in the fabrication of the cluster superlattice membranes, as not annealed membranes were not able to be delaminated from the substrate [135]. Another possible approach to explore at this step is the pre-intercalation of Gr with species which lower the binding between Gr and the Ir(111) substrate. Earlier studies have found Cs to easily intercalate Gr and assist in the transfer of large areas of Gr [170, 171]. In our experiments Eu intercalation at 750 K was attempted, but neither the full intercalation of the membranes, nor an effect on the transfer process could be confirmed.

The influence of membrane diameter on the H_2O intercalation has been investigated on a sample with a multitude of different sized membrane spots. A mask with holes of diameters 0.3 mm, 0.5 mm, 1 mm, 1.5 mm and 2 mm was used to grow accordingly sized membranes on an Ir(111) substrate. The resulting sample was placed in 1 mol NaOH solution at a voltage of 1.65 V and monitored with an optical microscope (see Figure 6.2 (a)). As visible in Figure 6.2 (b), after multiple hours in the solution, the intercalation starts from the outside edge of the membranes. Figure 6.2 (c) shows intercalation happening from a single spot in the middle of the 1 mm membrane and Figure 6.2 (d) the fully intercalated membrane. The intercalation of the largest (2 mm) starts shortly after and begins with a small area on the bottom right (Figure 6.2 (e)) and proceeds from there through the whole membrane (Figure 6.2 (f)). Further gas production then leads to the membrane forming a volcano like dome on the substrate (Figure 6.2 (g)). Only after this, intercalation of the other membranes takes place (Figure 6.2 (h)). A continuous bubbling then leads to the rupture of the membranes after enough gas has been produced (Figure 6.2 (i)). The intercalation of the membranes (safe for the 1 mm begins at the edges and

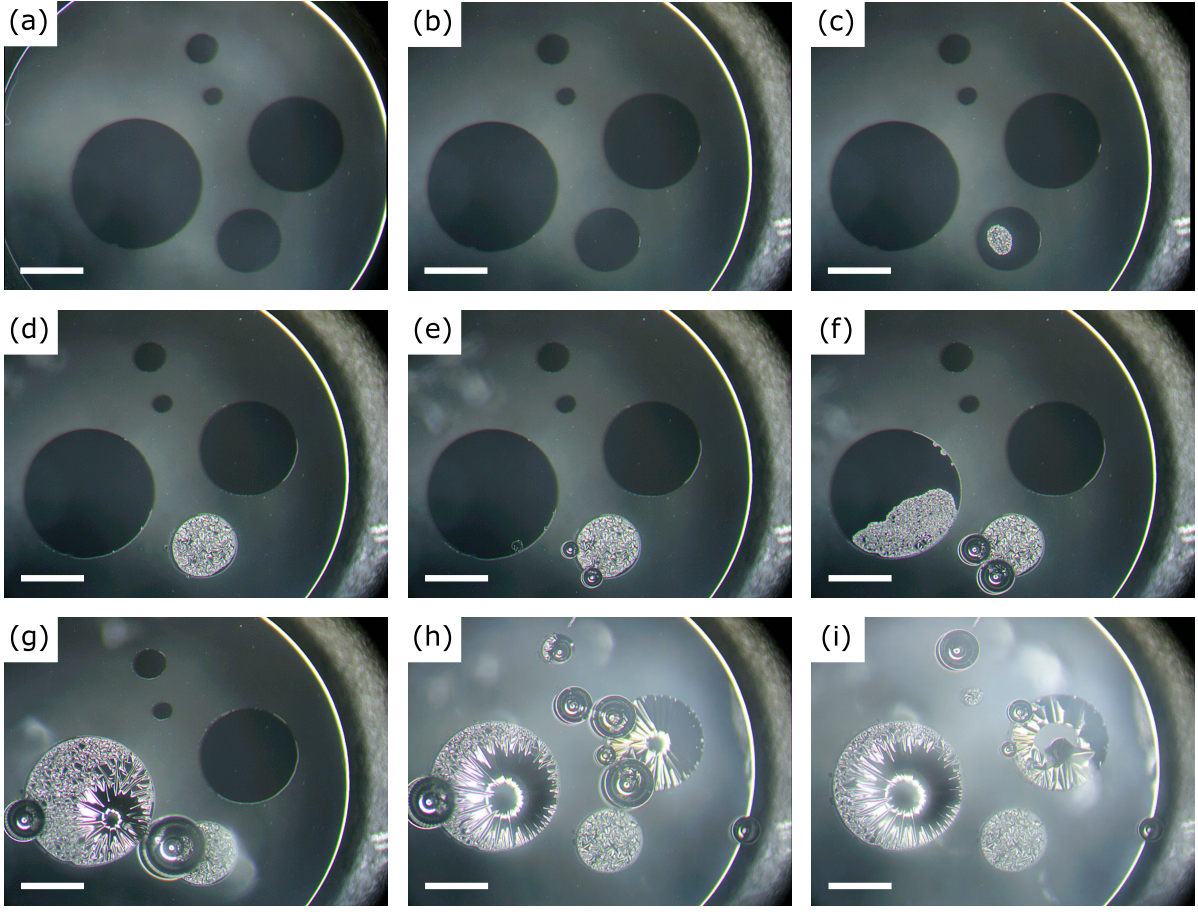


Figure 6.2: Optical microscope image of cluster superlattice membranes of different sizes and a a-C thickness of around 50 ML on a Ir(111) crystal in 1 mol NaOH solution on a 1.65 V potential. The membrane disks have a diameter of 0.3 mm, 0.5 mm, 1 mm, 1.5 mm and 2 mm. The scale bar is 1 mm in all images.

this mechanism would indicate a faster total intercalation of smaller membranes, however after repeated experiments there is no evidence of a correlation of size and successful intercalation of the membranes. To ensure large membranes as well as a high enough number of successes a mask with 19 0.8 mm holes in a hexagonal pattern was used in further experiments.

A second important factor in the fabrication of the membranes is the thickness of the carbon membranes. In experiments, membranes with around 5 ML C, 10 ML C and > 50 ML C were tested. Figure 6.3 shows the intercalation of a 5 ML C membrane. It is visible that the intercalation starts from the edge as well as multiple points in the middle of the membrane. As the intercalation progresses the membrane progresses small ruptured areas become apparent (Figure 6.3 (b)). Gas that is produced in the electrolysis in these areas escapes and no further

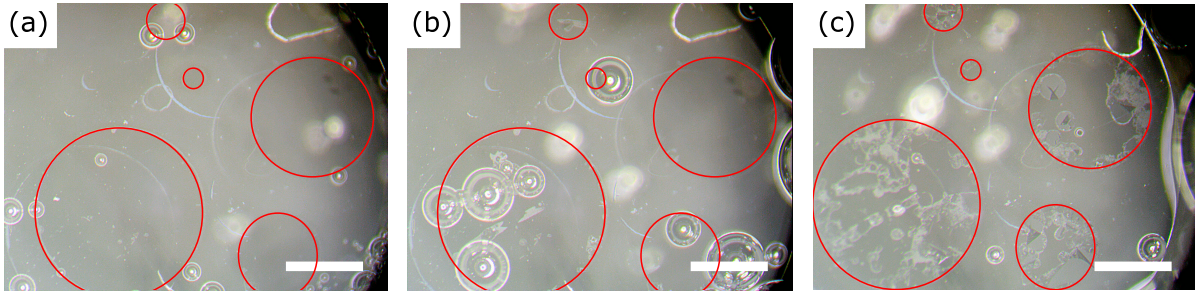


Figure 6.3: Optical microscope image of cluster superlattice membranes of different sizes and a a-C thickness of around 5 ML on a Ir(111) crystal in 1 mol NaOH solution on a 1.65 V potential. The membrane disks have a diameter of 0.3 mm, 0.5 mm, 1 mm, 1.5 mm and 2 mm and are highlighted by red circles. The scale bar is 1 mm in all images.

intercalation can be observed. This leads to small areas of intercalated membrane separated by completely unintercalated areas (Figure 6.3 (c)).

In comparison, thicker membranes show fewer signs of intercalation starting in the middle of the membrane, are less prone to rupturing and easier to fully intercalate. In fact, the 50 ML C membranes can be seen to form large bubble like structures above the substrate. It is not possible to completely detach the membranes from the substrate via gas pressure as all observed membranes ruptured before detaching (Figure 6.2 (i)). The intercalated membranes show a web-like structure when still on the substrate and a dome or volcano like shape when intercalated with a large gas volume. Both deformations indicate strain present in the membrane as the equilibrium shape would be either flat when on the substrate or half dome like when intercalated by gas.

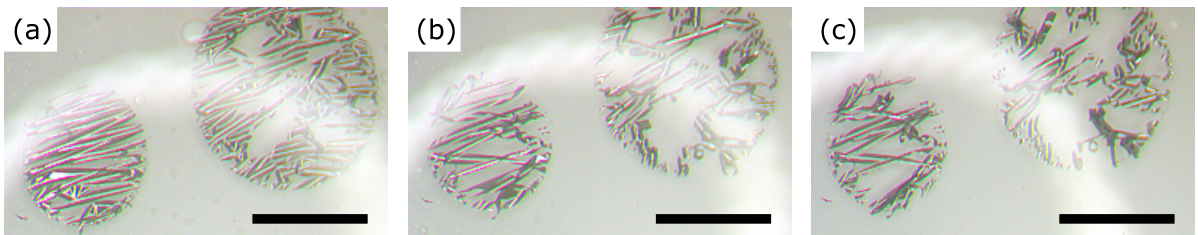


Figure 6.4: Optical microscope image of cluster superlattice membranes of different sizes and a a-C thickness of around 50 ML on PDMS. The membrane disks have a diameter of 1 mm and 1.5 mm. The scale bar is 1 mm in all images.

After detachment from the substrate the behaviour of thin and thick membranes also differs. While thin membranes attach very well to the polymer supports, the thick membranes curl up on themselves (see Figure 6.4). This curling behaviour has also been observed after transfer to

a new substrate and limits the applicability of thick carbon membranes. Both, the curling after detaching and the "volcano shape" on the substrate, can be explained with a high amount of tensile stress on the upper side of the amorphous carbon matrix. In practice membranes with a thickness of around 10 to 20 ML C have shown to offer a good compromise between large intercalated areas and low stress related curling. It might be possible to reduce the stress in the a-C matrix by embedding at elevated temperatures, or incorporation of other species into the a-C matrix to relieve the stress.

6.5 Simple Carbon Side up Transfer

The simplest possible transfer is a transfer of the CSLM to a new substrate without the necessity to rotate it. Such a transfer can be employed when the direction the membrane is either not of relevance, for example in sample preparation for transmission electron microscopy, or when access to the a-C side is actually wanted. After successfully intercalating the membranes on the Ir(111) substrate, any kind of polymer tested was able to pick up the membrane. The challenge was to find which polymer provides a clean release once the membranes are supported on the new substrate. A quick way to achieve this is by picking the membrane up with PDMS and stamping it to a new substrate. While placing the PDMS on the desired membrane area it is important to ensure no air is encapsulated. Heating during this step is to be avoided, as it can lead to the CSLM attaching strongly to the Ir(111) substrate again. PDMS is viscoelastic and as such the peeling speed will influence the adhesiveness between itself and the CSLM [172, 173]. Removal of the PDMS should be performed in one swift movement to ensure the best outcome.

After the removal from the substrate, the CSLM should be well attached to the PDMS. Washing with de-ionized water is possible at this point in time without significant loss of 2D material. Afterwards the PDMS/CSLM is stamped onto the target substrate. Immediate removal of the PDMS at this stage will lead to suboptimal outcomes. Before removing the PDMS the attachment of the CSLM to the new substrate can be improved by heating to 100 °C for 5 min. Vacuum annealing to 200 °C has also been found to reduce stress in 2D materials and removes interfacial bubbles [173]. Before the removal of the PDMS it is important to let it cool down to room temperature again. The PDMS is then removed as slowly as possible using a micromanipulator [174]. Rates of 10 µm per second have been found to produce satisfying results.

6.6 Turn-over Transfer

In order to transfer a membrane to a substrate with the Gr side facing the environment, it is necessary to provide temporary support using a second layer as depicted in Figure 6.5. It is crucial to remove the initial polymer support without damaging the second layer and ideally achieve a high yield of transferred membrane. One potential approach to accomplish this is through selective chemical etching. For instance, the membrane can be sandwiched between PMMA and a thin copper foil. If the membrane adheres well to the copper, it is theoretically possible to eliminate the PMMA using acetone. Subsequently, after placing the foil and membrane on a new substrate, the foil can be removed using ferric chloride. However, this process tends to result in significant residue and relies on the attachment of the membrane to the copper foil and the subsequent substrate, and has not been successfully implemented thus far.

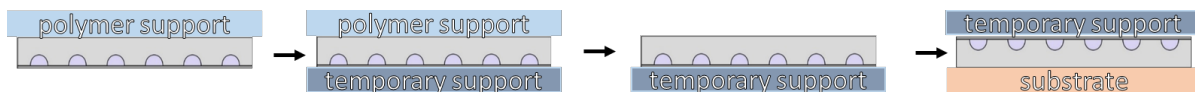


Figure 6.5: General sketch of the turn-over transfer using a first polymer layer to remove the membrane from the substrate and a second temporary layer to support the membrane during the turnover process.

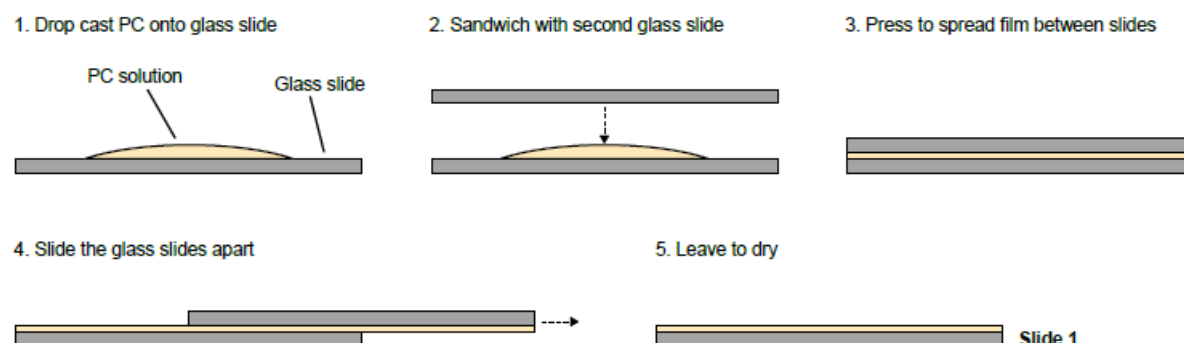
An alternative to etching removal of support layers is a mechanical route in which the membrane is stamped from less adhesive polymers to more adhesive polymers. As PDMS can be bought in varying degrees of adhesiveness and offers a generally residue free transfer it is the ideal starting process for this double transfer route. Starting with the lowest available adhesion grade and stamping it with a higher adhesion grade PDMS, it is possible to transfer and turn around small areas of CSLM. The higher the adhesion of the second stamping polymer, the more material can be removed from the original PDMS layer. While being clean and quick, the downsides of this procedure are losses of transferred area in the first step, as well as need for a higher grade of adhesion, that also lowers the amount of transferable membrane to the target substrate as it has to be released from the PDMS later. To avoid the troublesome mechanical release of the CSLM from PDMS, a highly adhesive and easily solvable polymer is the ideal choice for a second support layer.

Polycarbonate (PC) possesses a high adhesion to 2D materials, can be removed via trichlormethane, and is easily assembled in thin layers as a stamp [174–176]. The assembly steps from Ref. [174], depicted in Figure 6.6 were followed to produce a transparent stamp, which can be used to transfer close to 100% of CSLM from PDMS onto PC.

To start the process, the PC stamp is pressed onto the PDMS layer in areas containing the CSLM and heated to 130°C to soften the polymer layers. This improves adhesion between 2D material and the PC and allows any air bubbles to escape from between the layers. Once both layers are in contact there is a stark contrast change of the CSLM observed under the optical microscope, going from bright and reflective to dark gray (see Figure 6.7 (a) and (b)). Carefully applied pressure can aid the release of air bubbles. When the desired area is firmly attached and no bubbles are present the stack is cooled down to room temperature again, as the adhesion of PC is lowered at elevated temperatures. Afterwards the PC stamp needs to be removed slowly from the PDMS layer via micromanipulators.

To finalize the turn-over process this stamp is then pressed onto the target substrate and heated to 200°C for multiple minutes. At this temperature the PC melts and, together with the CSLM, firmly attaches to the target substrate. The stamp can then be removed carefully, so as not to smear the remaining PC layer. Afterwards the sample is cooled down to room temperature (see Figure 6.7 (c)). The PC layer can later be removed by washing the sample with trichlormethane. To ensure maximum adhesion of CSLM to the substrate it is important to perform the first washing step carefully by slowly lowering the sample into trichlormethane at a slight angle. Once the first washing step is completed, the trichlormethane/PC solution is removed and fresh trichlormethane is used to further wash the sample. This step can be repeated as often as deemed necessary to remove the last residues of PC on the sample. Finally the sample is rinsed in deionized water. The final result of a successful turn-over transfer can be seen in Figure 6.8, which shows multiple large areas of transferred CSLM on Ir(111) with the Gr exposed to the environment.

Prepare PC Film



Transfer PC onto PDMS

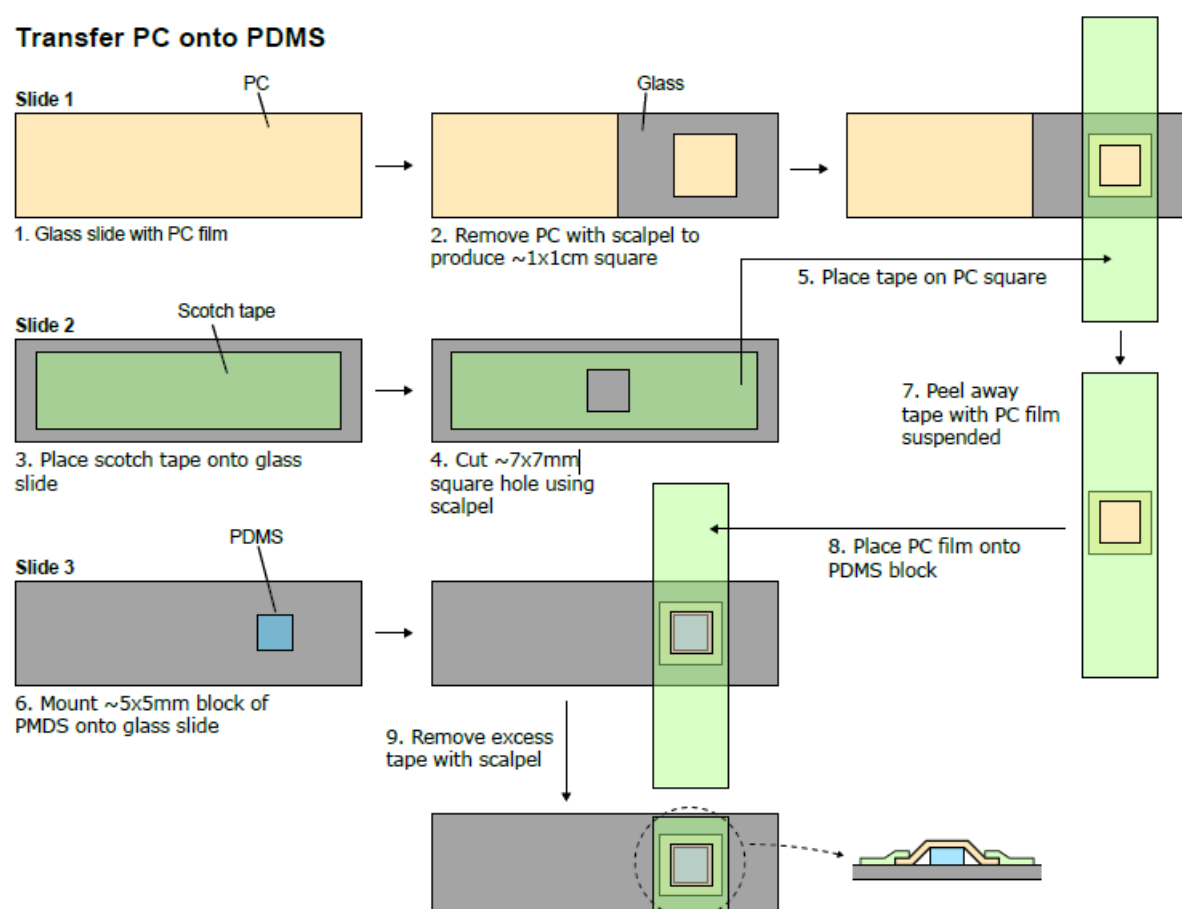


Figure 6.6: Preparation of the polycarbonate stamp. The polycarbonate (PC) solution is prepared by dissolving 5% by weight polycarbonate in chloroform. The method for preparing the transfer stamp is outlined in the figure. The PC is drop cast onto a glass slide using a pipette (typically 5 drops) and a second slide is then used to sandwich and spread the solution between the two slides. The slides are immediately slid apart, and left to allow the chloroform to evaporate. Excess PC is then removed by a scalpel to define a 1×1 cm square of PC. A window is cut into a piece of scotch tape, which is then used to pick up the PC from the glass slide. The tape is then used to place the PC onto a block of PDMS, and excess tape is removed again using a scalpel. For the completed stamp, the PC is held in place on the PDMS by the scotch tape. Adapted from Ref [174]. Copyright 2018 Springer Nature.

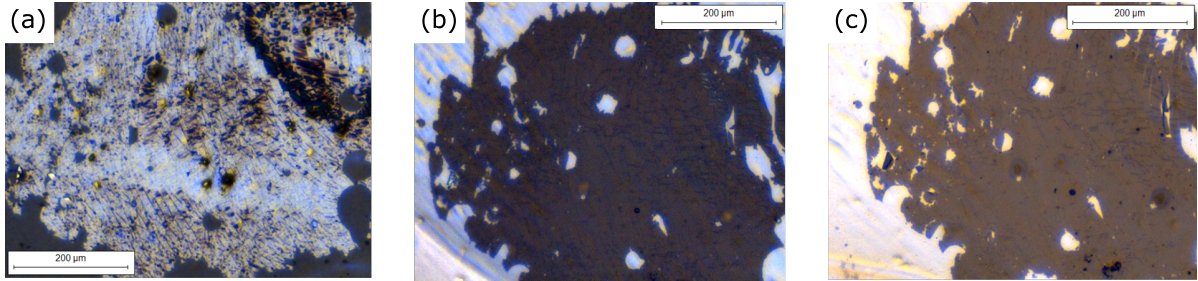


Figure 6.7: Optical microscope image of the same area of CSLM during different stages of the double transfer. (a) CSLM on PDMS, (b) CSLM sandwiched between PDMS and PC, (c) CSLM on Au covered by PC.

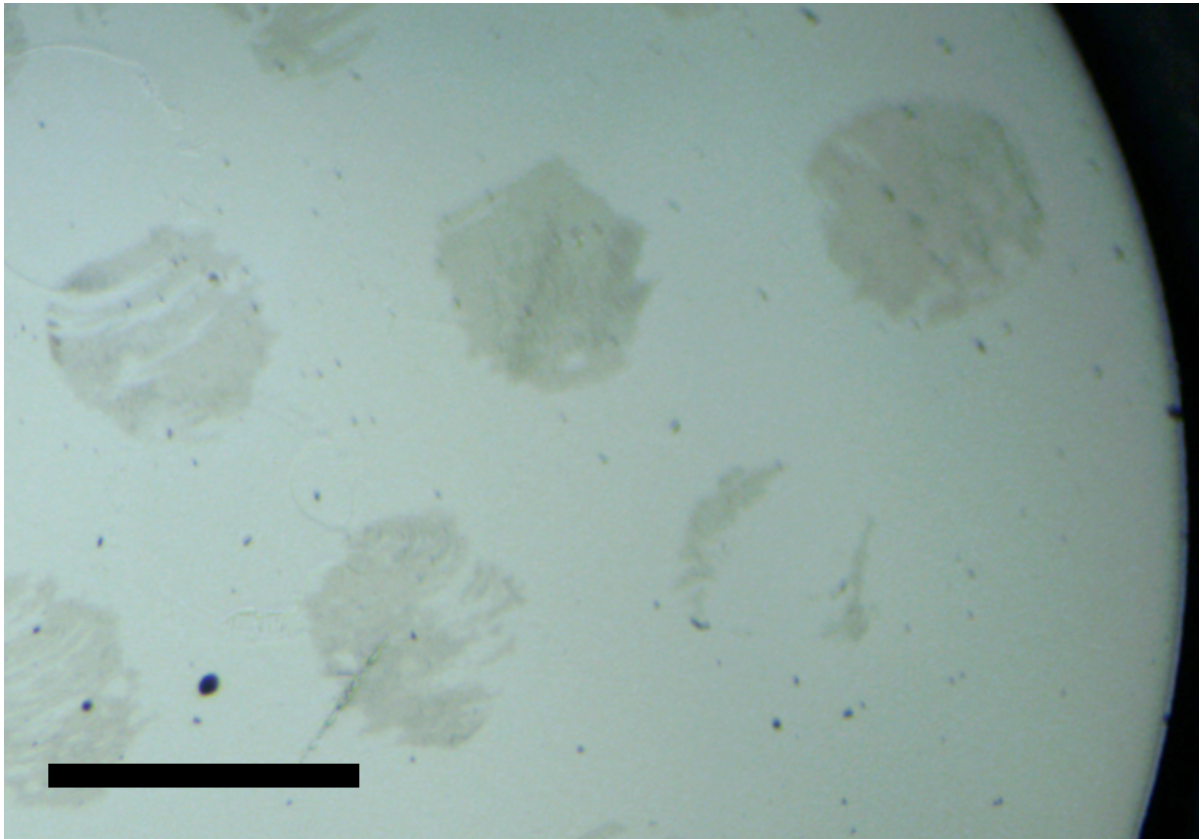


Figure 6.8: Optical microscope image of CSLMs on Ir(111) after the turnover process (graphene side facing the environment). The scale bar is 1 mm.

6.7 Conclusion and Outlook

A multitude of different transfer processes have been tested and developed to gain control over the orientation of CSLMs, transfer large areas and achieve clean transfers to arbitrary new substrates. PDMS has been shown to be highly versatile in its application due to its viscoelastic properties, commercial availability in different levels of adhesiveness and cleanliness during the handling.

PC stamps are producible by hand and offer a great basis for the turn-over process. Changes in temperature are able to soften it to provide better attachment to the membranes and later on to the final substrate.

While the intercalation of the membranes on the Ir(111) has been identified as the core step in the transfer of CSLMs it is also the most variable step, depending on factors not yet entirely understood. The preparation of the membrane, including thickness of the C layer, shape and size of the membrane spots, O etching and alkali metal intercalation, the quality of the substrate, the temperature of the intercalation fluid, the applied voltage and time all may play roles in the process of intercalating the membranes. The levels of involvement of each of the parameters would have to be further studied in a series of controlled experiments. The large parameter space and required time to prepare even single samples makes it infeasible to investigate the ins and outs of this process in this work as a sufficient set up has been found.

7 Functionalization of Fe–Pt Cluster Superlattice Membranes via O Radical Etching

7.1 Introduction

The field of heterogeneous 2D material structures is advancing rapidly, driven by the desire to harness their diverse physicochemical properties for tailored applications [156, 177, 178]. Cluster superlattice membranes (CSLMs) are a novel class of hybrid 2D materials, consisting of a templating layer - graphene or hexagonal boron-nitride - hosting a hexagonal nanocluster array, sandwiched by a stabilizing matrix. They present numerous opportunities for customization, with tunable cluster material and size, spacing, and choice of embedding material [100, 126, 135]. Fe–Pt clusters hosted in an a-C matrix represent an especially intriguing combination. The interplay between Pt and Fe atoms in the clusters results in increased catalytic activity and durability [179–183]. Additionally, Fe–Pt clusters in the L1₀ phase display enhanced magnetic properties, such as superparamagnetic behaviour and a large magnetic anisotropy [155, 184–188]. These properties make Fe–Pt clusters in CSLMs strong candidates for high-density magnetic recording media or research into dipole dipole interactions [154].

In order to fully harness the capabilities of CSLMs it is imperative that full control over the fabrication and handling process is established. Furthermore, the predicted properties, such as blockage of gas diffusion and catalytic activity after removal of the templating layer require experimental confirmation. Fe–Pt based membranes provide a useful fingerprint system for both of these categories. If the membrane successfully blocks the diffusion of oxygen, the Fe atoms should remain unoxidized after exposure to ambient conditions or atomic oxygen. Conversely, if the membrane can be reopened in a controlled manner, the Fe atoms should oxidize after exposure to oxygen. These tests not only confirm the predicted properties of the CSLMs but also serve as a means to optimize their performance for various applications.

In this chapter we report the successful transfer of a Fe–Pt based CSLM onto a new substrate,

confirm the membrane to be impenetrable to oxygen, and show a controllable way of reopening the CSLM.

7.2 Experimental Methods

STM was performed in the UHV system Athene in Cologne, Germany. XPS data were measured at the FlexPES beamline of MAX IV in Lund, Sweden. The base pressure in both systems is in the 1×10^{-11} mbar range for both systems. Ir(111) samples were prepared in situ by cycles of noble gas ion sputtering followed by flash annealing to 1420 K. Graphene was grown in a two step process: First the sample is exposed to 1×10^{-6} mbar ethene (C_2H_4) for 20 s and then flashed to 1300 K. Once the temperature is reached the sample is kept at 1300 K and exposed to 2×10^{-7} mbar ethene for 600 s before cooling down in UHV. Low-energy electron diffraction was used in Cologne and Lund to confirm a well ordered graphene layer.

Fe–Pt cluster superlattices are prepared on Gr via sequential deposition of Pt from an e-Beam evaporator and Fe from a Knudsen cell at 1400 K. To improve the ordering the sample was cooled down to 250 K in Cologne. Deposition rates were calibrated via the islands of Fe and Pt formed on Ir(111) measured by STM in Cologne and via the respective core level (Fe 2p, Pt 4d) in comparison to the Ir 4d core level in Lund.

XANES spectra were measured in the total electron yield configuration. The energy was calibrated via the binding energy of the C 1s core level.

STM was conducted at room temperature with tunneling currents in the order of $I = 0.5$ nA.

Transfer and turn-over of the Fe–Pt CSLM from one Ir(111) substrate to another followed a home-developed process, described in Chapter 6, consisting of the intercalation of H_2O below the membrane, followed by a lift off from the original Ir(111) substrate via polydimethylsiloxane (PDMS)-stamp, a second stamping with a polycarbonate (PC) stamp, and finally the transfer to a new Ir(111) substrate.

7.3 Results and Discussion

Figure 7.1 (a) shows an STM topograph of a cluster superlattice made up of 0.3 ML Fe deposited at 250 K onto 0.3 ML Pt cluster seeds on Gr/Ir(111). This seeding method gives the clusters a long range order as well as a filling of the moiré cells of around 91%, far surpassing that of pure Fe clusters on Gr/Ir(111) [100]. Figure 7.1 (b) shows the XA spectra of a sample prepared at

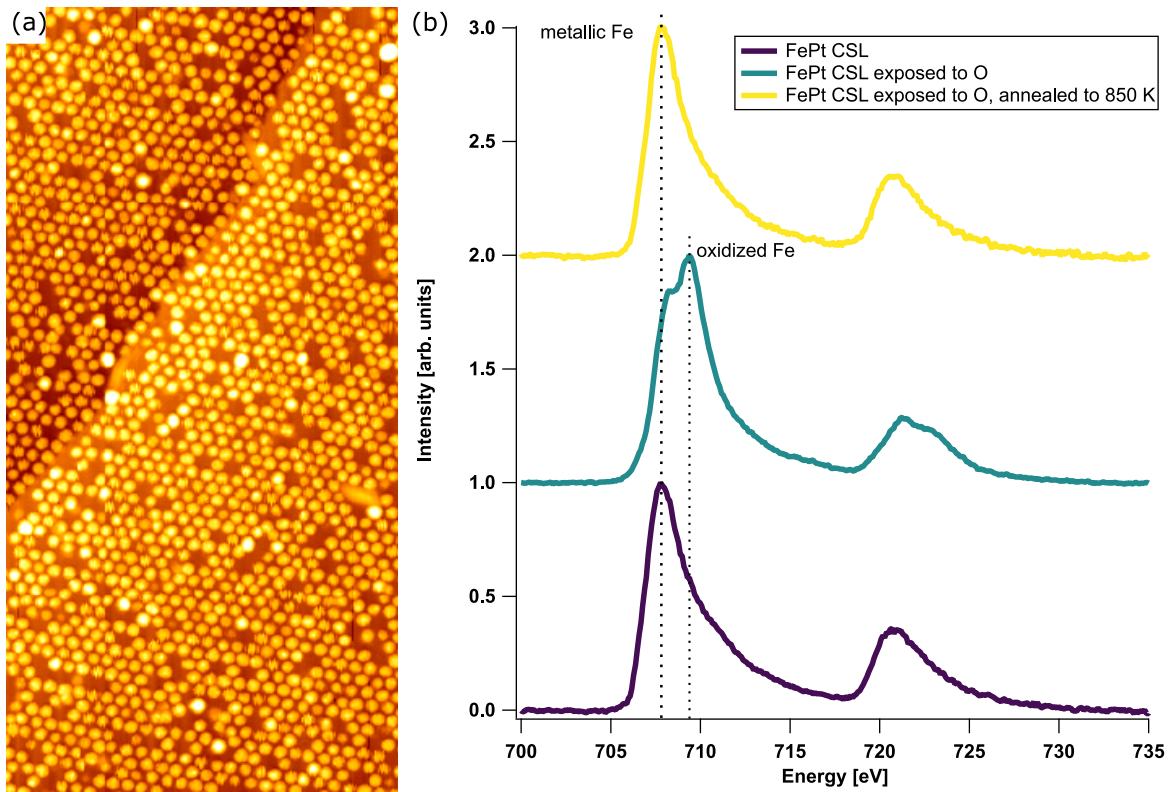


Figure 7.1: (a) STM topography of a 0.3 ML Fe + 0.3 ML Pt cluster superlattice on Gr/Ir(111). Scale is 150×75 nm. (b) XA spectra at the Fe $L_{3,2}$ edges, taken at RT. Spectra of a 0.3 ML Fe + 0.3 ML Pt cluster superlattice on Gr/Ir(111) in rising order: after degassing, after exposure to atomic O, after O exposure and annealing to 850 K.

MAX IV via 0.3 ML Pt seeding + 0.3 ML Fe deposition. The lowest (purple) spectrum shows the Fe $L_{3,2}$ edges in their initial state. A clear single peak at 708 eV can be identified, which is attributed to metallic Fe in accordance with literature (compare Ref. [189, 190]). No sign of oxidation is visible in the signal and we conclude that this is the initial state of mixed Fe–Pt clusters. Upon exposure to 100 L of atomic oxygen and 1000 L molecular oxygen (middle - turquoise - spectrum) the signal now has shifted to slightly higher energies and developed a clear double peak structure at 709.5 eV representative of oxidized Fe [189, 191]. After annealing the sample at 850 K for 30 s without supplying additional oxygen the signal returns to its original shape and position at 708 eV. While the oxidation of Fe is a natural reaction to O exposure, the mechanism of reverting back to the unoxidised state is not clear. One possibility is, that the Fe–Pt clusters intercalate the graphene layer [132] and form a surface alloy with the Ir substrate, losing the O in the process [192]. Another way to reduce Fe oxides is via a catalytic reaction. Fe_2O_3 clusters have been found to be able to supply their own oxygen towards the oxygenation of CO molecules [193, 194]. Fe–Pt nano particles have also been found to be active towards CO oxidation [180]. Together with O adsorbed on the graphene the clusters could break FeO bonds to form CO_2 , etch the graphene and, in turn, reduce the Fe. A second exposure to atomic O after the annealing (not shown) has led to no difference in the observed spectrum, hinting at the first mechanism to be the dominant one, as the Fe appears to be now protected against oxidation. The formation of a surface alloy below graphene is the most likely situation, as no significant reduction in signal strength has been observed after annealing, which excludes large quantities of iron diffusing into the crystal.

With the goal to investigate the properties of freestanding CSLMs, 800 μm wide patches of Fe–Pt CSLMs, based on the system depicted in Figure 7.1 (a), have been fabricated. After the delamination and turn over process, as described in Chapter 6, they have been placed back onto a clean Ir(111) substrate (see Figure 7.2 (a)). Precise manipulator controls combined with a spotsize below 200 $\mu\text{m} \times 200 \mu\text{m}$ enables measurements on a single membrane. To locate such a membrane first the reduction of the Ir 4f signal was monitored during the movement of the crystal in front of the beam. Later on the C 1s and Fe 2p signals were used to confirm that the desired membrane is placed in front of the beam. The XAS results of a turned-over Fe–Pt cluster superlattice membrane are presented in Figure 7.2 (b). The lowest (purple) spectrum shows the CSLM just after degasing at 500 K. The same single peak at 708 eV as in the CSL experiment is observed. No sign of oxidation can be detected, even though the membrane has been exposed to ambient conditions for multiple days. To further establish that the graphene and carbon matrix enclosing the clusters are leak tight the membranes are exposed to 100 L of atomic oxygen. The

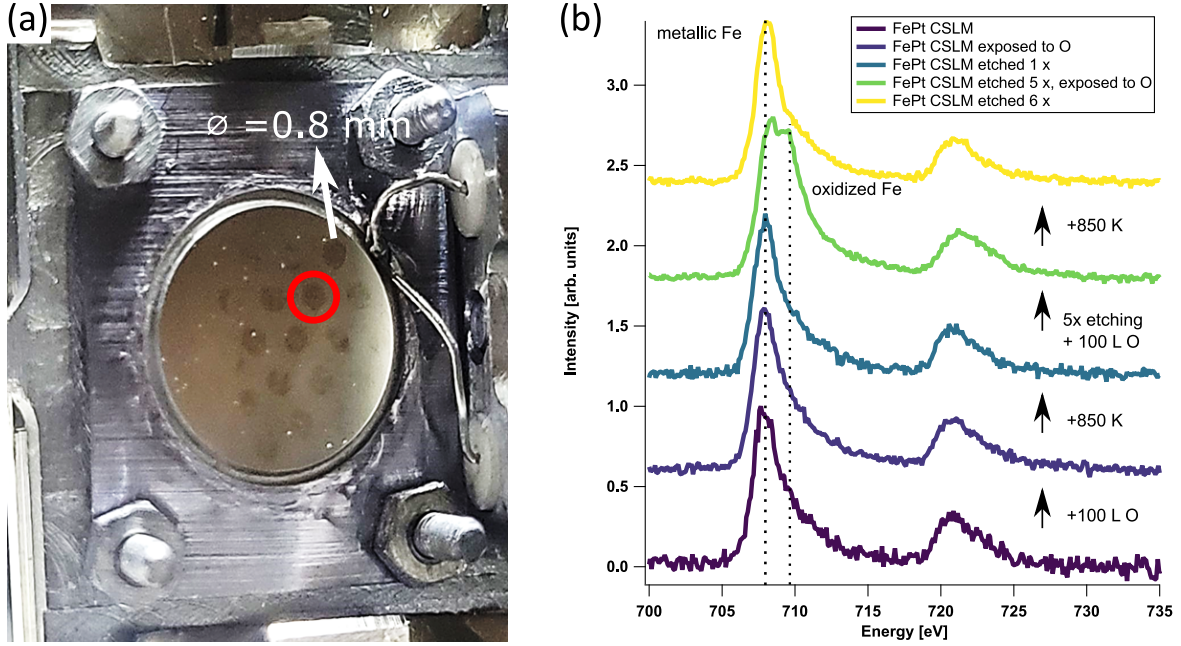


Figure 7.2: (a) Photograph of an Ir(111) sample with Fe–Pt CSLMs transferred, graphene side up, onto the crystal. The membrane diameter is 800 μm . The red circle highlights the membrane that was measured via XPS. (b) XA spectra at the Fe $L_{3,2}$ edges, taken at RT. Spectra of a CSLM of 0.3 ML Fe + 0.3 ML Pt clusters in rising order: after degassing, after exposure to atomic O, after O exposure and annealing to 850 K, after etching 5 times and exposure to atomic O, after etching 6 times. All spectra are normalized.

spectrum (second from the bottom, dark blue) looks identical to the spectrum after ambient exposure, confirming the graphene to be leak tight. Annealing at 850 K for 30 s also does not change the spectrum (middle, turquoise). Only after repeating the O exposure followed by the high temperature annealing 5 times a change is observed when exposing to O again. This time the Fe XAS spectrum (second from top, green) exhibits a clear double peak structure with the second peak at 709.5 eV, indicating that now the holes in graphene, formed by the radical O etching, have grown enough to expose the clusters to the environment again. This leads to immediate oxidation upon O exposure (compare figure 7.2 (a)). Similar to the in situ grown Fe–Pt cluster superlattice, subsequent annealing reduces the Fe again (top spectrum, yellow). However, as the graphene is etched open, further O exposures (not shown) leads to oxidation again.

7.4 Conclusion

In conclusion, we have demonstrated a way to grow a highly ordered Fe–Pt cluster superlattice and form it into a free standing 2D cluster superlattice membrane, which has been shown to fully block gas diffusion and is highly sintering resistant, opening up a pathway to study magnetic cluster - cluster interactions or Fe–Pt phase transitions in samples which are exposed to ambient conditions. Further, we have shown a controllable way to re-open the CSLM via cycles of radical oxygen dosing followed by annealing to 850 K. This treatment validates the CSLM as a potentially highly stable model catalyst housing a wide variety of different combinations of metal nanoparticles in an amorphous carbon matrix.

8 Discussion and Perspectives

8.1 Cluster Superlattice Membranes

Templated cluster superlattices have been studied intensively after their discovery in the early 2000's. One major idea was their usage as a model catalyst, offering a variable template, hosting clusters with a long range order and narrow size distribution. This property would allow averaging techniques like infra-red spectroscopy, surface X-ray diffraction or X-ray photoelectron spectroscopy to be used in the study of chemical reactions on single clusters. However, even though some studies of catalytic effects of cluster superlattices exist, a major downside of these systems is their instability. At high pressures or temperatures the lattices degrade due to particle migration and coalescence.

Driven by the goal to functionalize cluster superlattices and to allow them to withstand higher temperatures and pressures the concept of a cluster superlattice membrane was developed in Chapter 7. Embedding the CSL in an a-C matrix of a few nano-meter thickness has shown to greatly enhance its stability up to temperatures of 1050 K. Although access to the clusters is blocked after the embedding process, through the delamination of the stack of templating layer, clusters and a-C matrix from the substrate a novel free standing 2D material is fabricated.

This paper combines in situ STM, LEED and XPS studies with ex-situ TEM and Raman spectroscopy measurements to follow the necessary steps in the development and fabrication of this intriguing 2D material. STM topographs and LEED images were taken during the growth and embedding of cluster superlattices to confirm the perfect long range order and complete embedding of the CSL. XP spectra of the Ir 4f and C 1s core level were measured and show an increase in the interface component of the Ir signal as the CSL is grown and an even further increase after the embedding. This result is interpreted as a stronger binding of the Gr to the Ir(111) substrate. A subsequent annealing at 850 K leads to a reduction of this interfacial component, as well as a narrowing of the C 1s core level to a more sp^2 dominant signal.

This restructuring of the membrane is what facilitates the next steps: A conventional hydrogen bubbling transfer at an overpotential of around 1.5 V was performed to delaminate multiple

circular membranes with a diameter of 300 μm , supported by PMMA. To confirm the CSL, hosted in the a-C matrix, to be intact, HRTEM was employed. Diffraction measurements also show the regular spaced cluster superlattice, as well as the presence of the Gr layer. Raman spectroscopy doubles as a confirmation of the Gr coverage.

The work presented in Chapter 3 is the basis for all future applications of CSLMs and provides a practical guide to follow in the preparation of this class of heterogeneous 2D materials. It is still open to future work to exploit the versatility of the system itself, as only Ir and Pt clusters were studied and embedded in a-C. Embedding with different materials, such as oxides, has yet to be experimentally tested. Issues here could arise from the need to supply additional oxygen during the deposition of oxide layers and unwanted sintering of the clusters. A lack of strong binding between the clusters and the embedding material could render the endeavour to apply the CSLM as model catalyst futile as sintering might not be sufficiently suppressed once the Gr layer is removed. On the other hand, too strong binding could lead to reduced efficiency in catalysis, due to strong metal support interaction. Different embedding materials will change the way the matrix interacts with the Gr and might open up new pathways to handle the membranes after their removal from the substrate. Ideally one could envision a removal of the embedded clusters and the matrix without the templating layer.

Further experiments are also required to elucidate the role of the annealing and intercalation of europium on the delamination step. Especially the usage of intercalants is questionable, as it is not clear how far the intercalated atoms can travel below the templating layer and if it is even possible to fully intercalate a membrane in UHV with elements like Cs, Eu, Br or Li. Controlled STM experiments in which the starting point of the intercalation is limited to a certain area of the sample could show how mobile the atoms are below the Gr layer.

Improvement of the bubbling transfer is critical to future large scale defect and folding free transfers of the membranes. The role of defects in the membranes, as well as the edges and influence of size, shape and thickness of the membrane on the success of the transfer are also unexplored as of yet.

8.2 Carbon Embedding of Pt Cluster Superlattices Templated by Hexagonal Boron Nitride on Ir(111)

After the introduction of the CSLM, the next objective was to verify the versatility of the system. As the sister-compound of Gr, h-BN produces the same templating and an even stronger stabilizing effect for the growth of CSLs [126]. Its insulating nature makes it an ideal

template to study electron hopping transport between clusters [195]. Also, due to its different atomic constituents, it presents itself as the perfect templating layer to study the embedding of CSL with a-C via in situ XPS measurements as shown in Chapter 4.

In situ STM and XPS measurements were performed in Cologne and Trieste respectively to illuminate the embedding and the interaction of the a-C with the h-BN layer and a Pt cluster superlattice. Spectra of all involved atomic species, B, N, Pt, Ir and C are presented in an effort to understand the behaviour of the main components during growth and high temperature annealing.

The growth process of the a-C matrix proceeds similar to the one already discussed beforehand and in ref. [132]. Carbon first attaches firmly to the Pt clusters. Next the C will accumulate in the areas surrounding the clusters, further rehybridizing the h-BN, leading to an increased binding between h-BN and the Ir(111) surface. This effect shows itself as an increase of the Ir interfacial component, as well as a broadening of the B 1s and N 1s peaks, interpreted as an increase in chemical diversity of the species. After the Pt and h-BN are covered (at roughly 0.8 ML of C) the changes in their spectra under continued C deposition slow down and the C begins to form a network, forming the final matrix.

Annealing the membrane to high temperatures confirms the Pt CSL to be stable up to 850 K. At these temperatures the C also reconfigures and becomes more graphitic, leading to a decreased binding of the membrane to the Ir(111) substrate, similar to the Gr case discussed beforehand. As expected, the embedded CSL, while appearing stable in STM topographs up to 1050 K, will suffer from intercalation of the Pt through the h-BN. This is indicated by a shift of the Pt 4f signal towards a surface dominated one, as well as a decrease in the Ir 4f surface component after the onset of the intercalation above 850 K. The clusters seen in STM topographs (compare Ref.[132] are partially empty carbon shells similar to Ref. [136].

This work shows that the similarities of h-BN and Gr based membrane templates go beyond the obvious templating effect of the moiré unit cell. Amorphous carbon is a universally applicable embedding material for CSLMs. It first binds to the clusters, then the templating layer and finally forms the matrix itself. One major difference between the h-BN and Gr based membranes has been found in the interaction of h-BN with the a-C after annealing to 1250 K. Here it was possible to scratch away the a-C matrix and the embedded clusters with the STM tip, a process impossible on the Gr template. The intercalation issue plaguing Gr templated CSLs above 850 K are also present in h-BN and could for the first time be identified even under a thick a-C layer. However, this also opens up the option to study the intercalation of other species like Cs, Li or Eu which could, in the future, enable easier removal of h-BN based membranes, or block the intercalation of Pt.

8.3 Silicon Cluster Arrays on the Monolayer of Hexagonal Boron Nitride on Ir(111)

Silicon quantum dots show great promise to be applicable for quantum computing and qubit architecture. The expected size dependent electronic band gap and photoluminescence offer great opportunities for optoelectronic applications. In a bid to build devices based on Si nanoclusters it is necessary to fabricate well ordered arrays of similar sized clusters. Contacting such an array is a non-issue and the close size distribution facilitates a collective response of the clusters without smearing out the signal.

In an effort to apply the templating effect of the moiré structure to the non metallic Si clusters, the growth of Si cluster superlattices on h-BN on Ir(111) has been studied in Chapter 5. STM, STS and LEED were used to investigate growth, adsorption sites and electronic properties of the Si clusters.

To begin with, a new surface reconstruction of Si on Ir(111) was identified and in turn used to calibrate deposited Si amounts. Similar to Au or Fe, Silicon does not form a cluster superlattice when deposited on h-BN/Ir(111) at room temperature. In contrast, it forms islands above, or even below the h-BN and large unevenly spaced out clusters. It is possible to form an imperfect cluster superlattice by deposition at 130 K. The binding site of Si clusters in the mesa region of the moiré unit cell also differs from metals or C on h-BN and is likely related to semi-regular point defects. STS measurements of the differential conductance of differently sized Si clusters shows a clear size dependence of the measured band gap of the clusters.

The origin of the point defects in the moiré unit cell of h-BN/Ir(111) is still unresolved, as is their role in the binding of Si clusters. DFT calculations could offer an explanation for the appearance of these semi-regular defects which appear to be present in all grown samples of h-BN on Ir(111), even though they get barely any coverage in the literature. The most likely candidate for the cause are B atoms which can diffuse into the Ir substrate during growth and segregate out during the cooling process [196, 197].

Further experiments are required to actually gauge the collective response of the Si cluster superlattice. Photoluminescence measurements did not yield any results due to the Ir substrate drowning out any response. If it is possible to embed the Si cluster, forming a CSLM there would be a chance to study the size dependent optical response of a Si cluster superlattice. This depends on the embedding process not leading to sintering of the Si clusters however, which, due to the prevalence of SiC bonds, is a strong ask for the system. A change in embedding material however could lead to the desired outcome.

8.4 Transfer Methods for Cluster Superlattice Membranes

The implementation of cluster superlattice membranes in diverse settings necessitates the detachment of the material from the substrate, along with a reliable method for handling the material post-removal. There is a critical requirement for a clean, efficient, and reproducible procedure to precisely position the CSLM onto arbitrary substrates while ensuring the desired orientation. Chapter 6 details the necessary fabrication steps and a working handling procedure to access both sides of the membranes for further research purposes.

The singular most critical factor for the success of removal from the growth substrate is the intercalation of the membranes with water or hydrogen gas. Only intercalated areas are able to be lifted from the substrate via exfoliation methods. The main variables such as size and thickness of the membranes and their influence on the water intercalation are discussed. Evidence points to edge areas of the membranes as starting points for intercalation. However, the seemingly logical conclusion that smaller membranes are easier to intercalate due to their higher circumference to area ratio was not supported by experiments. Defects in the membrane, caused by uneven carbon coverage or the morphology of the substrate also act as nucleation points for intercalated areas. Due to this, thin membranes (~ 5 ML C) show more initial starting areas of intercalation. However, because thin membranes tend to rupture easily, gases developed during the process have an easy way to escape from below the 2D material, hindering further intercalation and render full removals unachievable. Thick membranes (~ 50 ML C) have been found to be fully intercalatable with the largest studied membrane being of circular shape with a 2 mm diameter. However, their handling is difficult due to high amounts of tensile strain, which easily leads to them crumpling or rolling up on themselves.

Depending on the use case, thick membranes can offer advantages due to their large available surface area e.g. as a model catalyst in electrochemistry or in experiments with large probe sizes like XPS. Thin membranes offer the ability to image the clusters with high resolution in TEM, where large areas are not a requirement. A good compromise between the systems has been found in an a-C coverage of roughly 10 ML C.

Two methods to handle CSLMs are presented: The first being a simple transfer with the a-C side facing the environment afterwards and the second one being more involved, but enabling access to the templating layer.

Stamping the intercalated membrane with any type of polymer leads to removal from the substrate, so the focus shifts to a clean and easy transfer. Polydimethylsiloxane (PDMS) stamping is a standard method in the transfer of 2D materials and works for the CSLM as well. Different methods to increase cleanliness and area of transferred materials, such as heating, are described.

The second transfer method is key to further applications of CSLMs, as it exposes the templating layer to the environment. Future experiments hinge on the ability to access this layer, either to contact it via electrodes, or to remove it to gain access to the embedded clusters. A combination of polymer to polymer stamping, followed by chemical removal of the second polymer layer has been shown to be a viable method to transfer the membrane to arbitrary new substrates and has enabled the work described in Chapter 7.

Even though this chapter gives instructions on how to handle CSLMs to achieve desired results, it by no means is to be seen as the be-all and end-all of transfer guides. There are a lot of unanswered questions pertaining to all steps of the process. Starting with the synthetization of the membranes themselves, the origin of the tensile strain in the membranes is not solved. Strategies to lower the stress and thus reduce damages in the membrane after the delamination could be deposition of C at elevated temperatures, or incorporation of metallic elements into the matrix. In situ intercalation of elements to lower the binding between Gr and the Ir(111) substrate are speculated to help in the following removal of the membranes, similar to the removal of pure Gr [170, 171]. It has yet to be shown though, that this step is actually helpful, or even that the intercalated species are mobile enough to reach the inner areas of the membranes which are on the order of hundreds of micro-meters away.

The intercalation process in 1 Mol NaOH solution was typically performed at RT and an overpotential of around 1.65 V. All three factors (temperature, potential and concentration) can impact the outcome [198–201]. Because of the potentials influence, also the geometry of the electrochemical cell can impact the outcome. Until now, a non symmetric setup was used where a Pt electrode was placed in a beaker on one side of the Ir crystal, leading to a difference in voltage gradient over the crystal surface. Future set-ups could make use of a ring shaped Pt-electrode, or a fine Pt grid placed atop the Ir crystal to reduce or avoid this issue.

If future applications or experiments demand a more controlled delamination protocol, all these elements of the preparation and intercalation step can be optimized. In the scope of this work however, the parameter space is too large to efficiently cover.

Finally a working transfer process is describes in detail. The combination of PC and PDMS allows stamping from one polymer to the other followed by a chemical removal of the PC once the CSLM is on the target substrate. This method has produced large areas of clean CSLM for XPS experiments. There are still a number of polymers not yet tested for this purpose which might improve the transfer. Polypropylencarbonate (PPC) for example has very similar properties to PC but exhibits stronger temperature dependent adhesiveness [202]. Polystyrol also has been applied as a solvable temporary layer for successful transfers of graphene[203, 204].

8.5 Functionalization of Fe–Pt Cluster Superlattice Membranes via O Radical Etching

The penultimate step in the full application of CSLM in nano catalysis is the full or partial removal of the templating layer, exposing the clusters to the environment again. To this end, it was necessary to develop a procedure which can remove Gr without also damaging the a-C matrix in a critical way. Prior work by Vinogradov et al has shown O radicals to be able to adsorb on, and, through annealing, controllably etch graphene [205].

In Chapter 7 Fe–Pt cluster superlattice membranes were grown and transferred via a home-developed transfer method to a secondary Ir substrate. XANES measurements of the Fe L_{2,3} edges monitoring the oxidation state of the Fe act as a fingerprint of the state of the templating layer. Non oxidized clusters confirm a closed membrane which is impermeable to O. When the clusters oxidize after repeated oxygen etching steps a partial opening of the Gr template is reached. Annealing of the oxidized clusters shows a re-transformation to the non oxidized state.

This chapter establishes a method to employ CSLMs in future catalysis experiments. The CSLM can be transported with the Gr layer attached, without being impacted by the environmental exposure. Before usage radical O exposure and annealing can then remove the protective layer, laying bare the clusters. TEM imaging of the clusters during and after the O exposure is still required to confirm the excellent cluster ordering. Application of CSLMs in simple electrocatalytic experiments such as the hydrogen evolution reaction, or in CO oxidation are the next logical steps. Ideally it will be possible to study the reactions taking place on single clusters via collective response of the whole cluster superlattice, enabling XPS, infra-red spectroscopy and similar techniques to observe reactions hidden until now by the small size of the clusters.

8.6 The Future of CSLMs

The completion of this thesis marks a significant milestone for cluster superlattice membranes, as they embark on an exciting new phase where their direct application in various experiments becomes possible. By flipping the membrane and placing it onto a metallic substrate, with the templating layer exposed, a promising opportunity arises for STM to explore the backside of the membrane. The opening process, which, so far, is only studied via XPS, could be imaged step by step, including the oxygen radical adsorption and graphene combustion. Once opened, the same system can also be used to study thermal stability, CO adsorption and oxidation, and possible post-growth processes as well as their respective stability and catalytical viability all in situ via STM and temperature programmed desorption. STS measurements will provide insight into the electronic state of the clusters.

Further XPS studies on modern near ambient pressure systems will provide information about the reactivity and stability of clusters outside of UHV conditions. Careful analysis and comparison to calculations will distinguish the reaction pathways of different catalysed reactions. Shrinking the clusters down to the atomic limit will enable studies into single-atom catalysis. TEM investigations will provide information about the structure, as well as the stability of the membrane. They also offer the opportunity to observe the sintering of particles in a highly controlled environment. Application of an opened CSLM as electrode in an electrochemical cell (e.g. for CO oxidation or the hydrogen evolution reaction) would provide further information about the reactivity of the clusters and could be used to probe the long term stability during thousands of reaction cycles.

Moving away from carbon as embedding layer comes with unique opportunities but also challenges. The embedding process itself has to be studied to confirm that a conformal embedding, which does not disturb the long range order of the clusters, is possible. If that and the delamination, are successful a whole new range of experiments opens up. Isolating embedding materials such as Boron enable the study of electron hopping transport between the clusters. Heterostructures of embedding materials (eg. lead on a thin a-C film) could be used to induce superconductivity in the clusters, which could in turn lead to interesting effects when combined with possible magnetic clusters. Oxide supports (e.g.. ceria or titania) would provide an easier opening procedure, as they can't be accidentally etched via oxygen exposure. After the template removal they are able to actively promote the catalytic reactivity of the embedded metals. In the realm of magnetism X-ray magnetic circular dichroism measurements of Fe-Pt or Co-Ptm based CSLMs will provide first insights into the predicted capabilities in phase formation and magnetic interaction within the membranes. A collective response of the clusters could in

principle would also be measurable via the magneto optical Kerr or Faraday effect. Magnetic ordering between the clusters could be measured and imaged via spin polarized STM.

Taking a step back from so far unrealised systems, the growth and delamination process of the CSLMs itself comes with a series of unanswered questions. Where does the strain in the material come from and how can it be reduced? Does intercalation of alkali metals facilitate a better intercalation of the membrane? What are the ideal parameters for the fluid intercalation of the membranes? All these questions could be answered in a series of experiments if the need for a more controlled fabrication should arise.

In conclusion, it is a very exciting time for this intriguing 2D material class, which is filled to the brim with opportunities and open questions.

9 Scientific Appendix: h-BN Based Cluster Superlattice Membranes

As stated in Chapter 3 it is generally possible to create a free standing cluster superlattice membrane based on a templating layer of h-BN. It was shown in Chapter 4, that Pt clusters inside an a-C matrix on h-BN are protected against sintering and the formation of the embedding matrix proceeds similarly to graphene templated membranes. What has been lacking so far was direct evidence of the cluster order still being present after the removal of the h-BN based membrane. Also the expected sintering resistance has not yet been directly proven. Transmission electron microscopy is the ideal tool to image the clusters and determine their thermal stability as well as the possible sintering mechanisms. In this chapter we will discuss h-BN based CSLM as observed by TEM and compare them with the well known system of Ir clusters on h-BN/Ir(111) as measured via STM.

0.6 ML Ir cluster have been grown in situ via e-beam deposition on a full monolayer of h-BN on Ir(111). STM and LEED were performed at this step to confirm the excellent order of the CSL. Figure 9.1 (a) shows an STM topograph of the system of 0.6 ML Ir clusters on h-BN/Ir(111). The expected excellent long range order with a inter cluster spacing of 2.9 nm and narrow size

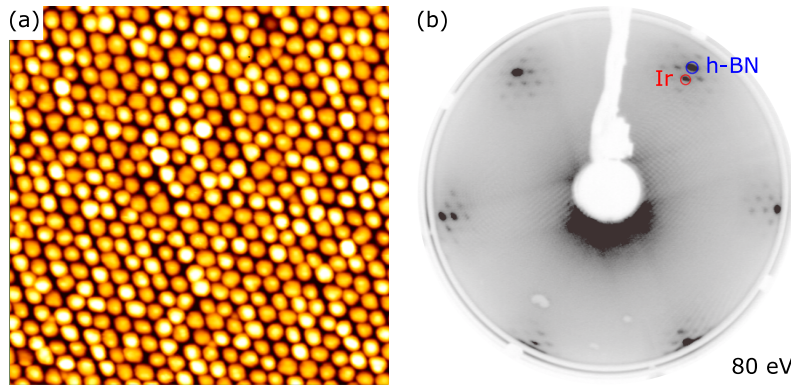


Figure 9.1: (a) STM topograph of 0.6 ML Ir on h-BN/Ir(111). The average cluster size is $s_{\text{avg}} = 68$ atoms. The image size is 60 nm \times 60 nm. (b) Image of the corresponding LEED pattern at 80 eV.

distribution of the system is clearly visible [126]. The corresponding LEED image, displaying the Ir(111) and *h*-BN reflections as well as the moiré reconstructions, is shown in Figure 9.1 (b).

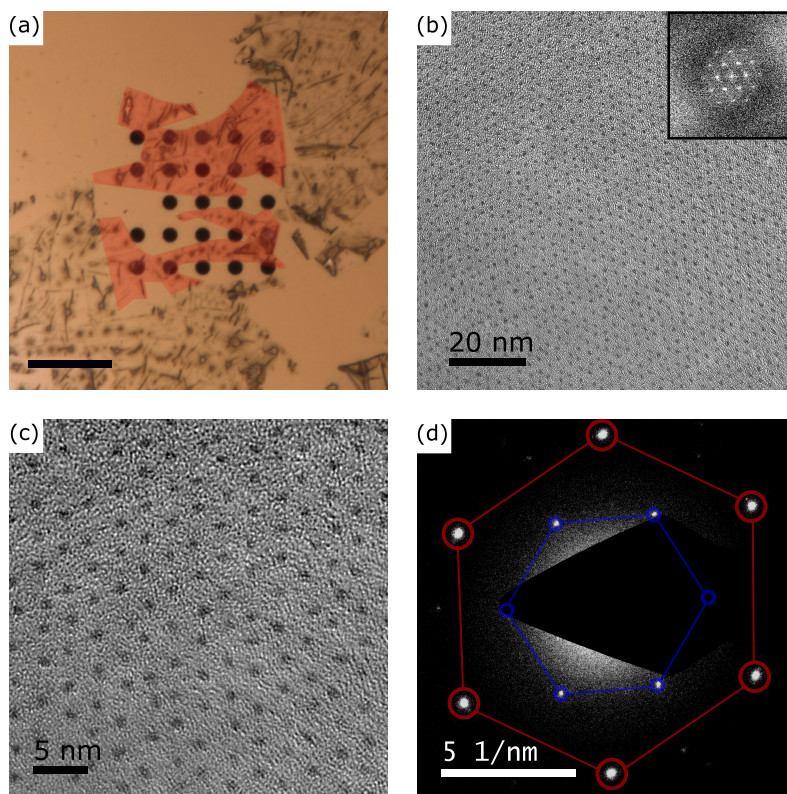


Figure 9.2: (a) Optical microscope image of an *h*-BN based CSLM suspended over the holes of a SiN TEM grid. Areas close to or over holes are highlighted in red. Scale bar is 50 μm . (b) HAADF TEM image of an *h*-BN based Ir cluster superlattice membrane. Inset shows a zoom in on the FFT, displaying the order of the superlattice. (c) HR TEM image of the Ir₆₈ clusters. (d) Selected area diffraction in the area of (b). The first order reflections are highlighted via blue circles. Two spots are hidden by the aperture. Red circles highlight the second order reflections.

After the intercalation and PDMS stamp removal, following the procedure described in Chapter 6, the CSLM was then stamped onto a SiN TEM grid. The result is depicted in Figure 9.2(a). Figure 9.2(b) displays a high resolution TEM image of the CSLM. The sample is remarkably clean and barely any residues from the transfer process are found in the imaged areas. The inter cluster spacing of 2.9 nm is preserved, as well as the order imposed by the former *h*-BN/Ir(111) moiré structure. Fourier filtering the image further strengthens the evidence for a fully preserved cluster ordering, as even second order reflections are observed. Diffraction measurements in the same area, depicted in Figure 9.2 (d), reveal the presence of the covering *h*-BN layer,

which is not identifiable in the real spaces images or their FFT (compare Ref.[134, 206, 207]).

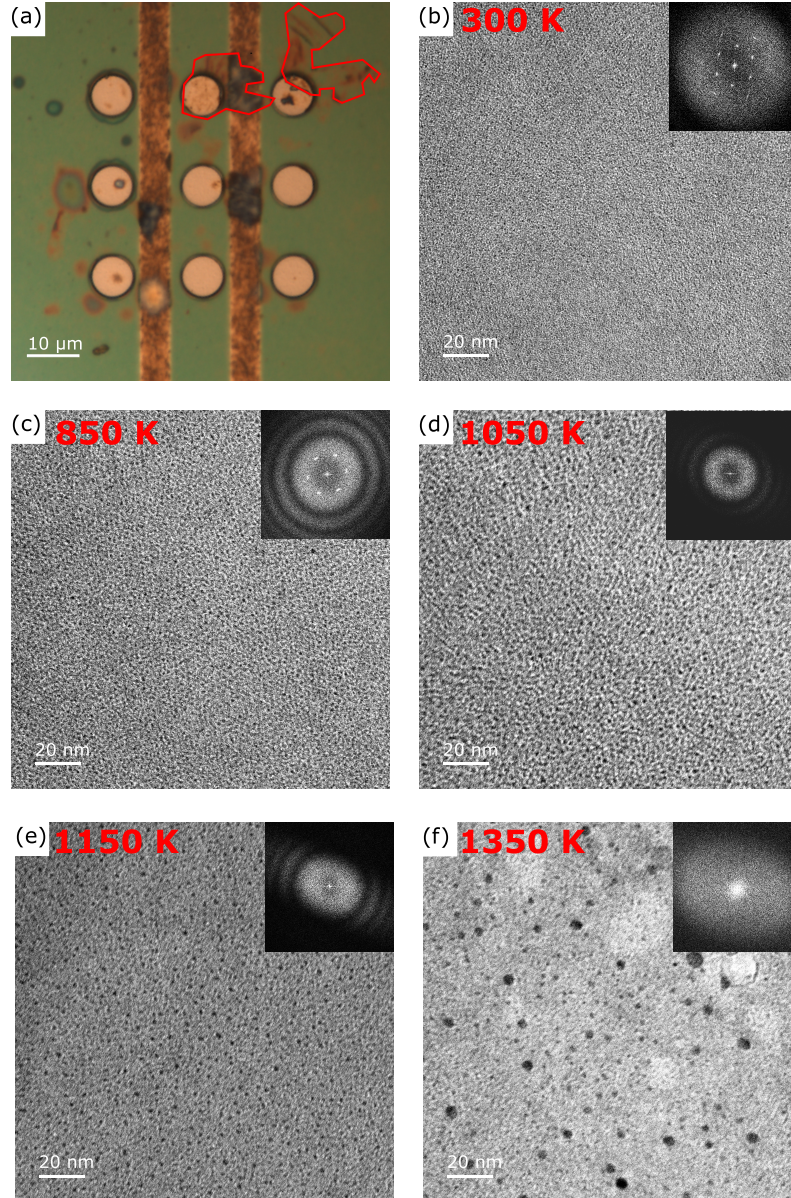


Figure 9.3: (a) Optical microscope image of an h-BN based CSLM suspended over the holes of a heatable TEM protochip. The relevant sample areas are highlighted by red outlines. (b)-(e) HAADF TEM images of an h-BN based Ir cluster superlattice membrane taken at RT after (b) no annealing and heating for 30 s to (c) 850 K, (d) 1050 K, (e) 1150 K, (f) 1350 K. Insets show a zoom in on the FFTs.

To study the thermal stability of the system a part of the same sample was transferred to a heatable TEM grid (see Figure 9.3 (a)). Due to the presence of a native 40 nm thick SiN layer

on the grid, the contrast of the TEM images on the clusters is low (Figure 9.3 (b)), even in the best imaging conditions. The hexagonal pattern observed in the FFT corresponds to the order of the CSL. Even though the contrast is bad, this information can still be used to gauge the temperature at which sintering leads to the destruction of the ordered cluster superlattice. After annealing to 850 K for 30 s (Figure 9.3 (c)) the contrast has improved significantly, without degrading the long range order. This change is attributed to a desorption of contaminants, also observed in XPS measurements in Chapter 7. At 1050 K significant sintering has occurred, and the long range order is only barely recognizable. The perceived increase in contrast is due to increase in mean particle size. Even higher temperatures (1150 K, Figure 9.3(e)) lead to total disordering and creation of larger and larger clusters. The highest probed annealing temperature of 1350 K results in large clusters in the order of 5-10 nm.

The sintering mechanism at temperatures up to 1050 K is not immediately obvious. Particle migration and coalescence has been shown to be blocked by the carbon layer at this temperature [208]. In CSLMs on the Ir(111) growth substrate intercalation through the Gr or *h*-BN layer has been observed. The energy gained by a cluster by becoming part of the Ir bulk is large enough to penetrate an *h*-BN or Gr layer at 1050 K [132, 208]. In general, this mechanism could also explain sintering via PMC. The clusters would escape their carbon shells and move around the *h*-BN surface until they coalesce. While there is energy to be gained this way, the energy barrier required for this sintering mechanism certainly is above that of the intercalation process on the substrate, so we expect PMC to play a minor role in this temperature range.

Ostwald ripening on the other hand would require large Ir atoms to detach from the clusters and move through the a-C matrix. The low solubility of Ir in C and the large inter cluster distance stand against this [209]. However, a significant restructuring of the a-C matrix has been observed at temperatures above 850 K in which the matrix goes from a mainly sp^3 hybridized C to a more graphitic sp^2 dominated one [135, 208, 210]. This could open up channels in the a-C layer through which the Ir atoms are able to move, similar to atoms in the VdW gap of graphite [211, 212].

To further study the mechanisms of sintering in a CSLM a series of TEM images were taken at high temperature (1350 K). The results are presented in Figure 9.4. The clusters highlighted by red circles act as reference points, as they do not change throughout the image series and sample drift at this temperature is an issue. In the first 2 seconds a merger between two smaller particles to the right (highlighted by blue circles) is observed. No significant changes take place between 2 and 4 seconds. Between 4 and 6 seconds two changes are visible: The movement of a whole particle highlighted by orange and the merger of at least 2 particles into a significantly larger one at a different position, highlighted by a blue circle. The observed changes

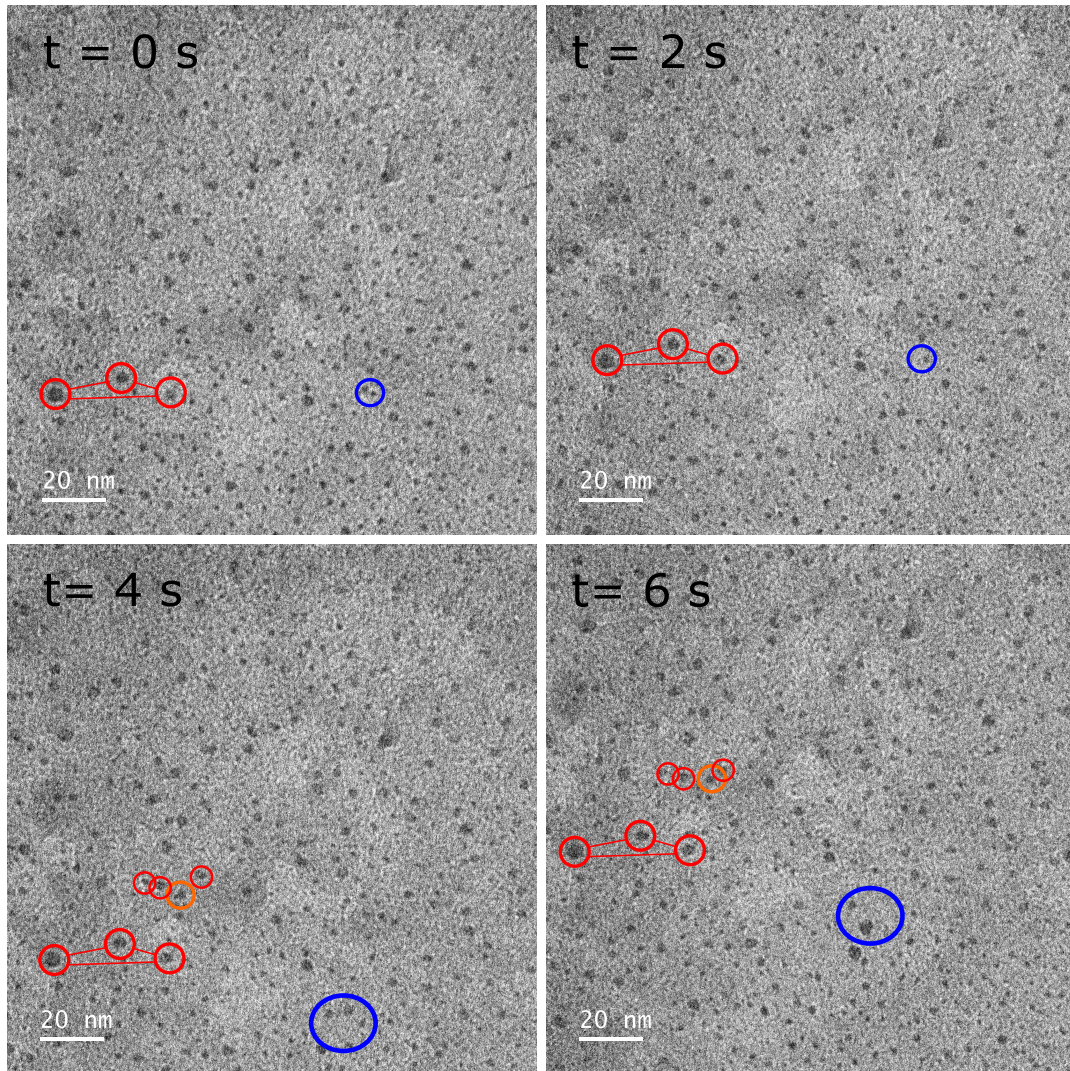


Figure 9.4: A series of TEM images taken at 1350 K with a 2 s time step. The red circle highlight reference points, blue and orange ones changes in the cluster positions.

are the smoking gun evidence for a sintering via particle migration and coalescence happening at 1350 K, as Ostwald ripening would not induce movement of the particles. As it is unlikely that the particles freely move through the carbon, it is suspected that at this temperature the carbon has fully detached from the h-BN and the particles are suspended in the gap. Similar results have been found in Ref. [208], where after annealing the system to 1250 K the a-C layer could be removed easily from the h-BN layer via scratching with an STM tip.

In conclusion, it was shown that h-BN based CSLMs are perfectly capable of stabilizing the cluster superlattice during removal from the growth substrate. TEM imaging has revealed the excellent long range order as well as the presence of h-BN on the sample. An annealing series up to 1350 K was done which presented evidence of the stability of the h-BN CSLM up to at least 850 K. The sintering mechanism destroying the order is presumed to be Ostwald ripening dominated up to 1050 K. A time resolved TEM series was performed at 1350 K, which revealed that at this extreme temperature PMC is the predominant sintering mechanism

10 List of Publications

(Liste der Teilpublikationen)

Parts of the results presented in this thesis can be found in the following publications:

Teile dieser Arbeit wurden als Bestandteil der folgenden Artikel in Fachzeitschriften bereits veröffentlicht:

- [135] **Tobias Hartl**, Moritz Will, Davor Capeta, Rajendra Singh, Daniel Scheinecker, Virginia Boix de la Cruz, Sophia Dellmann, Paolo Lacovig, Silvano Lizzit, Boris V Senkovskiy, Alexander Grüneis, Marko Kralji, Jan Knudsen, Jani Kotakoski, Thomas Michely and Pantelis Bampoulis
Cluster Superlattice Membranes
ACS Nano **14**, 13629 (2020)
- [208] **Tobias Hartl**, Moritz Will, Pantelis Bampoulis, Daniel Herrmann, Philipp Valerius, Charlotte Herbig, Virginia Boix de la Cruz, Paolo Lacovig, Vedran Vonk,, Simon Chung, Andreas Stierle, Silvano Lizzit, Jan Knudsen and Thomas Michely
Carbon Embedding of Pt Cluster Superlattices Templated by Hexagonal Boron Nitride on Ir (111)
J. Phys. Chem. C. **125**, 23435 (2021)
- [133] **Tobias Hartl**, Daniel Herrmann, Moritz Will, Yannic Falke, Alexander Grüneis, Thomas Michely and Pantelis Bampoulis
Silicon cluster arrays on the monolayer of hexagonal boron nitride on Ir (111)
J. Phys. Chem. C. **126**, 6809 (2022)

Further publications:

Weitere Publikationen:

- [132] Moritz Will, Pantelis Bampoulis, **Tobias Hartl** , Philipp Valerius and Thomas Michely
Conformal Embedding of Cluster Superlattices with Carbon
ACS Appl. Mater. Interfaces **11**, 40524 (2019)

- [213] Moritz Will, **Tobias Hartl**, Virginia Boix de la Cruz, Paolo Lacovig, Silvano Lizzit, Jan Knudsen, Thomas Michely and Pantelis Bampoulis
Growth, stability, and electronic decoupling of Pt clusters on h-BN/Ir (111)
J. Phys. Chem. C. **125**, 3880 (2021)

Conference contributions as presenting author:

Konferenzbeiträge als präsentierender Autor:

09/2021 EMRS Fall Meeting, Online Conference, *Cluster Superlattice Membranes*, Talk

05/2022 EWEG 2D, St. Moritz (CH), *Cluster Superlattice Membranes*, Talk

09/2022 DFG Tagung der SKM, Regensburg (DE), *Carbon Embedding of Pt Cluster Superlattices Templated by Hexagonal Boron Nitride on Ir(111)*, Poster

03/2023 DFG Tagung der SKM, Dresden (DE), *Bottom-up synthesis and transfer of free-standing nanocluster arrays supported by carbon*, Talk

Bibliography

- [1] B. Lindström and L. J. Pettersson, “A brief history of catalysis,” *Cattech*, vol. 7, no. 4, pp. 130–138, 2003. 1
- [2] J. J. Berzelius, “Berzelius and the Platinum Metals,” *Platin. Met. Rev.*, vol. 23, no. 4, pp. 155–156, 1979. 1
- [3] H. Davy, “VIII. Some new experiments and observations on the combustion of gaseous mixtures, with an account of a method of preserving a continued light in mixtures of inflammable gases and air without flame,” *Philos. Trans. R. Soc.*, no. 107, pp. 77–85, 1817. 1
- [4] E. Davy, “VI. On some combinations of platinum,” *Philos. Trans. R. Soc.*, no. 110, pp. 108–125, 1820. 1
- [5] Precedence Research, “Catalyst market - global industry analysis, size, share, growth, trends, regional outlook, and forecast 2022-2030,” 2022. 1
- [6] A. Mathew and T. Pradeep, “Noble metal clusters: applications in energy, environment, and biology,” *Part. Part. Syst. Charact.*, vol. 31, no. 10, pp. 1017–1053, 2014. 1
- [7] T. Muroi, “Role of precious metal catalysts,” *Noble Metals*, pp. 301–334, 2012. 1
- [8] J. Kummer, “Use of noble metals in automobile exhaust catalysts,” *J. Phys. Chem.*, vol. 90, no. 20, pp. 4747–4752, 1986. 1
- [9] W. A. De Heer, “The physics of simple metal clusters: experimental aspects and simple models,” *Rev. Mod. Phys.*, vol. 65, no. 3, p. 611, 1993. 1
- [10] G. Pastor, J. Dorantes-Dávila, and K. Bennemann, “Size and structural dependence of the magnetic properties of small 3d-transition-metal clusters,” *Phys. Rev. B*, vol. 40, no. 11, p. 7642, 1989. 2

- [11] Z. Xu, F.-S. Xiao, S. Purnell, O. Alexeev, S. Kawi, S. Deutsch, and B. Gates, “Size-dependent catalytic activity of supported metal clusters,” *Nature*, vol. 372, no. 6504, pp. 346–348, 1994. 2
- [12] R. Smalley, “Laser studies of metal cluster beams,” *Laser Chem.*, vol. 2, no. 3-4, pp. 167–184, 1983. 2
- [13] K. Selby, M. Vollmer, J. Masui, V. Kresin, W. A. de Heer, and W. Knight, “Surface plasma resonances in free metal clusters,” *Phys. Rev. B*, vol. 40, no. 8, p. 5417, 1989.
- [14] D. Cox, K. Reichmann, D. Trevor, and A. Kaldor, “CO chemisorption on free gas phase metal clusters,” *J. Chem. Phys.*, vol. 88, no. 1, pp. 111–119, 1988. 2
- [15] U. Heiz, F. Vanolli, A. Sanchez, and W.-D. Schneider, “Size-dependent molecular dissociation on mass-selected, supported metal clusters,” *J. Am. Chem. Soc.*, vol. 120, no. 37, pp. 9668–9671, 1998. 2
- [16] K. Wettergren, F. F. Schweinberger, D. Deiana, C. J. Ridge, A. S. Crampton, M. D. Roetzer, T. W. Hansen, V. P. Zhdanov, U. Heiz, and C. Langhammer, “High sintering resistance of size-selected platinum cluster catalysts by suppressed Ostwald ripening,” *Nano Lett.*, vol. 14, no. 10, pp. 5803–5809, 2014. 11
- [17] Y. Fukamori, M. König, B. Yoon, B. Wang, F. Esch, U. Heiz, and U. Landman, “Fundamental insight into the substrate-dependent ripening of monodisperse clusters,” *ChemCatChem*, vol. 5, no. 11, pp. 3330–3341, 2013. 2, 11
- [18] D. Franz, S. Runte, C. Busse, S. Schumacher, T. Gerber, T. Michely, M. Mantilla, V. Kilic, J. Zegenhagen, and A. Stierle, “Atomic structure and crystalline order of graphene-supported Ir nanoparticle lattices,” *Phys. Rev. Lett.*, vol. 110, no. 6, p. 065503, 2013. 2, 14, 15
- [19] D. Franz, N. Blanc, J. Coraux, G. Renaud, S. Runte, T. Gerber, C. Busse, T. Michely, P. J. Feibelman, U. Hejral, *et al.*, “Atomic structure of Pt nanoclusters supported by graphene/Ir (111) and reversible transformation under CO exposure,” *Phys. Rev. B.*, vol. 93, no. 4, p. 045426, 2016.
- [20] D. Franz, U. Schröder, R. Shayduk, B. Arndt, H. Noei, V. Vonk, T. Michely, and A. Stierle, “Hydrogen solubility and atomic structure of graphene supported Pd nanoclusters,” *ACS Nano*, vol. 15, no. 10, pp. 15771–15780, 2021. 18

-
- [21] K. Gotterbarm, F. Späth, U. Bauer, C. Bronnbauer, H.-P. Steinrück, and C. Papp, "Reactivity of graphene-supported Pt nanocluster arrays," *ACS Catal.*, vol. 5, no. 4, pp. 2397–2403, 2015. 12, 14
- [22] "Reactivity and Passivation of Fe Nanoclusters on h-BN/Rh (111), author=Waleska, Natalie J and Düll, Fabian and Bachmann, Philipp and Hemauer, Felix and Steinhauer, Johann and Papp, Christian," *Chem.–A European Journal*, vol. 27, no. 68, pp. 17087–17093, 2021. 2
- [23] S. Billinge, "Nanoparticle structures served up on a tray," *Nature*, vol. 495, no. 7442, pp. 453–454, 2013. 2
- [24] A. D. McNaught, A. Wilkinson, *et al.*, *Compendium of chemical terminology*, vol. 1669. Blackwell Science Oxford, 1997. 5
- [25] I. Chorkendorff and J. W. Niemantsverdriet, *Concepts of modern catalysis and kinetics*. John Wiley & Sons, 2017. 5
- [26] H. F. Rase, *Handbook of commercial catalysts: heterogeneous catalysts*. CRC press, 2000. 5
- [27] S. Bhaduri and D. Mukesh, *Homogeneous catalysis: mechanisms and industrial applications*. John Wiley & Sons, 2014. 5
- [28] J. Regalbuto, *Catalyst preparation: science and engineering*. CRC press, 2016. 5
- [29] P. Munnik, P. E. De Jongh, and K. P. De Jong, "Recent developments in the synthesis of supported catalysts," *Chemical reviews*, vol. 115, no. 14, pp. 6687–6718, 2015.
- [30] B. A. Mehrabadi, S. Eskandari, U. Khan, R. D. White, and J. R. Regalbuto, "A review of preparation methods for supported metal catalysts," *Adv. Catal.*, vol. 61, pp. 1–35, 2017. 5
- [31] B. Hammer, Y. Morikawa, and J. K. Nørskov, "CO chemisorption at metal surfaces and overlayers," *Phys. Rev. Lett.*, vol. 76, no. 12, p. 2141, 1996. 5
- [32] F. Pinna, "Supported metal catalysts preparation," *Catal. Today*, vol. 41, no. 1-3, pp. 129–137, 1998. 5
- [33] A. Primo and H. Garcia, "Zeolites as catalysts in oil refining," *Chem. Soc. Rev.*, vol. 43, no. 22, pp. 7548–7561, 2014. 5

- [34] H. Gandhi, G. Graham, and R. McCabe, “Automotive exhaust catalysis,” *J. Catal.*, vol. 216, no. 1-2, pp. 433–442, 2003.
- [35] B. Zhang, X. Tang, Y. Li, Y. Xu, and W. Shen, “Hydrogen production from steam reforming of ethanol and glycerol over ceria-supported metal catalysts,” *Int. J. Hydrog. Energy*, vol. 32, no. 13, pp. 2367–2373, 2007.
- [36] J. Zhang, Y. Zhao, X. Guo, C. Chen, C.-L. Dong, R.-S. Liu, C.-P. Han, Y. Li, Y. Gogotsi, and G. Wang, “Single platinum atoms immobilized on an MXene as an efficient catalyst for the hydrogen evolution reaction,” *Nat. Catal.*, vol. 1, no. 12, pp. 985–992, 2018. 5
- [37] J. Kibsgaard and I. Chorkendorff, “Considerations for the scaling-up of water splitting catalysts,” *Nat. Energy*, vol. 4, no. 6, pp. 430–433, 2019. 5
- [38] L. Liu and A. Corma, “Metal catalysts for heterogeneous catalysis: from single atoms to nanoclusters and nanoparticles,” *Chem. rev.*, vol. 118, no. 10, pp. 4981–5079, 2018. 6
- [39] “Chemistry and properties of nanocrystals of different shapes, author=Burda, Clemens and Chen, Xiaobo and Narayanan, Radha and El-Sayed, Mostafa A, journal=Chem. Rev.,” vol. 105, no. 4, pp. 1025–1102, 2005. 6, 12
- [40] G. A. Somorjai and J. Carrazza, “Structure sensitivity of catalytic reactions,” *Ind. Eng. Chem. Fundam.*, vol. 25, no. 1, pp. 63–69, 1986. 6
- [41] T. Jiang, D. Mowbray, S. Dobrin, H. Falsig, B. Hvolbæk, T. Bligaard, and J. K. Nørskov, “Trends in CO oxidation rates for metal nanoparticles and close-packed, stepped, and kinked surfaces,” *J. Phys. Chem. C.*, vol. 113, no. 24, pp. 10548–10553, 2009. 6
- [42] Y. Gao, N. Shao, Y. Pei, Z. Chen, and X. C. Zeng, “Catalytic activities of subnanometer gold clusters (Au16–Au18, Au20, and Au27–Au35) for CO oxidation,” *ACS Nano*, vol. 5, no. 10, pp. 7818–7829, 2011. 6, 7
- [43] S. Yamazoe, K. Koyasu, and T. Tsukuda, “Nonscalable oxidation catalysis of gold clusters,” *Acc. Chem. Res.*, vol. 47, no. 3, pp. 816–824, 2014. 6, 7
- [44] M. Haruta, N. Yamada, T. Kobayashi, and S. Iijima, “Gold catalysts prepared by coprecipitation for low-temperature oxidation of hydrogen and of carbon monoxide,” *J. Catal.*, vol. 115, no. 2, pp. 301–309, 1989. 6
- [45] A. Sanchez, S. Abbet, U. Heiz, W.-D. Schneider, H. Häkkinen, R. Barnett, and U. Landman, “When gold is not noble: nanoscale gold catalysts,” *J. Phys. Chem. A*, vol. 103, no. 48, pp. 9573–9578, 1999. 6

-
- [46] D. Buceta, Y. Piñeiro, C. Vázquez-Vázquez, J. Rivas, and M. A. López-Quintela, “Metallic clusters: theoretical background, properties and synthesis in microemulsions,” *Catal.*, vol. 4, no. 4, pp. 356–374, 2014. 7
- [47] D. C. Meier and D. W. Goodman, “The influence of metal cluster size on adsorption energies: CO adsorbed on Au clusters supported on TiO₂,” *J. Am. Chem. Soc.*, vol. 126, no. 6, pp. 1892–1899, 2004. 7
- [48] M. Boronat, A. Leyva-Perez, and A. Corma, “Theoretical and experimental insights into the origin of the catalytic activity of subnanometric gold clusters: attempts to predict reactivity with clusters and nanoparticles of gold,” *Acc. Chem. Res.*, vol. 47, no. 3, pp. 834–844, 2014. 7
- [49] K. Taylor, C. Pettiette-Hall, O. Cheshnovsky, and R. Smalley, “Ultraviolet photoelectron spectra of coinage metal clusters,” *J. Chem. Phys.*, vol. 96, no. 4, pp. 3319–3329, 1992. 7
- [50] R. Pal, L.-M. Wang, Y. Pei, L.-S. Wang, and X. C. Zeng, “Unraveling the mechanisms of O₂ activation by size-selected gold clusters: transition from superoxo to peroxo chemisorption,” *J. Am. Chem. Soc.*, vol. 134, no. 22, pp. 9438–9445, 2012. 7
- [51] T. El-Brolossy, T. Abdallah, M. B. Mohamed, S. Abdallah, K. Easawi, S. Negm, and H. Talaat, “Shape and size dependence of the surface plasmon resonance of gold nanoparticles studied by Photoacoustic technique,” *Eur. Phys. J. Spec. Top.*, vol. 153, pp. 361–364, 2008. 7
- [52] L. Du, A. Furube, K. Yamamoto, K. Hara, R. Katoh, and M. Tachiya, “Plasmon-induced charge separation and recombination dynamics in gold- TiO₂ nanoparticle systems: dependence on TiO₂ particle size,” *J. Phys. Chem. C.*, vol. 113, no. 16, pp. 6454–6462, 2009. 7
- [53] K. L. Kelly, E. Coronado, L. L. Zhao, and G. C. Schatz, “The optical properties of metal nanoparticles: the influence of size, shape, and dielectric environment,” 2003. 7
- [54] A. Primo, A. Corma, and H. García, “Titania supported gold nanoparticles as photocatalyst,” *Phys. Chem. Chem. Phys.*, vol. 13, no. 3, pp. 886–910, 2011. 7
- [55] X. Chen, Z. Zheng, X. Ke, E. Jaatinen, T. Xie, D. Wang, C. Guo, J. Zhao, and H. Zhu, “Supported silver nanoparticles as photocatalysts under ultraviolet and visible light irradiation,” *Green Chem.*, vol. 12, no. 3, pp. 414–419, 2010. 7

- [56] X. Guo, C. Hao, G. Jin, H.-Y. Zhu, and X.-Y. Guo, "Copper nanoparticles on graphene support: an efficient photocatalyst for coupling of nitroaromatics in visible light," *Angew. Chem. Int. Ed.*, vol. 53, no. 7, pp. 1973–1977, 2014. 7
- [57] G. Sitja, S. Le Moal, M. Marsault, G. Hamm, F. Leroy, and C. R. Henry, "Transition from molecule to solid state: reactivity of supported metal clusters," *Nano Lett.*, vol. 13, no. 5, pp. 1977–1982, 2013. 7, 8, 13
- [58] U. Heiz, A. Sanchez, S. Abbet, and W.-D. Schneider, "Catalytic oxidation of carbon monoxide on monodispersed platinum clusters: each atom counts," *J. Am. Chem. Soc.*, vol. 121, no. 13, pp. 3214–3217, 1999. 7, 8
- [59] Y. Watanabe, X. Wu, H. Hirata, and N. Isomura, "Size-dependent catalytic activity and geometries of size-selected Pt clusters on TiO₂ (110) surfaces," *Cat. Sci. Tech.*, vol. 1, no. 8, pp. 1490–1495, 2011. 7
- [60] S. Mostafa, F. Behafarid, J. R. Croy, L. K. Ono, L. Li, J. C. Yang, A. I. Frenkel, and B. R. Cuenya, "Shape-dependent catalytic properties of Pt nanoparticles," *J. Am. Chem. Soc.*, vol. 132, no. 44, pp. 15714–15719, 2010.
- [61] J. Mondal, Q. T. Trinh, A. Jana, W. K. H. Ng, P. Borah, H. Hirao, and Y. Zhao, "Size-dependent catalytic activity of palladium nanoparticles fabricated in porous organic polymers for alkene hydrogenation at room temperature," *ACS Appl. Mater. Interfaces*, vol. 8, no. 24, pp. 15307–15319, 2016.
- [62] J. Chen, Q. Zhang, Y. Wang, and H. Wan, "Size-dependent catalytic activity of supported palladium nanoparticles for aerobic oxidation of alcohols," *Adv. Synth. Catal.*, vol. 350, no. 3, pp. 453–464, 2008.
- [63] J. Li, W. Chen, H. Zhao, X. Zheng, L. Wu, H. Pan, J. Zhu, Y. Chen, and J. Lu, "Size-dependent catalytic activity over carbon-supported palladium nanoparticles in dehydrogenation of formic acid," *J. Catal.*, vol. 352, pp. 371–381, 2017.
- [64] F. Li and B. C. Gates, "Size-dependent catalytic activity of zeolite-supported iridium clusters," *J. Phys. Chem. C*, vol. 111, no. 1, pp. 262–267, 2007. 7
- [65] S. Kunz, F. F. Schweinberger, V. Habibpour, M. Röttgen, C. Harding, M. Arenz, and U. Heiz, "Temperature dependent CO oxidation mechanisms on size-selected clusters," *J. Phys. Chem. C*, vol. 114, no. 3, pp. 1651–1654, 2010. 8, 9

-
- [66] M. A. van Spronsen, J. W. Frenken, and I. M. Groot, "Surface science under reaction conditions: CO oxidation on Pt and Pd model catalysts," *Chem. Soc. Rev.*, vol. 46, no. 14, pp. 4347–4374, 2017. 8
- [67] C. Campbell, G. Ertl, H. Kuipers, and J. Segner, "A molecular beam study of the adsorption and desorption of oxygen from a Pt (111) surface," *Surf. Sci.*, vol. 107, no. 1, pp. 220–236, 1981. 8
- [68] K.-H. Allers, H. Pfnür, P. Feulner, and D. Menzel, "Fast reaction products from the oxidation of CO on Pt (111): Angular and velocity distributions of the CO₂ product molecules," *J. Chem. Phys.*, vol. 100, no. 5, pp. 3985–3998, 1994. 8
- [69] D. J. Burnett, A. T. Capitano, A. M. Gabelnick, A. L. Marsh, D. A. Fischer, and J. L. Gland, "In-situ soft X-ray studies of CO oxidation on the Pt (1 1 1) surface," *Surf. Sci.*, vol. 564, no. 1-3, pp. 29–37, 2004. 9
- [70] J.-S. McEwen, S. Payne, H. J. Kreuzer, M. Kinne, R. Denecke, and H.-P. Steinrück, "Adsorption and desorption of CO on Pt (1 1 1): a comprehensive analysis," *Surf. Sci.*, vol. 545, no. 1-2, pp. 47–69, 2003. 9
- [71] M. J. Farias, G. A. Camara, and J. M. Feliu, "Understanding the CO preoxidation and the intrinsic catalytic activity of step sites in stepped Pt surfaces in acidic medium," *J. Phys. Chem. C.*, vol. 119, no. 35, pp. 20272–20282, 2015. 9
- [72] B. Hammer, O. H. Nielsen, and J. Nørskov, "Structure sensitivity in adsorption: CO interaction with stepped and reconstructed Pt surfaces," *Catal. Lett.*, vol. 46, no. 1-2, pp. 31–35, 1997.
- [73] B. Hammer, "Special sites at noble and late transition metal catalysts," *Top. Catal.*, vol. 37, no. 1, pp. 3–16, 2006. 9
- [74] S. Tauster, S. Fung, and R. L. Garten, "Strong metal-support interactions. Group 8 noble metals supported on titanium dioxide," *J. Am. Chem. Soc.*, vol. 100, no. 1, pp. 170–175, 1978. 9
- [75] W. C. Conner Jr and J. L. Falconer, "Spillover in heterogeneous catalysis," *Chem. Rev.*, vol. 95, no. 3, pp. 759–788, 1995. 9
- [76] H. Over, Y. D. Kim, A. Seitsonen, S. Wendt, E. Lundgren, M. Schmid, P. Varga, A. Morgante, and G. Ertl, "Atomic-scale structure and catalytic reactivity of the RuO₂ (110) surface," *Science*, vol. 287, no. 5457, pp. 1474–1476, 2000. 9

- [77] T. W. Hansen, A. T. DeLaRiva, S. R. Challa, and A. K. Datye, "Sintering of catalytic nanoparticles: particle migration or Ostwald ripening?," *Acc. Chem. Res.*, vol. 46, no. 8, pp. 1720–1730, 2013. 10, 11
- [78] S. R. Challa, A. T. Delariva, T. W. Hansen, S. Helveg, J. Sehested, P. L. Hansen, F. Garzon, and A. K. Datye, "Relating rates of catalyst sintering to the disappearance of individual nanoparticles during Ostwald ripening," *J. Am. Chem. Soc.*, vol. 133, no. 51, pp. 20672–20675, 2011. 10
- [79] T. W. Hansen, "Sintering and particle dynamics in supported metal catalysts," *Department of Chemistry (Lyngby, Technical University of Denmark, 2006)*, 2006. 10
- [80] Q. Xu, K. C. Kharas, B. J. Croley, and A. K. Datye, "The sintering of supported Pd automotive catalysts," *ChemCatChem*, vol. 3, no. 6, pp. 1004–1014, 2011. 10, 11
- [81] A. T. DeLaRiva, T. W. Hansen, S. R. Challa, and A. K. Datye, "In situ transmission electron microscopy of catalyst sintering," *J. Catal.*, vol. 308, pp. 291–305, 2013. 11
- [82] C. Granqvist and R. Buhrman, "Statistical model for coalescence of islands in discontinuous films," *Appl. Phys. Lett.*, vol. 27, no. 12, pp. 693–694, 1975. 11
- [83] P. Wynblatt and N. Gjostein, "Supported metal crystallites," *rog. Solid. State Ch.*, vol. 9, pp. 21–58, 1975. 11
- [84] L. Liu, D. M. Meira, R. Arenal, P. Concepcion, A. V. Puga, and A. Corma, "Determination of the evolution of heterogeneous single metal atoms and nanoclusters under reaction conditions: which are the working catalytic sites?," *ACS Catal.*, vol. 9, no. 12, pp. 10626–10639, 2019. 11
- [85] N. Daelman, M. Capdevila-Cortada, and N. López, "Dynamic charge and oxidation state of Pt/CeO₂ single-atom catalysts," *Nat. Mater.*, vol. 18, no. 11, pp. 1215–1221, 2019. 11
- [86] L. Liu and A. Corma, "Evolution of isolated atoms and clusters in catalysis," *Trends Chem.*, vol. 2, no. 4, pp. 383–400, 2020.
- [87] F. Maurer, J. Jelic, J. Wang, A. Gänzler, P. Dolcet, C. Wöll, Y. Wang, F. Studt, M. Casapu, and J.-D. Grunwaldt, "Tracking the formation, fate and consequence for catalytic activity of Pt single sites on CeO₂," *Nat. Catal.*, vol. 3, no. 10, pp. 824–833, 2020. 11
- [88] B. J. O'Neill, D. H. Jackson, J. Lee, C. Canlas, P. C. Stair, C. L. Marshall, J. W. Elam, T. F. Kuech, J. A. Dumesic, and G. W. Huber, "Catalyst design with atomic layer deposition," *ACS Catal.*, vol. 5, no. 3, pp. 1804–1825, 2015. 11

-
- [89] H. Feng, J. Lu, P. C. Stair, and J. W. Elam, "Alumina over-coating on Pd nanoparticle catalysts by atomic layer deposition: enhanced stability and reactivity," *Catal. Lett.*, vol. 141, pp. 512–517, 2011. 11, 16
- [90] J. Lu, J. W. Elam, and P. C. Stair, "Synthesis and stabilization of supported metal catalysts by atomic layer deposition," *Acc. Chem. Res.*, vol. 46, no. 8, pp. 1806–1815, 2013. 11, 16
- [91] P. Yin, S. Hu, K. Qian, Z. Wei, L.-L. Zhang, Y. Lin, W. Huang, H. Xiong, W.-X. Li, and H.-W. Liang, "Quantification of critical particle distance for mitigating catalyst sintering," *Nat. Commun.*, vol. 12, no. 1, p. 4865, 2021. 11
- [92] A. Cao and G. Veser, "Exceptional high-temperature stability through distillation-like self-stabilization in bimetallic nanoparticles," *Nat. Mater.*, vol. 9, no. 1, pp. 75–81, 2010. 11
- [93] Z. Wang, X. Jin, R. Xu, Z. Yang, S. Ma, T. Yan, C. Zhu, J. Fang, Y. Liu, S.-J. Hwang, *et al.*, "Cooperation between Dual Metal Atoms and Nanoclusters Enhances Activity and Stability for Oxygen Reduction and Evolution," *ACS Nano*, 2023. 11
- [94] G. Somorjai and Y. Borodko, "Research in nanosciences—great opportunity for catalysis science," *Catal. Lett.*, vol. 76, pp. 1–5, 2001. 12
- [95] M. X. Yang, D. H. Gracias, P. W. Jacobs, and G. A. Somorjai, "Lithographic fabrication of model systems in heterogeneous catalysis and surface science studies," *Langmuir*, vol. 14, no. 6, pp. 1458–1464, 1998. 12, 13
- [96] O. Y. Loh and H. D. Espinosa, "Nanoelectromechanical contact switches," *Nat. Nanotechnol.*, vol. 7, no. 5, pp. 283–295, 2012. 12
- [97] B. Yan, A. Thubagere, W. R. Premasiri, L. D. Ziegler, L. Dal Negro, and B. M. Reinhard, "Engineered SERS substrates with multiscale signal enhancement: nanoparticle cluster arrays," *ACS Nano*, vol. 3, no. 5, pp. 1190–1202, 2009. 12, 13
- [98] X. Hou, Q. Wang, G. Mao, H. Liu, R. Yu, and X. Ren, "Periodic silver nanocluster arrays over large-area silica nanosphere template as highly sensitive SERS substrate," *Appl. Surf. Sci.*, vol. 437, pp. 92–97, 2018. 12, 13
- [99] G. Hamm, C. Becker, and C. Henry, "Bimetallic Pd–Au nanocluster arrays grown on nanostructured alumina templates," *Nanotechnol.*, vol. 17, no. 8, p. 1943, 2006. 12, 13

- [100] A. T. N'Diaye, T. Gerber, C. Busse, J. Mysliveček, J. Coraux, T. Michely, *et al.*, “A versatile fabrication method for cluster superlattices,” *New J. Phys.*, vol. 11, no. 10, p. 103045, 2009. 12, 13, 14, 15, 17, 73, 74
- [101] A. Javey and H. Dai, “Regular arrays of 2 nm metal nanoparticles for deterministic synthesis of nanomaterials,” *J. Am. Chem. Soc.*, vol. 127, no. 34, pp. 11942–11943, 2005. 13
- [102] K. Anikin, E. Rodyakina, S. Veber, A. Milekhin, A. Latyshev, and D. R. Zahn, “Localized surface plasmon resonance in gold nanocluster arrays on opaque substrates,” *Plasmonics*, vol. 14, pp. 1527–1537, 2019. 13
- [103] J. P. Schmidt, S. E. Cross, and S. K. Buratto, “Surface-enhanced Raman scattering from ordered Ag nanocluster arrays,” *J. Chem. Phys.*, vol. 121, no. 21, pp. 10657–10659, 2004.
- [104] S. K. Cha, J. H. Mun, T. Chang, S. Y. Kim, J. Y. Kim, H. M. Jin, J. Y. Lee, J. Shin, K. H. Kim, and S. O. Kim, “Au–Ag core–shell nanoparticle array by block copolymer lithography for synergistic broadband plasmonic properties,” *ACS Nano*, vol. 9, no. 5, pp. 5536–5543, 2015. 13
- [105] A. Avoyan, G. Rupprechter, A. S. Eppler, and G. A. Somorjai, “Fabrication and characterization of the Ag-based high-technology model nanocluster catalyst for ethylene epoxidation manufactured by electron beam lithography,” *Top. Catal.*, vol. 10, pp. 107–113, 2000. 13
- [106] S. Gohil, R. Chandra, B. Chalke, S. Bose, and P. Ayyub, “Sputter deposition of self-organized nanoclusters through porous anodic alumina templates,” *J. Nanosci. Nanotechnol.*, vol. 7, no. 2, pp. 641–646, 2007. 13
- [107] B.-C. Lau, C.-Y. Liu, H.-Y. Lin, C.-H. Huang, H.-C. Chui, and Y. Tzeng, “Electrochemical fabrication of anodic aluminum oxide films with encapsulated silver nanoparticles as plasmonic photoconductors,” *Electrochem. solid-state lett.*, vol. 14, no. 5, p. E15, 2011. 13
- [108] C.-H. Huang, H.-Y. Lin, S. Chen, C.-Y. Liu, H.-C. Chui, and Y. Tzeng, “Electrochemically fabricated self-aligned 2-D silver/alumina arrays as reliable SERS sensors,” *Opt. Express*, vol. 19, no. 12, pp. 11441–11450, 2011. 13
- [109] A. T. N'Diaye, J. Coraux, T. N. Plasa, C. Busse, T. Michely, *et al.*, “Structure of epitaxial graphene on Ir (111),” *New J. Phys.*, vol. 10, no. 4, p. 043033, 2008. 13, 15

-
- [110] H. Ago, Y. Ogawa, M. Tsuji, S. Mizuno, and H. Hibino, "Catalytic growth of graphene: toward large-area single-crystalline graphene," *J. Phys. Chem. Lett.*, vol. 3, no. 16, pp. 2228–2236, 2012. 13
- [111] H.-J. Freund and G. Pacchioni, "Oxide ultra-thin films on metals: new materials for the design of supported metal catalysts," *Chem. Soc. Rev.*, vol. 37, no. 10, pp. 2224–2242, 2008. 13
- [112] N. Nilius, E. D. Rienks, H.-P. Rust, and H.-J. Freund, "Self-organization of gold atoms on a polar FeO (111) surface," *Phys. Rev. Lett.*, vol. 95, no. 6, p. 066101, 2005. 13
- [113] S. Degen, C. Becker, and K. Wandelt, "Thin alumina films on Ni₃Al (111): A template for nanostructured Pd cluster growth," *Faraday Discuss.*, vol. 125, pp. 343–356, 2004. 13
- [114] C. Becker, A. Rosenhahn, A. Wiltner, K. Von Bergmann, J. Schneider, P. Pervan, M. Milun, M. Kralj, and K. Wandelt, "Al₂O₃-films on Ni₃Al (111): a template for nanostructured cluster growth," *New J. Phys.*, vol. 4, no. 1, p. 75, 2002. 13
- [115] A. Lehnert, S. Rusponi, M. Etzkorn, S. Ouazi, P. Thakur, and H. Brune, "Magnetic anisotropy of Fe and Co adatoms and Fe clusters magnetically decoupled from Ni₃Al (111) by an alumina bilayer," *Phys. Rev. B*, vol. 81, no. 10, p. 104430, 2010. 13
- [116] C. R. Henry, "2D-arrays of nanoparticles as model catalysts," *Catal. Lett.*, vol. 145, pp. 731–749, 2015. 13
- [117] A. T. N'Diaye, S. Bleikamp, P. J. Feibelman, T. Michely, *et al.*, "Two-dimensional Ir cluster lattice on a graphene moiré on Ir (111)," *Phys. Rev. Lett.*, vol. 97, no. 21, p. 215501, 2006. 13, 15, 16
- [118] K. Donner and P. Jakob, "Structural properties and site specific interactions of Pt with the graphene/Ru (0001) moiré overlayer," *J. Chem. Phys.*, vol. 131, no. 16, p. 164701, 2009. 13
- [119] Z. Liang, H. Khosravian, A. Uhl, R. J. Meyer, and M. Trenary, "Graphene domain boundaries on Pt (111) as nucleation sites for Pt nanocluster formation," *Surf. Sci.*, vol. 606, no. 21-22, pp. 1643–1648, 2012.
- [120] E. Sutter, P. Albrecht, B. Wang, M.-L. Bocquet, L. Wu, Y. Zhu, and P. Sutter, "Arrays of Ru nanoclusters with narrow size distribution templated by monolayer graphene on Ru," *Surf. Sci.*, vol. 605, no. 17-18, pp. 1676–1684, 2011.

- [121] Z. Zhou, F. Gao, and D. W. Goodman, “Deposition of metal clusters on single-layer graphene/Ru (0001): Factors that govern cluster growth,” *Surf. Sci.*, vol. 604, no. 13-14, pp. L31–L38, 2010.
- [122] M. Sicot, S. Bouvron, O. Zander, U. Rüdiger, Y. S. Dedkov, and M. Fonin, “Nucleation and growth of nickel nanoclusters on graphene Moiré on Rh (111),” *Appl. Phys. Lett.*, vol. 96, no. 9, p. 093115, 2010.
- [123] D. Mousadacos, M. Pivetta, H. Brune, and S. Rusponi, “Sm cluster superlattice on graphene/Ir (111),” *New J. Phys.*, vol. 19, no. 12, p. 123021, 2017.
- [124] A. Cavallin, M. Pozzo, C. Africh, A. Baraldi, E. Vesselli, C. Dri, G. Comelli, R. Larciprete, P. Lacovig, S. Lizzit, *et al.*, “Local electronic structure and density of edge and facet atoms at Rh nanoclusters self-assembled on a graphene template,” *ACS Nano*, vol. 6, no. 4, pp. 3034–3043, 2012.
- [125] K. Gotterbarm, C. Steiner, C. Bronnbauer, U. Bauer, H.-P. Steinrück, S. Maier, and C. Papp, “Graphene-templated growth of Pd nanoclusters,” *J Phys. Chem. C*, vol. 118, no. 29, pp. 15934–15939, 2014. 13, 14
- [126] M. Will, N. Atodiresei, V. Caciuc, P. Valerius, C. Herbig, and T. Michely, “A monolayer of hexagonal boron nitride on Ir (111) as a template for cluster superlattices,” *ACS Nano*, vol. 12, no. 7, pp. 6871–6880, 2018. 13, 15, 16, 17, 73, 80, 90
- [127] C. Vo-Van, S. Schumacher, J. Coraux, V. Sessi, O. Fruchart, N. B. Brookes, P. Ohresser, and T. Michely, “Magnetism of cobalt nanoclusters on graphene on iridium,” *Appl. Phys. Lett.*, vol. 99, no. 14, p. 142504, 2011. 14
- [128] A. J. Martínez-Galera, H. Guo, M. D. Jiménez-Sánchez, S. Franchi, K. C. Prince, and J. M. Gómez-Rodríguez, “There is life after coking for Ir nanocatalyst superlattices,” *Nano Res.*, vol. 15, no. 8, pp. 6969–6976, 2022. 14
- [129] F. Düll, J. Steinhauer, F. Späth, U. Bauer, P. Bachmann, H.-P. Steinrück, S. Wickert, R. Denecke, and C. Papp, “Ethylene: Its adsorption, reaction, and coking on Pt/h-BN/Rh (111) nanocluster arrays,” *J. Phys. Chem.*, vol. 152, no. 22, p. 224710, 2020. 14
- [130] C. Busse, P. Lazić, R. Djemour, J. Coraux, T. Gerber, N. Atodiresei, V. Caciuc, R. Brako, S. Blügel, J. Zegenhagen, *et al.*, “Graphene on Ir (111): physisorption with chemical modulation,” *Phys. Rev. Lett.*, vol. 107, no. 3, p. 036101, 2011. 14, 15

-
- [131] J. Knudsen, P. J. Feibelman, T. Gerber, E. Grånäs, K. Schulte, P. Stratmann, J. N. Andersen, and T. Michely, “Clusters binding to the graphene moiré on Ir (111): X-ray photoemission compared to density functional calculations,” *Phys. Rev. B*, vol. 85, no. 3, p. 035407, 2012. 15
- [132] M. Will, P. Bampoulis, T. Hartl, P. Valerius, and T. Michely, “Conformal Embedding of Cluster Superlattices with Carbon,” *ACS Appl. Mater. Interfaces*, vol. 11, no. 43, pp. 40524–40532, 2019. 15, 16, 17, 76, 81, 92, 95
- [133] T. Hartl, D. Herrmann, M. Will, Y. Falke, A. Grüneis, T. Michely, and P. Bampoulis, “Silicon cluster arrays on the monolayer of hexagonal boron nitride on Ir (111),” *J. Phys. Chem. C*, vol. 126, no. 15, pp. 6809–6814, 2022. 15, 95, 122
- [134] F. H. Farwick zum Hagen, D. M. Zimmermann, C. C. Silva, C. Schlueter, N. Atodiresei, W. Jolie, A. J. Martinez-Galera, D. Dombrowski, U. A. Schroder, M. Will, *et al.*, “Structure and growth of hexagonal boron nitride on Ir (111),” *ACS Nano*, vol. 10, no. 12, pp. 11012–11026, 2016. 15, 91
- [135] T. Hartl, M. Will, D. Capeta, R. Singh, D. Scheinecker, V. Boix de la Cruz, S. Dellmann, P. Lacovig, S. Lizzit, B. V. Senkovskiy, *et al.*, “Cluster Superlattice Membranes,” *ACS Nano*, vol. 14, no. 10, pp. 13629–13637, 2020. 16, 18, 61, 62, 64, 73, 92, 95, 121
- [136] C. Herbig, T. Knispel, S. Simon, U. A. Schröder, A. J. Martínez-Galera, M. A. Arman, C. Teichert, J. Knudsen, A. V. Krashenninnikov, and T. Michely, “From permeation to cluster arrays: graphene on Ir (111) exposed to carbon vapor,” *Nano Lett.*, vol. 17, no. 5, pp. 3105–3112, 2017. 16, 81
- [137] R. Alcala, M. Mavrikakis, and J. A. Dumesic, “DFT studies for cleavage of C–C and C–O bonds in surface species derived from ethanol on Pt (111),” *J. Catal.*, vol. 218, no. 1, pp. 178–190, 2003. 16
- [138] W. McMillan, “Tunneling model of the superconducting proximity effect,” *Phys. Rev.*, vol. 175, no. 2, p. 537, 1968. 17
- [139] V. Cherkez, J. Cuevas, C. Brun, T. Cren, G. Ménard, F. Debontridder, V. Stolyarov, and D. Roditchev, “Proximity effect between two superconductors spatially resolved by scanning tunneling spectroscopy,” *Phys. Rev. X*, vol. 4, no. 1, p. 011033, 2014. 17
- [140] S. Schumacher, F. Huttmann, M. Petrović, C. Witt, D. F. Förster, C. Vo-Van, J. Coraux, A. J. Martinez-Galera, V. Sessi, I. Vergara, *et al.*, “Europium underneath graphene on Ir

- (111): Intercalation mechanism, magnetism, and band structure,” *Phys. Rev. B*, vol. 90, no. 23, p. 235437, 2014. 18
- [141] S. Schumacher, T. O. Wehling, P. Lazic, S. Runte, D. F. Förster, C. Busse, M. Petrović, M. Kralj, S. Blügel, N. Atodiresei, *et al.*, “The backside of graphene: manipulating adsorption by intercalation,” *Nano Lett.*, vol. 13, no. 11, pp. 5013–5019, 2013.
- [142] U. A. Schröder, M. Petrović, T. Gerber, A. J. Martínez-Galera, E. Grånäs, M. A. Arman, C. Herbig, J. Schnadt, M. Kralj, J. Knudsen, *et al.*, “Core level shifts of intercalated graphene,” *2D Mater.*, vol. 4, no. 1, p. 015013, 2016.
- [143] Z. Liu, A. Hinaut, S. Peeters, S. Scherb, E. Meyer, M. C. Righi, and T. Glatzel, “Reconstruction of a 2D layer of KBr on Ir (111) and electromechanical alteration by graphene,” *Beilstein J. Nanotechnol.*, vol. 12, no. 1, pp. 432–439, 2021. 18
- [144] Y. Wang, Y. Zheng, X. Xu, E. Dubuisson, Q. Bao, J. Lu, and K. P. Loh, “Electrochemical delamination of CVD-grown graphene film: toward the recyclable use of copper catalyst,” *ACS Nano*, vol. 5, no. 12, pp. 9927–9933, 2011. 18
- [145] A. Wang, J. Li, and T. Zhang, “Heterogeneous single-atom catalysis,” *Nat. Rev. Chem.*, vol. 2, no. 6, pp. 65–81, 2018. 18
- [146] X.-F. Yang, A. Wang, B. Qiao, J. Li, J. Liu, and T. Zhang, “Single-atom catalysts: a new frontier in heterogeneous catalysis,” *Acc. Chem. Res.*, vol. 46, no. 8, pp. 1740–1748, 2013. 18
- [147] G. S. Parkinson, “Single-atom catalysis: How structure influences catalytic performance,” *Catal. Lett.*, vol. 149, pp. 1137–1146, 2019. 18
- [148] Z. Jakub, J. Hulva, M. Meier, R. Bliem, F. Kraushofer, M. Setvin, M. Schmid, U. Diebold, C. Franchini, and G. S. Parkinson, “Local structure and coordination define adsorption in a model Ir1/Fe3O4 single-atom catalyst,” *Angew. Chem. Int. Ed.*, vol. 58, no. 39, pp. 13961–13968, 2019.
- [149] H. Li, B. Yu, Z. Zhuang, W. Sun, B. Jia, and T. Ma, “A small change in the local atomic environment for a big improvement in single-atom catalysis,” *J. Mater. Chem. A*, vol. 9, no. 7, pp. 4184–4192, 2021. 18
- [150] R. Imbihl, R. Behm, and R. Schlögl, “Bridging the pressure and material gap in heterogeneous catalysis,” *Phys. Chem. Chem. Phys.*, vol. 9, no. 27, p. 3459, 2007. 18

-
- [151] Ž. Šljivančanin and A. Pasquarello, “Supported Fe nanoclusters: evolution of magnetic properties with cluster size,” *Phys. Rev. Lett.*, vol. 90, no. 24, p. 247202, 2003. 19
- [152] S. Baker, C. Binns, K. Edmonds, M. Maher, S. Thornton, S. Louch, and S. Dhesi, “Enhancements in magnetic moments of exposed and Co-coated Fe nanoclusters as a function of cluster size,” *J. Magn. Magn. Mater.*, vol. 247, no. 1, pp. 19–25, 2002. 19
- [153] Y. Kraftmakher, “Magnetic field of a dipole and the dipole–dipole interaction,” *Eur. J. Phys.*, vol. 28, no. 3, p. 409, 2007. 19
- [154] D. J. Sellmyer, Y. Xu, M. Yan, Y. Sui, J. Zhou, and R. Skomski, “Assembly of high-anisotropy L10 FePt nanocomposite films,” *J. Magn. Magn. Mater.*, vol. 303, no. 2, pp. 302–308, 2006. 19, 73
- [155] P. Capiod, L. Bardotti, A. Tamion, O. Boisson, C. Albin, V. Dupuis, G. Renaud, P. Ohresser, and F. Tournus, “Elaboration of nanomagnet arrays: organization and magnetic properties of mass-selected FePt nanoparticles deposited on epitaxially grown graphene on Ir (111),” *Phys. Rev. Lett.*, vol. 122, no. 10, p. 106802, 2019. 19, 73
- [156] K. S. Novoselov, A. Mishchenko, o. A. Carvalho, and A. Castro Neto, “2D materials and van der Waals heterostructures,” *Science*, vol. 353, no. 6298, p. aac9439, 2016. 61, 73
- [157] A. K. Geim, “Graphene: status and prospects,” *Science*, vol. 324, no. 5934, pp. 1530–1534, 2009. 61
- [158] S. Manzeli, D. Ovchinnikov, D. Pasquier, O. V. Yazyev, and A. Kis, “2D transition metal dichalcogenides,” *Nature Rev. Mater.*, vol. 2, no. 8, pp. 1–15, 2017. 61
- [159] K. Zhang, Y. Feng, F. Wang, Z. Yang, and J. Wang, “Two dimensional hexagonal boron nitride (2D-hBN): synthesis, properties and applications,” *J. Mater. Chem. C*, vol. 5, no. 46, pp. 11992–12022, 2017.
- [160] A. Carvalho, M. Wang, X. Zhu, A. S. Rodin, H. Su, and A. H. Castro Neto, “Phosphorene: from theory to applications,” *Nature Rev. Mater.*, vol. 1, no. 11, pp. 1–16, 2016.
- [161] A. K. Geim and I. V. Grigorieva, “Van der Waals heterostructures,” *Nature*, vol. 499, no. 7459, pp. 419–425, 2013. 61
- [162] X. Cai, Y. Luo, B. Liu, and H.-M. Cheng, “Preparation of 2D material dispersions and their applications,” *Chem. Soc. Rev.*, vol. 47, no. 16, pp. 6224–6266, 2018. 61

- [163] R. Frisenda, E. Navarro-Moratalla, P. Gant, D. P. De Lara, P. Jarillo-Herrero, R. V. Gorbachev, and A. Castellanos-Gomez, “Recent progress in the assembly of nanodevices and van der Waals heterostructures by deterministic placement of 2D materials,” *Chemical Society Reviews*, vol. 47, no. 1, pp. 53–68, 2018. 61
- [164] M. Yankowitz, S. Chen, H. Polshyn, Y. Zhang, K. Watanabe, T. Taniguchi, D. Graf, A. F. Young, and C. R. Dean, “Tuning superconductivity in twisted bilayer graphene,” *Science*, vol. 363, no. 6431, pp. 1059–1064, 2019. 61
- [165] J. Li, X. Yang, Y. Liu, B. Huang, R. Wu, Z. Zhang, B. Zhao, H. Ma, W. Dang, Z. Wei, *et al.*, “General synthesis of two-dimensional van der Waals heterostructure arrays,” *Nature*, vol. 579, no. 7799, pp. 368–374, 2020.
- [166] Z. Dai, L. Liu, and Z. Zhang, “Strain engineering of 2D materials: issues and opportunities at the interface,” *Adv. Mater.*, vol. 31, no. 45, p. 1805417, 2019. 61
- [167] L.-P. Ma, W. Ren, and H.-M. Cheng, “Transfer methods of graphene from metal substrates: A review,” *Small Methods*, vol. 3, no. 7, p. 1900049, 2019. 63
- [168] Z. Zhang, X. Ji, J. Shi, X. Zhou, S. Zhang, Y. Hou, Y. Qi, Q. Fang, Q. Ji, Y. Zhang, *et al.*, “Direct chemical vapor deposition growth and band-gap characterization of MoS₂/h-BN van der Waals heterostructures on Au foils,” *ACS Nano*, vol. 11, no. 4, pp. 4328–4336, 2017.
- [169] Y. Gao, Z. Liu, D.-M. Sun, L. Huang, L.-P. Ma, L.-C. Yin, T. Ma, Z. Zhang, X.-L. Ma, L.-M. Peng, *et al.*, “Large-area synthesis of high-quality and uniform monolayer WS₂ on reusable Au foils,” *Nat. Commun.*, vol. 6, no. 1, p. 8569, 2015. 63
- [170] I. Š. Rakić, D. Čapeta, M. Plodinec, and M. Kralj, “Large-scale transfer and characterization of macroscopic periodically nano-rippled graphene,” *Carbon*, vol. 96, pp. 243–249, 2016. 64, 84
- [171] M. Petrović, I. Šrut Rakić, S. Runte, C. Busse, J. Sadowski, P. Lazić, I. Pletikosić, Z.-H. Pan, M. Milun, P. Pervan, *et al.*, “The mechanism of caesium intercalation of graphene,” *Nat. Commun.*, vol. 4, no. 1, p. 2772, 2013. 64, 84
- [172] S. Deguchi, J. Hotta, S. Yokoyama, and T. S. Matsui, “Viscoelastic and optical properties of four different PDMS polymers,” *J. Micromech. Microeng.*, vol. 25, no. 9, p. 097002, 2015. 67

-
- [173] A. Jain, P. Bharadwaj, S. Heeg, M. Parzefall, T. Taniguchi, K. Watanabe, and L. Novotny, “Minimizing residues and strain in 2D materials transferred from PDMS,” *Nanotechnol.*, vol. 29, no. 26, p. 265203, 2018. 67
- [174] D. Purdie, N. Pugno, T. Taniguchi, K. Watanabe, A. Ferrari, and A. Lombardo, “Cleaning interfaces in layered materials heterostructures,” *Nat. Commun.*, vol. 9, no. 1, p. 5387, 2018. 67, 68, 70
- [175] H.-W. Guo, Z. Hu, Z.-B. Liu, and J.-G. Tian, “Stacking of 2D materials,” *Adv. Funct. Mater.*, vol. 31, no. 4, p. 2007810, 2021.
- [176] T. F. Schranhamer, M. Sharma, R. Singh, and S. Das, “Review and comparison of layer transfer methods for two-dimensional materials for emerging applications,” *Chem. Soc. Rev.*, vol. 50, no. 19, pp. 11032–11054, 2021. 68
- [177] S. Das, J. A. Robinson, M. Dubey, H. Terrones, and M. Terrones, “Beyond graphene: progress in novel two-dimensional materials and van der Waals solids,” *Annu. Rev. Mater. Res.*, vol. 45, pp. 1–27, 2015. 73
- [178] S.-J. Liang, B. Cheng, X. Cui, and F. Miao, “Van der Waals heterostructures for high-performance device applications: challenges and opportunities,” *Adv. Mater.*, vol. 32, no. 27, p. 1903800, 2020. 73
- [179] P. Rodríguez-Kessler and J. Ricardo-Chávez, “Structures of FePt Clusters and their Interactions with the O₂ Molecule,” *Chem. Phys. Lett.*, vol. 622, pp. 34–41, 2015. 73
- [180] L. Li, Y.-Z. Wang, X.-X. Wang, K.-K. Song, X.-D. Jian, P. Qian, Y. Bai, and Y.-J. Su, “Size and stoichiometry effect of FePt bimetal nanoparticle catalyst for CO oxidation: A DFT study,” *J. Phys. Chem. C*, vol. 124, no. 16, pp. 8706–8715, 2020. 76
- [181] J. Wang, Z. Wang, S. Li, R. Wang, and Y. Song, “Surface and interface engineering of FePt/C nanocatalysts for electro-catalytic methanol oxidation: Enhanced activity and durability,” *Nanoscale*, vol. 9, no. 12, pp. 4066–4075, 2017.
- [182] D. Chen, X. Zhao, S. Chen, H. Li, X. Fu, Q. Wu, S. Li, Y. Li, B.-L. Su, and R. S. Ruoff, “One-pot fabrication of FePt/reduced graphene oxide composites as highly active and stable electrocatalysts for the oxygen reduction reaction,” *Carbon*, vol. 68, pp. 755–762, 2014.

- [183] Z. Meng, F. Xiao, Z. Wei, X. Guo, Y. Zhu, Y. Liu, G. Li, Z.-Q. Yu, M. Shao, and W.-Y. Wong, “Direct synthesis of L1 0-FePt nanoparticles from single-source bimetallic complex and their electrocatalytic applications in oxygen reduction and hydrogen evolution reactions,” *Nano Res.*, vol. 12, pp. 2954–2959, 2019. 73
- [184] C. Barreateau and D. Spanjaard, “Magnetic and electronic properties of bulk and clusters of FePt L10,” *J. Phys. Condens. Matter.*, vol. 24, no. 40, p. 406004, 2012. 73
- [185] H. Ebert, S. Bornemann, J. Minár, P. Dederichs, R. Zeller, and I. Cabria, “Magnetic properties of Co-and FePt-clusters,” *Comput. Mater. Sci.*, vol. 35, no. 3, pp. 279–282, 2006.
- [186] Y. Xu, Z. Sun, Y. Qiang, and D. J. Sellmyer, “Magnetic properties of L 1 0 FePt and FePt: Ag nanocluster films,” *J. Appl. Phys.*, vol. 93, no. 10, pp. 8289–8291, 2003.
- [187] J. Lyubina, B. Rellinghaus, O. Gutfleisch, and M. Albrecht, “Structure and magnetic properties of L10-ordered Fe–Pt alloys and nanoparticles,” in *Handb. Magn. Mater.*, vol. 19, pp. 291–407, Elsevier, 2011.
- [188] V. Dupuis, G. Khadra, S. Linas, A. Hillion, L. Gagnaniello, A. Tamion, J. Tuillon-Combes, L. Bardotti, F. Tournus, E. Otero, *et al.*, “Magnetic moments in chemically ordered mass-selected CoPt and FePt clusters,” *J. Magn. Magn. Mater.*, vol. 383, pp. 73–77, 2015. 73
- [189] O. Dmitrieva, M. Spasova, C. Antoniak, M. Acet, G. Dumpich, J. Kästner, M. Farle, K. Fauth, U. Wiedwald, H.-G. Boyen, *et al.*, “Magnetic moment of Fe in oxide-free FePt nanoparticles,” *Phys. Rev. B*, vol. 76, no. 6, p. 064414, 2007. 76
- [190] C. Antoniak, M. E. Gruner, M. Spasova, A. V. Trunova, F. M. Römer, A. Warland, B. Krumme, K. Fauth, S. Sun, P. Entel, *et al.*, “A guideline for atomistic design and understanding of ultrahard nanomagnets,” *Nat. Commun.*, vol. 2, no. 1, p. 528, 2011. 76
- [191] T. Regan, H. Ohldag, C. Stamm, F. Nolting, J. Lüning, J. Stöhr, and R. White, “Chemical effects at metal/oxide interfaces studied by x-ray-absorption spectroscopy,” *Phys. Rev. B*, vol. 64, no. 21, p. 214422, 2001. 76
- [192] J. Brede, J. Sławińska, M. Abadia, C. Rogero, J. E. Ortega, I. Piquero-Zulaica, J. Lobo-Checa, A. Arnau, and J. I. Cerdá, “Tuning the Graphene on Ir (111) adsorption regime by Fe/Ir surface-alloying,” *2D Mater.*, vol. 4, no. 1, p. 015016, 2016. 76

-
- [193] B. Reddy, F. Rasouli, M. Hajaligol, and S. Khanna, “Novel pathway for CO oxidation on a Fe₂O₃ cluster,” *Chem. Phys. Lett.*, vol. 384, no. 4-6, pp. 242–245, 2004. 76
- [194] T. Yan, D. W. Redman, W.-Y. Yu, D. W. Flaherty, J. A. Rodriguez, and C. B. Mullins, “CO oxidation on inverse Fe₂O₃/Au (1 1 1) model catalysts,” *J. Catal.*, vol. 294, pp. 216–222, 2012. 76
- [195] J. Wang, F. Ma, W. Liang, and M. Sun, “Electrical properties and applications of graphene, hexagonal boron nitride (h-BN), and graphene/h-BN heterostructures,” *Mater. Today Phys.*, vol. 2, pp. 6–34, 2017. 81
- [196] K. M. Omambac, M. Petrovic, P. Bampoulis, C. Brand, M. A. Kriegel, P. Dreher, D. Janoschka, U. Hagemann, N. Hartmann, P. Valerius, *et al.*, “Segregation-enhanced epitaxy of borophene on Ir (111) by thermal decomposition of borazine,” *ACS Nano*, vol. 15, no. 4, pp. 7421–7429, 2021. 82
- [197] M. G. Cuxart, K. Seufert, V. Chesnyak, W. A. Waqas, A. Robert, M.-L. Bocquet, G. S. Duesberg, H. Sachdev, and W. Auwärter, “Borophenes made easy,” *Sci. Adv.*, vol. 7, no. 45, p. eabk1490, 2021. 82
- [198] L. Liu, X. Liu, Z. Zhan, W. Guo, C. Xu, J. Deng, D. Chakarov, P. Hyldgaard, E. Schröder, A. Yurgens, *et al.*, “A mechanism for highly efficient electrochemical bubbling delamination of CVD-grown graphene from metal substrates,” *Adv. Mater. Interfaces*, vol. 3, no. 8, p. 1500492, 2016. 84
- [199] J. Kim, S. Kwon, D.-H. Cho, B. Kang, H. Kwon, Y. Kim, S. O. Park, G. Y. Jung, E. Shin, W.-G. Kim, *et al.*, “Direct exfoliation and dispersion of two-dimensional materials in pure water via temperature control,” *Nat. Commun.*, vol. 6, no. 1, p. 8294, 2015.
- [200] K. Verguts, K. Schouteden, C.-H. Wu, L. Peters, N. Vrancken, X. Wu, Z. Li, M. Erkens, C. Porret, C. Huyghebaert, *et al.*, “Controlling water intercalation is key to a direct graphene transfer,” *ACS Appl. Mater. Interfaces*, vol. 9, no. 42, pp. 37484–37492, 2017.
- [201] K. Verguts, J. Coroa, C. Huyghebaert, S. De Gendt, and S. Brems, “Graphene delamination using ‘electrochemical methods’: An ion intercalation effect,” *Nanoscale*, vol. 10, no. 12, pp. 5515–5521, 2018. 84
- [202] K. Kinoshita, R. Moriya, M. Onodera, Y. Wakafuji, S. Masubuchi, K. Watanabe, T. Taniguchi, and T. Machida, “Dry release transfer of graphene and few-layer h-BN by utilizing thermoplasticity of polypropylene carbonate,” *NPJ 2D Mater. Appl.*, vol. 3, no. 1, p. 22, 2019. 84

- [203] T. Nasir, B. J. Kim, M. Hassnain, S. H. Lee, B. J. Jeong, I. J. Choi, Y. Kim, H. K. Yu, and J.-Y. Choi, “Plasticized polystyrene by addition of diene based molecules for defect-less cvd graphene transfer,” *Polymers*, vol. 12, no. 8, p. 1839, 2020. 84
- [204] T. Nasir, B. J. Kim, K.-W. Kim, S. H. Lee, H. K. Lim, D. K. Lee, B. J. Jeong, H. C. Kim, H. K. Yu, and J.-Y. Choi, “Design of softened polystyrene for crack-and contamination-free large-area graphene transfer,” *Nanoscale*, vol. 10, no. 46, pp. 21865–21870, 2018. 84
- [205] N. Vinogradov, K. Schulte, M. L. Ng, A. Mikkelsen, E. Lundgren, N. Mårtensson, and A. Preobrajenski, “Impact of atomic oxygen on the structure of graphene formed on Ir (111) and Pt (111),” *J. Phys. Chem. C*, vol. 115, no. 19, pp. 9568–9577, 2011. 85
- [206] X. Wang, M. Hossain, Z. Wei, and L. Xie, “Growth of two-dimensional materials on hexagonal boron nitride (h-BN),” *Nanotechnol.*, vol. 30, no. 3, p. 034003, 2018. 91
- [207] H. Oh, J. Jo, Y. Tchae, H. Yoon, H. Hwi Lee, S.-S. Kim, M. Kim, B.-H. Sohn, and G.-C. Yi, “Centimeter-sized epitaxial h-BN films,” *NPG Asia Mater.*, vol. 8, no. 11, pp. e330–e330, 2016. 91
- [208] T. Hartl, M. Will, P. Bampoulis, D. Herrmann, P. Valerius, C. Herbig, V. Boix de la Cruz, P. Lacovig, V. Vonk, S. Chung, *et al.*, “Carbon Embedding of Pt Cluster Superlattices Templated by Hexagonal Boron Nitride on Ir (111),” *J. Phys. Chem. C*, vol. 125, no. 42, pp. 23435–23444, 2021. 92, 94, 95, 121
- [209] P. Franke and D. Neuschütz, “Binary Systems from BC to Cr-Zr,” 2004. 92
- [210] O. Krivoruchko, A. Shmakov, and V. Zaikovskii, “In situ X-ray diffraction study of solid state transformations during catalytic graphitisation of amorphous carbon,” *Nucl. Instrum. Methods. Phys. Res. B*, vol. 470, no. 1-2, pp. 198–201, 2001. 92
- [211] Y. Wen, K. He, Y. Zhu, F. Han, Y. Xu, I. Matsuda, Y. Ishii, J. Cumings, and C. Wang, “Expanded graphite as superior anode for sodium-ion batteries,” *Nat. Commun.*, vol. 5, no. 1, p. 4033, 2014. 92
- [212] Y.-C. Lin, A. Motoyama, S. Kretschmer, S. Ghaderzadeh, M. Ghorbani-Asl, Y. Araki, A. V. Krasheninnikov, H. Ago, and K. Suenaga, “Polymorphic phases of metal chlorides in the confined 2D space of bilayer graphene,” *Adv. Mater.*, vol. 33, no. 52, p. 2105898, 2021. 92

- [213] M. Will, T. Hartl, V. Boix de la Cruz, P. Lacovig, S. Lizzit, J. Knudsen, T. Michely, and P. Bampoulis, “Growth, stability, and electronic decoupling of Pt clusters on h-BN/Ir (111),” *The Journal of Physical Chemistry C*, vol. 125, no. 7, pp. 3880–3889, 2021.

Danksagung

Zu aller erst möchte ich Prof. Dr. Thomas Michely danken, dass er es mir ermöglicht hat diese Arbeit in seiner Arbeitsgruppe durchzuführen. Ohne seine Anleitung, Ideen und positiven Bestärkungen seit meiner Bachelorarbeit, bis hin zu dieser Thesis wäre diese nicht möglich gewesen. Ich bin sehr froh ihn meinen "Doktor-Vater" nennen zu dürfen.

Mein Dank gilt weiterhin Prof. Dr. Ruslan Temirov der kurzerhand die Rolle als zweiter Gutachter dieser Arbeit übernommen hat.

Prof. Dr. Klas Lindfors möchte ich für die Übernahme des Vorsitzes der Prüfungskommission danken.

Besonderer Dank gilt außerdem der gesamten aktuellen und ehemaligen AG-Michely, die die Durchführung dieser Arbeit nicht nur ermöglicht, sondern zu einer Freude gemacht haben. Namentlich erwähnen möchte ich hierbei zuerst Camiel Van Efferen, Catherine Grover, Wouter Jolie und Jeison Fischer die einzelne Kapitel meiner Thesis Korrektur gelesen haben. Moritz Will möchte ich dafür danken, dass er mich in der Masterarbeit und den ersten Schritten dieser Thesis tatkräftig unterstützt hat und es mir so ermöglicht hat seine Arbeit erfolgreich fortzuführen. Pantelis Bampoulis hat ebenso große Teile dieser Arbeit mitgetragen und seine Anleitung bei Experimenten war unerlässlich für das Gelingen dieser.

Hervorheben möchte ich auch die unendlichen Mühen von Pascal Hurth, der nicht nur meine Ideen durch Magie und 3D Druck zur Realität werden lies, sondern auch unermüdlich geholfen hat alle technischen Probleme (von denen es nicht zu wenige gab) auszumerzen. Weiterhin möchte ich Camiel Van Efferen und Stefan Schulte danken, das ich sie nicht nur als Kollegen sondern auch als Freunde kennenlernen durfte. Die Zeit im Büro, im Labor, auf Konferenzen und Messreisen mit euch war mir immer eine Freude!

A special thanks is in order for Jan Knudsen, Virginia Boix de la Cruz, Alexei Preobrajenski, Rajendra Singh, Arixin Bo, Jani Kotakoski and Marko Kralj, all of whom have enabled this work and supported me throughout measurements in their labs or at beamtimes and taught me

how to see below the surface!

Zu einer guten Arbeitsatmosphäre haben auch die anderen Mitglieder des Experimentuts beigetragen. Namentlich erwähnen möchte ich Robin Bernhard und Lukas Rieland, aka das Meme-Team. Ausserdem Lara Pätzold, die mir immer ein offenes Ohr geliehen hat auch wenn wir uns nicht immer ganz einig waren.

Meinem Kommilitonen, Doktoranden-Kollegen und langjährigen Freund Chris Reinoffer gilt ein besonderer Dank! Ohne dich hätten die letzten Jahre nicht so viel Spass gemacht und die Festivals wären nur halb so schön gewesen. Vielen Dank!

Fabian Hartl gebührt besonderer Dank für die Unterstützung in allen Themen "Chemie" von denen ich nach wie vor viel zu wenig verstehe.

Ein besonderes Dankeschön gilt außerdem meiner Freundin Janina Dreisbach, die mich in den letzten eineinhalb Jahren meiner Thesis begleitet hat. Ich liebe dich!

Zu guter Letzt möchte ich meiner ganzen Familie und insbesondere meinen Eltern und Geschwistern danken die mich immer voll und ganz unterstützt haben!

Erklärung

„Hiermit versichere ich an Eides statt, dass ich die vorliegende Dissertation selbstständig und ohne die Benutzung anderer als der angegebenen Hilfsmittel und Literatur angefertigt habe. Alle Stellen, die wörtlich oder sinngemäß aus veröffentlichten und nicht veröffentlichten Werken dem Wortlaut oder dem Sinn nach entnommen wurden, sind als solche kenntlich gemacht. Ich versichere an Eides statt, dass diese Dissertation noch keiner anderen Fakultät oder Universität zur Prüfung vorgelegen hat; dass sie - abgesehen von unten angegebenen Teilpublikationen und eingebundenen Artikeln und Manuskripten - noch nicht veröffentlicht worden ist sowie, dass ich eine Veröffentlichung der Dissertation vor Abschluss der Promotion nicht ohne Genehmigung des Promotionsausschusses vornehmen werde. Die Bestimmungen dieser Ordnung sind mir bekannt. Darüber hinaus erkläre ich hiermit, dass ich die Ordnung zur Sicherung guter wissenschaftlicher Praxis und zum Umgang mit wissenschaftlichem Fehlverhalten der Universität zu Köln gelesen und sie bei der Durchführung der Dissertation zugrundeliegenden Arbeiten und der schriftlich verfassten Dissertation beachtet habe und verpflichte mich hiermit, die dort genannten Vorgaben bei allen wissenschaftlichen Tätigkeiten zu beachten und umzusetzen. Ich versichere, dass die eingereichte elektronische Fassung der eingereichten Druckfassung vollständig entspricht.“

Teilpublikationen:

- [135] **Tobias Hartl**, Moritz Will, Davor Capeta, Rajendra Singh, Daniel Scheinecker, Virginia Boix de la Cruz, Sophia Dellmann, Paolo Lacovig, Silvano Lizzit, Boris V Senkovskiy, Alexander Grüneis, Marko Kralji, Jan Knudsen, Jani Kotakoski, Thomas Michely and Pantelis Bampoulis
Cluster Superlattice Membranes
ACS Nano **14**, 13629 (2020)
- [208] **Tobias Hartl**, Moritz Will, Pantelis Bampoulis, Daniel Herrmann, Philipp Valerius, Charlotte Herbig, Virginia Boix de la Cruz, Paolo Lacovig, Vedran Vonk, Simon Chung, Andreas Stierle, Silvano Lizzit, Jan Knudsen and Thomas Michely
Carbon Embedding of Pt Cluster Superlattices Templated by Hexagonal Boron Nitride on Ir (111)
J. Phys. Chem. C. **125**, 23435 (2021)

- [133] **Tobias Hartl**, Daniel Herrmann, Moritz Will, Yannic Falke, Alexander Grüneis, Thomas Michely and Pantelis Bampoulis
Silicon cluster arrays on the monolayer of hexagonal boron nitride on Ir (111)
J. Phys. Chem. C. **126**, 6809 (2022)

Köln, den 25.10.2023

Tobias Hartl

Tobias Hartl

Lebenslauf (*Curriculum Vitae*)

Persönliche Daten

Name	Hartl
Vorname	Tobias
Geburtstag	08.05.1993
Geburtsort	Frechen
Staatsangehörigkeit	deutsch

Ausbildung

11/2019 – heute	Promotionsstudium II. Physikalisches Institut, Universität zu Köln Arbeitsgruppe Prof. Dr. T. Michely
10/2016 – 10/2019	M. Sc. Physics, Durchschnittsnote: 1,3 Masterarbeit “Fabrication of a Stable Cluster Membrane” (Note: 1,0) II. Physikalischen Institut, Universität zu Köln
01/2013 – 01/2010	B. Sc in Physik, Universität zu Köln Durchschnittsnote: 1,8 Masterarbeit “Quantitative Charakterisierung von niedrigenergetischen Ionenquellen für kontrollierte Erosionsexperimente ” (Note: 1,0)
06/2012	Allgemeine Hochschulreife, Europagymnasium Kerpen, Durchschnittsnote: 1,4